Photoacoustic Microscopy of Hemodynamics and Oxygen Metabolism at the Microscopic Level

A Dissertation

Submitted to

the Faculty of the School of Engineering and Applied Science

University of Virginia

In Partial Fulfillment

of the Requirements for the Degree

of

Doctor of Philosophy

By

Naidi Sun

June 2020

Approval Sheet

This Dissertation is submitted in partial fulfillment of the requirements

for the degree of

Doctor of Philosophy

Sun, Naidi, Author

This dissertation has been read and approved by the examining Committee:

Hu, Song, Advisor

Peirce-Cottler, Shayn, Committee Chair

Meyer, Craig, Committee Member

Hossack, John, Committee Member

Zuo, Zhiyi, Committee Member

Accepted for the School of Engineering and Applied Science:

Benson, Craig H., Dean

School of Engineering and Applied Science

June 2020

In memory of my father Yue,

Dedicated to my mother Lihua,

Dedicated to my beloved wife Ningning,

for their unfaltering support and unconditional love

Acknowledgements

I would like to express my deepest gratitude to my advisor, Dr. Song Hu, for his constant mentorship from the first day when I came to his lab as a volunteer, then throughout my PhD journey. Without his continuous guidance and encouragement, this dissertation would not be possible. His enthusiasm and meticulous for scientific research truly inspired me and will continue to guide me in my future career. I feel extremely fortunate to have Dr. Hu not only as my advisor on research, but also as my mentor in life.

I would also like to express my sincere appreciation to my committee members, Dr. Shayn Peirce-Cottler, Dr. Craig Meyer, Dr. John Hossack, and Dr. Zhiyi Zuo, for their invaluable advice and insightful suggestion on my research and dissertation work.

I am also grateful to my collaborators, Dr. Shayn Peirce-Cottler, Dr. Zhiyi Zuo, Dr. John Hossack, Dr. David Kashatus, Dr. Chia-Yi Kuan, Dr. Mark D. Okusa, Dr. Christopher A. DeRosa, Dr. Leif G. Carlsson, Dr. Regina Fritsche-Danielson, Dr. Kenny M. Hansson, Dr. Patrick S. Cottler, Dr. Diane L. Rosin, Dr. Jennifer Kashatus, Anthony C. Bruce, Dr. Yu-Yo Sun, Dr. Shuqiu Zheng, Dr. Jun Li, Dr. Hong-Ru Chen, Dr. Ruimin Chen, Dr. Qifa Zhou, Dr. Scott A. Seaman, Sushanth Sathyanarayana, Michaela Rikard, Dr. Aldo Nascimento, Dr. Heather Perry, and Dr. Adam J. Dixon, for their tremendous help and fruitful discussions.

I would like to thank all my lab members past and present for their supports, encouragements, and friendships, including Dr. Matt Kennedy, Dr. Bo Ning, Dr. Rui Cao, Dr. Tianxiong Wang, Dr. Chenchu Zhang, Dr. Zhiqiang Xu, Yiming Wang, Fenghe Zhong, Yifeng Zhou, Tao Sun, Zhuoying Wang, Angela Tran, Vincent Sciortino, Indigo Milne, Rongxin Fu, Jiaqi Chen, and Youwei Bao. It has been a great pleasure to be a part of such a dynamic and friendly group of people. In particular, I would like to thank Dr. Bo Ning and Dr. Rui Cao who have been very helpful with easing my transition to PhD life.

I dedicate my thesis to my family and friends for their support through the days when things were

Abstract

Heart disease, stroke, diabetes, cancer, and kidney disease are leading causes of death in the United States. Across this wide range of complex diseases, the dysfunction in hemodynamics and oxygen metabolism plays an important role. However, the mechanistic details remain incompletely understood. Exquisitely sensitive to blood hemoglobin—the primary oxygen carrier in the circulation, multi-parametric PAM holds great potential to bridge the knowledge gap. My thesis research focuses on the development of advanced multi-parametric PAM instruments and complementary analytical tools, which together have enabled comprehensive quantification of hemodynamics and oxygen metabolism at the microscopic level *in vivo*. I have demonstrated the utility of this first-of-a-kind hardware-software platform in multiple tissue/organ sites (e.g., the skin, brain, kidney and muscle) and have applied it to study hemodynamic and oxygen-metabolic dysfunction in multiple mouse disease models, including ligation-based hemodynamic redistribution and arteriogenesis, acute kidney injury, ischemic stroke, neonatal brain injury, wound healing, and cancer.

In Chapter 2, we developed a set of novel algorithms for C_{Hb} quantification, tissue-level MRO_2 /$CMRO_2$ quantification, vessel segmentation, the ultrasound-aided and real-time contour imaging methods. In Chapter 3, we revealed a new, inverse relationship between initial vascular resistance and extent of arteriogenesis, as well as the moderate diameter increase and flow upregulation in collateral arterioles for obese mice which were subsequently lost compared to the lean mice, after the ligation of feeding arteries. In Chapter 4, we showed that intradermal injection of AZD8601 formulated in a biocompatible vehicle results in pronounced, sustained and dose-dependent vasodilation, blood flow

upregulation, and neovessel formation, in striking contrast to those induced by recombinant human VEGF-A protein, a non-translatable variant of AZD8601, and citrate/saline vehicle. And we also showed that sequential dosing of AZD8601 could accelerated re-epithelialization during the early phase of diabetic wound healing. In Chapter 5, we revealed a strong correlation between inhaled oxygen concentration and measured sO_2 of mouse kidney, and the change of oxygen stress was associated with reduced kidney ATP levels in the early stages of LPS-induced AKI. In Chapter 6, a first-of-a-kind long-lifetime (>5 months), cortex-wide (6×8 mm^2), and light-weight (<2 g) cranial window approach was explored, and utilized in awake versus. anesthesia comparison and longitudinally monitoring the cerebrovascular responses to photothrombotic stroke throughout the recovery process. In Chapter 7, we utilized the multi-parametric PAM in neonatal mice using the Vannucci HI model and the results showed a rapid drop of $CMRO_2$ during the HI with rapid recovery in the latent phase, and finally irreversible dropped again as the second energy failure. The effectiveness of therapeutic hypothermia was also confirmed by the hypothermia reduced post-HI mitochondrial hyperactivity and moderate decrease of $CMRO_2$.

Table of content

Abbreviations

2-D:	Two-dimensional
3-D:	Three-dimensional
AKI:	Acute kidney injury
BBB:	Blood-brain barrier
BPF:	Bandpass filter
BS:	Beam sampler
CAD:	Coronary artery disease
CBF:	Cerebral blood flow
C_{Hb}:	Total hemoglobin concentration
CL:	Correction lens
Cmax:	Maximum concentration
$CMRO_2$:	Cerebral metabolic rate of oxygen
$CMRO_{2i}$:	Index for cerebral oxygen metabolism
Ct:	Cycle threshold
DBS:	Dichroic beam splitter
DCS:	Diffuse correlation spectroscopy
DL:	Doublets
FC:	Fiber collimator
FCA:	Flow cross-sectional area

FDNIRS: Dual frequency-domain near-infrared spectroscopy

GPU: Graphics processing unit

H&E: Hematoxylin-eosin

HI: Hypoxic-ischemic

HIE: Hypoxic-ischemic encephalopathy

KIM-1:   Kidney injury molecule-1

LPS: Lipopolysaccharide

LSCI: Laser speckle contrast imaging

MEMS: Micro electromechanical system

micro-CT: Microcomputed tomography

MMP-9:   Matrix metalloproteinase-9

MPR: Myocardial perfusion reserve

MRI: Magnetic resonance imaging

MRO_2:   Metabolic rate of oxygen

MRS: Magnetic resonance spectroscopy

NAG: N-acetyl-β-D-glucosaminidase

NDF: Neutral-density filter

NT: Non-translatable

OCR: Oxygen consumption rate

OEF: Oxygen extraction fraction

PAM: Photoacoustic microscopy

PAS: Periodic acid-Schiff

PBS: Polarizing beamsplitter

PC: Peritubular capillary

PD: Photodiode

PET: Positron emission tomography

PM-SMF: Polarization-maintenance signal-mode fiber

RBC: Red blood cells

ROI: Region of interest

RT-qPCR: Reverse transcription PCR

SA-AKI: Sepsis associated acute kidney injury

SAM: Scanning acoustic microscopy

SD: Standard deviation

SEM: Standard error of the mean

SMF: Single-mode fiber

SNR: Signal-to-noise ratio

sO_2:   Saturation of oxygen

TPM: Two-photon microscopy

TTC: Triphenyltetrazolium chloride

UT: Ultrasonic transducer

VAD: Vessel area density

VEGF-A: Vascular endothelial growth factor A

List of Figures

indicates the ligated arteriolar tree, and the ligation site lies outside PAM images. The insets in (a, c) are the blowups of the white boxed regions at the lower left corners of the two panels.

Fig. 3.4. Single-vessel analysis of collateral remodeling in (a) diameter and (b) volumetric blood flow over the yellow boxed region in Fig. 3.3c. Data are shown in absolute value (a: μm, b: nL/s), as well as the relative changes (%) between two adjacent time points in brackets. Increased and decreased values are labeled in green and red, respectively. Purple is used to label vessel segments that are missing in one of the two time points. In (b), solid and dashed lines indicate segments without and with reversed flow direction, respectively. Arrows indicate the flow direction.

Fig. 3.5. Reproducibility of Multi-parametric PAM in unperturbed microvascular network in the mouse ear without ligation surgery.

Fig. 3.6. Single-vessel analysis of the mouse ear without ligation surgery in (a) vessel diameter, (b) blood flow speed, (c) sO_2, (d) blood oxygen supply, (e) wall shear stress, and (f) vascular resistance, respectively.

Fig. 3.7. Multi-parametric analysis of the competition in collateral remodeling. (a) Longitudinal monitoring of the ear microvascular network before, right after, and up to 21 days following the arterial ligation (scale bar: 1mm). The three collateral arterioles are labeled in red, green and blue, respectively. Red cross indicates the ligated arteriolar tree. (b–g) Multifaceted collateral remodeling quantified as relative changes (%) in vessel diameter, blood flow speed, sO_2, blood oxygen supply, wall shear stress, and vascular resistance, respectively.

Fig. 3.8. Relationship between initial vascular resistance and the extent of collateral remodeling. (a-d) Inverse correlation between initial resistance and changes in vessel diameter, volumetric blood flow, tortuosity and wall shear stress, respectively. The analyses are based on 11 collateral arterioles from 6 mice.

Fig. 3.9. Relationship between initial vascular resistance and the extent of collateral remodeling. (a–d) Inverse correlation between initial resistance and changes in vessel diameter, volumetric blood flow,

tortuosity and wall shear stress, respectively. The analyses are based on 19 collateral arterioles from 10 mice of 3 different strains.

Fig. 3.10. Influence of obesity on the ligation-induced hemodynamic redistribution. (a, b) Multi-parametric PAM images. The red crosses in (a) and (b) indicate the ligated arteriolar trees, and the ligation site lies outside PAM images. (c, d) Blowups over the white boxed region in (a) and (b). White arrows: remodeling collateral vessels. (e) Tissue-level hemodynamic responses to the ligation extracted by taking the differences between the measurements acquired at each of the post-ligation points and that acquired before ligation. Black dash area: the hypoxia region (scale bar: 500μm).

Fig. 3.11. Influence of obesity on the ligation-induced remodeling in microvascular structure and function. Colored asterisks indicate the statistical significance over the pre-ligation values, while black asterisks indicate that between the two animal groups at the same time point. Data were presented as mean±SD. (*: $p<0.05$, **: $p<0.01$, and ***: $p<0.001$).

Fig. 3.12. Influence of obesity on the relationship between initial vascular resistance and the extent of collateral remodeling. Inverse correlation between initial resistance and changes in (a) vessel diameter, (b) volumetric blood flow and (c) tortuosity, respectively, in the control and obese mice. Statistical significance between the linear fittings of the two groups is indicated below each panel. (ns: not significant, **: $p<0.01$).

Fig. 4.1. Transfection efficiency, pharmacokinetic characterization, and hybridization of AZD8601. (a) subsequent measurement of human VEGF-A protein. Levels of VEGF-A protein produced are normalized to levels produced by AZD8601 (n = 3/group). (b) Maximum concentration of VEGF-A protein (Cmax) after intradermal injection in db/db mice of 10, 100 and 300 μg of AZD8601 in citrate/saline (n = 6/dose group, left panel). Human VEGF-A protein content in skin biopsies up to 144 hours after intradermal injection of 100 μg citrate/saline-formulated AZD8601 in db/db mice (n = 3–8/time point, right panel). (c) In situ hybridization staining for AZD8601 (brown color in the upper panel) and immunohistochemistry staining for human VEGF-A protein (magenta color and black arrows in the lower panel) after intradermal injection of 100 μg AZD8601 in citrate/saline formulation as a function of

time up to 144 hours. Magnification is 400x.

Fig. 4.2. (a) Time-lapse multi-parametric PAM of microvascular responses to 100 μg of AZD8601 or NT-VEGF-A mRNA intradermally injected to the mouse ear. (b) Statistical comparison of the multifaceted microvascular responses to AZD8601, VEGF-A protein, NT-VEGF-A mRNA, and citrate/saline vehicle (n = 8/group). $*p < 0.05$, $**p < 0.01$, $***p < 0.001$, and $****p < 0.0001$.

Fig. 4.3. Time-lapse multi-parametric PAM of microvascular responses to (a) recombinant human VEGF-A protein or (b) citrate/saline vehicle intradermally injected to the mouse ear.

Fig. 4.4. Intradermal injection of 100 μg AZD8601 induces angiogenesis and neovascularization. Top row, microvascular structure of the whole field of view. Bottom row, zoom-in of the blue boxed region showing detailed view of the capillary angiogenesis on day 7 and neovessel formation on day 14 (green arrows).

Fig. 4.5. Time-lapse multi-parametric PAM of microvascular responses to sequential dosing of (A) 100 μg AZD8601 or (B) saline vehicle intradermally injected to the mouse ear on day 0, 2 and 4.

Fig. 4.6. Statistical comparison of the multifaceted microvascular responses in diameter, volumetric flow, oxygen extraction fraction (OEF), and oxygen metabolism to single and multiple injections of AZD8601 and citrate/saline vehicle (n = 4/group). $*p < 0.05$, $**p < 0.01$, $***p < 0.001$, and $****p < 0.0001$.

Fig. 4.7. Time-lapse multi-parametric PAM of microvascular responses to 30 μg of AZD8601 intradermally injected to the mouse ear.

Fig. 4.8. Time-lapse multi-parametric PAM of microvascular responses to 10 μg of AZD8601 intradermally injected to the mouse ear.

Fig. 4.9. Repeated and higher doses of AZD8601 had greater effects on diabetic wound healing. (a) Dosing on days 0 and 3 increased early healing compared to dosing on day 0 only (n = 7–8/group). (b) The greatest effect on wound closure was achieved by the 200 μg dose of AZD8601 (n = 6/group). $*p < 0.05$, $**p < 0.01$, $***p < 0.001$.

Schematic of the coronal cross section of the cranial window. (d) Dimensions and weight of the custom-made 3-D printed head frame.

Fig. 6.2. PAM imaging with and without the in-tact skull and restoration of BBB over time. (a) Structural PAM images of the cortical vasculature through the in-tact skull before (left), and after (right) the cranial window installation, once the skull has been removed. Scale bar: 1mm, blowup: 250μm. (b) Structural PAM image of the cortical vasculature on day 4 after the cranial window installation. Dashed circle: major hemorrhages in the brain. Scale bar: 1mm. (c) Visualization of Evans blue leakage 2 hours after dye injection (bottom) compared to baseline image before injection (top) at different timepoints after cranial window installation Scale bar: 1mm. (d) Evans blue coverage after date of initial cranial window installation.

Fig. 6.3. (a) Longitudinal imaging of the awake mouse brain through a cranial window by multi-parametric PAM (Row 1–3) and a dissecting microscope (Row 4). Scale bar: 1 mm. (b-e) Segmentation-based quantitative analysis shows unchanged vascular structure and function over the prolonged monitoring period.

Fig. 6.4. Qualitative and quantitative comparisons between mouse cortex imaged at awake and anesthetized conditions. (a) PAM images of awake (left) and anesthetized (right) mouse cortical vasculature. Scale bar: 1 mm.   (b-e) Statistical comparisons of key functional parameters in arteries and veins between awake and anesthetized mice ($N = 5$).

Fig. 6.5. (a) Longitudinal PAM of cerebrovascular responses to photothrombotic stroke. Dashed circle: focal ischemic region. Scale bar: 1 mm. (b-e) Quantitative analysis of structural and functional vascular remodeling and associated metabolic changes in response to stroke injury and recovery. (f) Co-registered PAM and TTC images show a correlation between reduced $CMRO_2$ and tissue infarction.

Fig. 7.1. Neonatal mouse brain imaging platform.

Fig. 7.2. (a) sO_2 and flow speed under 20.9%-vs-10% O_2. (b) PAM-derived CBF, OEF, and $CMRO_2$.

Fig. 7.3. Combined HI causes $CMRO_2$-suppression and a rapid recovery in the ipsilateral hemisphere in P10 mice. (a) Sequential sO_2 and flow speed images of the indicated phases. (b) Quantification of CBF, OEF, and $CMRO_2$ (n=4). *: $p<0.05$ and ** $p<0.01$ for the indicated comparison by t-test. (c) Tracing of the different $CMRO_2$ responses to HI in ipsilateral-versus-contralateral hemispheres.

Fig. 7.4. Comparison of the mitochondria activity and integrity at 2-versus-5 h post-HI. p-value is determined by t-test. n=3-4 as indicated.

Fig. 7.5. (a) Correlation of TTC-defined infarction and severe $CMRO_2$ reduction in awake mice at 24 h post-HI. The $CMRO_2$ values in the normothermia-vs-hypothermia treated mouse hemispheres were labeled. (B) Statistical analysis (n=3 for each).

Fig. 7.6. Hypothermia protects against the rapid demise of mitochondria after experimental HIE in mice. p-value is determined by t-test.

Fig. 8.1. (a) Pictures of wound healing process taken by microscopy; (b) Time-lapse PAM of the hemodynamic change during wound healing, For the height map, "0" is the position of the very bottom point for the ear microvasculature. The black-white images are the cross-section B-scans indicated in height images with the white dashed line, to show the thickness change in the wound area. Arrows on sO_2 map indicate the feeding arteries and draining veins analyzed in Fig. 8.2. Horizontal scale bar: 500 μm, vertical scale bar: 50 μm.

Fig. 8.2. Statistical comparison (N = 4) of (a-c) Structural change, (d-g) Hemodynamic change based on vessel segmentation, and (h-i) Hemodynamic change at the tissue level in the wound healing process. Healing front is defined as the surrounding of the wound with 10% area of the open wound area. White asterisks within the bars indicate the p value between the baseline (data not shown) and the certain timepoint. Paired t-test was used in (a), (b), (h) and (i), while two-way ANOVA tests were used in (c-g). *, **, ***, and **** respectively represent $p<0.05$, $p<0.01$, $p<0.001$, and $p<0.0001$. Data are presented as mean $\pm$ SD.

Chapter 1 Introduction

1.1 Background and motivation

Hemodynamic and oxygen-metabolic dysfunction almost occur in all kinds of diseases and/or tissue abnormalities: the lack of proper vascularization is a major complication that underlies a wide variety of devastating diseases, including coronary artery disease[1], heart failure[2], critical limb ischemia[3], and chronic diabetic ulcers with impaired wound healing ability[4]; abnormal oxygen metabolism also has a profound effect on ischemic brain stroke[5], tumor growth[6], Alzheimer's disease[7] and other metabolism-related pathophysiological diseases[8-10]. Therefore, a tremendous effort has been made to comprehensively study the dysfunction in hemodynamic and oxygen-metabolism in clinical research and diagnosis[11-20].

In the past decades, the dramatic growth in biomedical applications of imaging technologies brings a fresh perspective for this biological study, including but not limited to, positron emission tomography (PET)[11,12], functional ultrasound[21,22], laser speckle contrast imaging (LSCI)[23], two-photon microscopy (TPM)[20,24], magnetic resonance imaging/spectroscopy (MRI/MRS)[25,26], dual frequency-domain near-infrared spectroscopy and diffuse correlation spectroscopy (FDNIRS/DCS)[27]. However, all these technologies have fundamental limitations, remaining the mechanistic details of hemodynamic and oxygen-metabolic dysfunction incompletely understood.

Capitalizing on the light absorption of hemoglobin, photoacoustic microscopy (PAM) holds great potential to label-free and noninvasive characterization of the microvasculature[28-31]. This novel technique inspired a new approach to the comprehensive quantification of hemodynamics and oxygen metabolism

both at the single-microvessel level and microscopic level *in vivo*, with the advanced multi-parametric PAM instruments and complementary analytical tools. By the utility of this first-of-a-kind hardware-software platform in multiple tissue/organ sites (e.g., the skin, brain, kidney and muscle), multiple mouse disease models, including diabetic wound healing, ischemic stroke, neonatal brain injury, cancer, and acute kidney injury, could be studied both anatomically and functionally.

1.2 Overview of the dissertation

In Chapter 2, development of the current multi-parametric PAM instruments and complementary analytical tools was made, enabling comprehensive quantification of hemodynamics and oxygen metabolism at the microscopic level *in vivo*, then both of the *in vivo* and *in vitro* test was made to demonstrate these technical renovations. Specifically, the method for quantification of total hemoglobin concentration (C_{Hb}) with the statistical analysis of the PAM signal based the Brownian motion of hemoglobin-carrying red blood cells (RBCs) was developed first, then a MATLAB-based vessel segmentation algorithm was also developed, enabling to extract hemodynamic parameters within individual microvessels. Based on the simultaneously measurement of C_{Hb}, saturation of oxygen (sO_2), and blood flow speed—all the hemodynamic parameters required for quantification of metabolic rate of oxygen (MRO_2) or cerebral MRO_2 ($CMRO_2$), the measurement was extended to the microscopic-level MRO_2 map using Fick's law by superposing the measurements of individual of segments. At last, two contour scan algorithms were developed for the contour cortex-wide brain imaging, and validated in both of the phantom and *in vivo* experiments.

In Chapter 3, we used the developed hardware-software integrated platform for quantitative,

longitudinal, and label-free imaging of network-wide hemodynamic changes and arteriogenesis at the single-vessel level. By ligating feeding arteries in the mouse ear, we induced network-wide hemodynamic redistribution and localized arteriogenesis. The utility of this technology was demonstrated by studying the influence of obesity on microvascular arteriogenesis. Simultaneously monitoring the remodeling of competing collateral arterioles revealed a new, inverse relationship between initial vascular resistance and extent of arteriogenesis. Obese mice exhibited similar remodeling responses to lean mice through the first week, including diameter increase and flow upregulation in collateral arterioles. However, these gains were subsequently lost in obese mice. Capable of label-free, comprehensive, and dynamic quantification of structural and functional changes in the microvascular network *in vivo*, this platform opens up new opportunities to study the mechanisms of microvascular arteriogenesis, its implications in diseases, and approaches to pharmacologically rectify microvascular dysfunction.

In Chapter 4, we longitudinally and comprehensively characterized microvascular responses to AZD8601, a modified mRNA encoding vascular endothelial growth factor A (VEGF-A), *in vivo*. Using multi-parametric PAM, we showed that intradermal injection of AZD8601 formulated in a biocompatible vehicle results in pronounced, sustained and dose-dependent vasodilation, blood flow upregulation, and neovessel formation, in striking contrast to those induced by recombinant human VEGF-A protein, a non-translatable variant of AZD8601, and citrate/saline vehicle. Moreover, we evaluated the bioactivity of AZD8601 in a mouse model of diabetic wound healing *in vivo*. Using a boron nanoparticle-based tissue oxygen sensor, we showed that sequential dosing of AZD8601 improves vascularization and tissue

oxygenation of the wound bed, leading to accelerated re-epithelialization during the early phase of diabetic wound healing.

In Chapter 5, we have developed a novel, label-free technique using intravital multi-parametric PAM to directly monitor the hemodynamic changes of sO_2 and blood flow of the kidney microvasculature. *In vivo* PAM performed in mice challenged with 14% oxygen revealed a strong correlation between inhaled oxygen concentration and measured sO_2. With a lipopolysaccharide (LPS) induced acute kidney injury (AKI) model, time dependent changes in hemodynamic parameters and kidney injury markers were observed. The change of oxygen stress was associated with reduced kidney ATP levels in the early stages of LPS-induced AKI. This technical innovation lays the foundation for dynamic monitoring of renal oxygen metabolism in AKI, as well as chronic kidney disease.

In Chapter 6, we have developed the first-of-a-kind long-lifetime (>5 months), cortex-wide (6×8 mm2), and light-weight (<2 g) cranial window with dual transparency to both light and ultrasound. The lifetime of the new cranial window was demonstrated by multi-parametric PAM of the awake mouse brain over an extended period of 24 weeks, during which no dura thickening, skull regrowth, or window-induced changes in the functional readouts was observed. Moreover, the effect of the window implantation on the blood-brain barrier (BBB) was examined with an *in vivo* Evan Blue assay, which showed a complete recovery of the BBB integrity within 14 days. The utility of the present technique for studying the chronic progression of brain diseases was demonstrated by monitoring the functional recovery of the mouse brain from ischemic stroke throughout the acute (<24 hours), subacute (1−5 days), and chronic (up to 4 weeks) stages of ischemic stroke. The large window size allows simultaneous

recording of the ipsilateral (i.e., ischemic) and the contralateral hemispheres for side-by-side comparison. This work opens up numerous new opportunities to study the chronic progression of a wide spectrum of neurovascular disorders and their responses to therapies.

In Chapter 7, we first extended our previously developed head-restrained PAM from adult mice to P10 (i.e., ten days after birth) mice, enabling awake and cortex-wide contour imaging, and validated it with global hypoxia experiment. The results showed that hypoxia increases $CMRO_2$, which is consistent with the MRI-based results of the metabolic response to 10-14% oxygen by adult human subjects. Then, the Vannucci hypoxic-ischemic (HI) model was used to mimic the hypoxic-ischemic encephalopathy (HIE) condition in neonatal mice, and the hemodynamic parameters were acquired by PAM to calculate $CMRO_2$ for the comparison of the contralateral and ipsilateral side. Both of the PAM and biochemistry results showed a rapid drop of $CMRO_2$ during the HI with rapid recovery in the latent phase, and finally irreversible dropped again as the second energy failure. At last, we explored the effectiveness of therapeutic hypothermia, and the results showed that hypothermia reduced post-HI mitochondrial hyperactivity and moderate decrease of $CMRO_2$.

Reference

[1] Nabel, E. G. & Braunwald, E. A Tale of Coronary Artery Disease and Myocardial Infarction. *New England Journal of Medicine* **366**, 54-63 (2012).

[2] Landmesser, U. & Drexler, H. Chronic heart failure: an overview of conventional treatment versus novel approaches. *Nature clinical practice. Cardiovascular medicine* **2**, 628-638 (2005).

[3] Varu, V. N., Hogg, M. E. & Kibbe, M. R. Critical limb ischemia. *Journal of vascular surgery* **51**, 230-241 (2010).

[4] Brem, H. & Tomic-Canic, M. Cellular and molecular basis of wound healing in diabetes. *J Clin Invest* **117**, 1219-1222 (2007).

[5] Girouard, H. & Iadecola, C. Neurovascular coupling in the normal brain and in hypertension, stroke, and Alzheimer disease. *Journal of applied physiology (Bethesda, Md. : 1985)* **100**, 328-335 (2006).

[6] Kallinowski, F. *et al.* Blood flow, metabolism, cellular microenvironment, and growth rate of human tumor xenografts. *Cancer research* **49**, 3759-3764 (1989).

[7] Iadecola, C. Neurovascular regulation in the normal brain and in Alzheimer's disease. *Nature reviews. Neuroscience* **5**, 347-360 (2004).

[8] Tadros, T., Traber, D. L. & Herndon, D. N. Hepatic blood flow and oxygen consumption after burn and sepsis. *The Journal of trauma* **49**, 101-108 (2000).

[9] Cheng, K. *et al.* Hypoxia-inducible factor-1alpha regulates beta cell function in mouse and human islets. *The Journal of clinical investigation* **120**, 2171-2183 (2010).

[10] Maquet, P. Sleep function(s) and cerebral metabolism. *Behavioural Brain Research* **69**, 75-83 (1995).

[11] Frackowiak, R. S., Lenzi, G. L., Jones, T. & Heather, J. D. Quantitative measurement of regional cerebral blood flow and oxygen metabolism in man using 15O and positron emission tomography: theory, procedure, and normal values. *Journal of computer assisted tomography* **4**, 727-736 (1980).

[12] Ibaraki, M. *et al.* PET measurements of CBF, OEF, and CMRO2 without arterial sampling in hyperacute ischemic stroke: method and error analysis. *Annals of nuclear medicine* **18**, 35-44 (2004).

[13] Xu, F., Ge, Y. & Lu, H. Noninvasive quantification of whole-brain cerebral metabolic rate of oxygen (CMRO2) by MRI. *Magnetic resonance in medicine* **62**, 141-148 (2009).

[14] Zhou, C. *et al.* Diffuse optical monitoring of blood flow and oxygenation in human breast cancer during early stages of neoadjuvant chemotherapy. *Journal of biomedical optics* **12**, 051903 (2007).

[15] Gu, Z. *et al.* NEMA NU-4 performance evaluation of PETbox4, a high sensitivity dedicated PET preclinical tomograph. *Physics in medicine and biology* **58**, 3791-3814 (2013).

[16] Jones, P. B. *et al.* Simultaneous multispectral reflectance imaging and laser speckle flowmetry of cerebral blood flow and oxygen metabolism in focal cerebral ischemia. *Journal of biomedical optics* **13**, 044007 (2008).

[17] Guevara, E., Sadekova, N., Girouard, H. & Lesage, F. Optical imaging of resting-state functional

connectivity in a novel arterial stiffness model. *Biomedical optics express* **4**, 2332-2346 (2013).

[18] Dizeux, A. *et al.* Functional ultrasound imaging of the brain reveals propagation of task-related brain activity in behaving primates. *Nature Communications* **10**, 1400 (2019).

[19] Hall, A. M., Rhodes, G. J., Sandoval, R. M., Corridon, P. R. & Molitoris, B. A. In vivo multiphoton imaging of mitochondrial structure and function during acute kidney injury. *Kidney Int* **83**, 72-83 (2013).

[20] Dunn, K. W. *et al.* Functional studies of the kidney of living animals using multicolor two-photon microscopy. *American Journal of Physiology-Cell Physiology* **283**, C905-C916 (2002).

[21] Macé, E. *et al.* Functional ultrasound imaging of the brain. *Nature Methods* **8**, 662-664 (2011).

[22] Lindner Jonathan, R. *et al.* Ultrasound Assessment of Inflammation and Renal Tissue Injury With Microbubbles Targeted to P-Selectin. *Circulation* **104**, 2107-2112 (2001).

[23] Rege, A., Thakor, N. V., Rhie, K. & Pathak, A. P. In vivo laser speckle imaging reveals microvascular remodeling and hemodynamic changes during wound healing angiogenesis. *Angiogenesis* **15**, 87-98 (2012).

[24] Ashworth, S. L., Sandoval, R. M., Tanner, G. A. & Molitoris, B. A. Two-photon microscopy: Visualization of kidney dynamics. *Kidney International* **72**, 416-421 (2007).

[25] Kobayashi, H. *et al.* Renal tubular damage detected by dynamic micro-MRI with a dendrimer-based magnetic resonance contrast agent. *Kidney International* **61**, 1980-1985 (2002).

[26] Rodgers, Z. B., Detre, J. A. & Wehrli, F. W. MRI-based methods for quantification of the cerebral metabolic rate of oxygen. *Journal of cerebral blood flow and metabolism : official journal of the International Society of Cerebral Blood Flow and Metabolism* **36**, 1165-1185 (2016).

[27] Kang, J. *et al.* Validation of noninvasive photoacoustic measurements of sagittal sinus oxyhemoglobin saturation in hypoxic neonatal piglets. *Journal of applied physiology (Bethesda, Md. : 1985)* **125**, 983-989 (2018).

[28] Wang, L. V. & Hu, S. Photoacoustic Tomography: In Vivo Imaging from Organelles to Organs. *Science* **335**, 1458-1462 (2012).

[29] Cao, R. *et al.* Functional and oxygen-metabolic photoacoustic microscopy of the awake mouse brain. *NeuroImage* **150**, 77-87 (2017).

[30] Ning, B. *et al.* in *Biomedical Optics 2016.* BTh3D.4 (Optical Society of America).

[31] Ning, B. *et al.* Simultaneous photoacoustic microscopy of microvascular anatomy, oxygen saturation, and blood flow. *Opt. Lett.* **40**, 910-913 (2015).

Chapter 2 Development of the advanced multi-parametric PAM instruments and complementary analytical tools

2.1 Introduction

Capable of providing label-free, comprehensive, and quantitative characterization of hemodynamic parameters, PAM has been widely studied on both of the technical side and application side in recent years. A conventional multi-parametric PAM with 300-kHz A-line rate[1], as well as a micro electromechanical system (MEMS)-based PAM have been reported to further improve the speed of PAM imaging[2]. To break the limitation of the axial resolution of conventional PAM, an isotropic-resolution PAM with multi-angle illumination system has been also developed, with the axial resolution 10-fold better than that of conventional PAM[3]. With the rapid development of graphics processing unit (GPU), GPU-based parallel computing has been also utilized in PAM, especially for the blood flow quantification, to accelerate data processing[4]. On the application side, a wide range of different organs and tissues have been studied for multiple disease models, including mouse brain[5], hindlimb[6], and ear[7]. To further explore the possibility of clinical translation, miniaturized PAM have been also developed with smaller size and lighter weight[8]. Although multi-parametric PAM have generated intense scientific interest, there are still some limitations.

The current multi-parametric PAM only enables the mapping of microvascular anatomy, or the distribution of normalized C_{Hb}, but not the absolute value, which will restrict its applications in many disease studies. Besides, without a robust segmentation algorithm, it remains a challenge to comprehensively quantify the hemodynamics in individual microvessels across a complex network *in*

vivo acquired by PAM. In addition, the current metabolic rate of oxygen (MRO$_2$) quantification based on PAM, is the region-related value rather than at the microscopic level which is more related to the practical situation, such as the stroke model. At last, the focal zone of the current two-dimensional (2-D) raster scan of the conventional PAM is often insufficient to accommodate the depth variation of the cortex-wide brain imaging.

In this chapter, the method of C$_{Hb}$ quantification was explored first, then a MATLAB-based vessel segmentation algorithm was developed for extracting the hemodynamic changes at the single-microvessel level. Based on the simultaneously measurement of C$_{Hb}$, sO$_2$, and blood flow speed—all the hemodynamic parameters required for quantification of CMRO$_2$[5,9,10], the measurement was extended to the microscopic level and generate MRO$_2$ maps using Fick's law by superposing the measurements of individual of segments[11]. At last, an integrated scanning acoustic microscopy (SAM) was added to our current multi-parametric PAM system for the contour scanning of cortex-wide brain, and a more advanced real-time contour scan algorithm was also developed.

2.2 Algorithm of absolute C$_{Hb}$ quantification and vessel segmentation

2.2.1 Absolute C$_{Hb}$ quantification

Statistical analysis of the PAM signal can reveal the Possion distribution-governed Brownian motion of hemoglobin-carrying RBCs *in vivo*[12]. Briefly, the average RBC count (N_{RBC}) within the detection volume of PAM can be derived as:

$$E(N_{RBC}) = \frac{E^2(A_{PAM})}{Var(A_{PAM}) - Var(N_{PAM})} \tag{2-1}$$

in which $E()$ and $Var()$ respectively denote the mean and variance operation, A_{PAM} is the amplitude

of the PAM signal, and N_{PAM} is the electronic thermal noise of the PAM system. In the present study,

N_{RBC} is quantified by analyzing 100 successive A-lines acquired at 532 nm. Since each RBC contains

~15 pg of hemoglobin on average[13], the total amount of hemoglobin within the detection volume is

$15 \times N_{RBC}$ pg. Given that the lateral resolution of PAM is 2.7 μm and the $1/e$ penetration of 532-nm light

in rodent blood is 46 μm[14], the detection volume of our system is 263 μm³. Thus, the C_{Hb} (g/L) can be

estimated as:

$$C_{Hb} = 57 \times E(N_{RBC}) \qquad (2\text{-}2)$$

To examine the accuracy of this method *in vitro*, we prepared 10 samples with C_{Hb} evenly distributed

over the range of 15–150 g/L using fresh defibrinated bovine blood (910–100, Quad Five). As shown in

Fig. 2.1, the PAM-measured C_{Hb} values agreed with the preset concentrations (linearity: $R^2 = 0.96$) but

became inaccurate when the C_{Hb} was diluted to below 30 g/L. This inaccuracy is likely due to the

insufficient signal-to-noise ratio of PAM under the severe and non-physiological hemodilution.
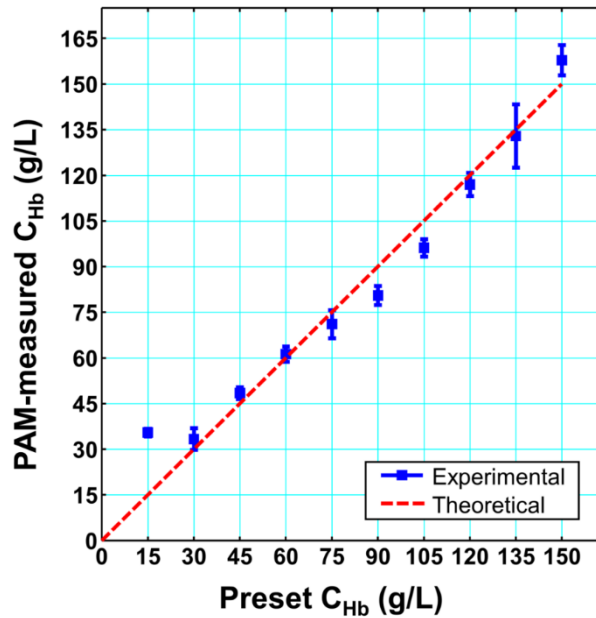
Fig. 2.1. Validation of PAM-based C_{Hb} quantification using defibrinated bovine blood *in vitro*.

By using this method, the absolute C_{Hb} value could be finally quantified, together with the other parameters sO_2 and blood flow, whose methods have been published before[5,10] (Fig. 2.2). These three hemodynamic parameters are the three key parameters required for quantification of MRO_2 or $CMRO_2$, which are essential for study oxygen-metabolic dysfunction and other disease models. A built-in function 'imfilter' in MATLAB was used to generate all the images.
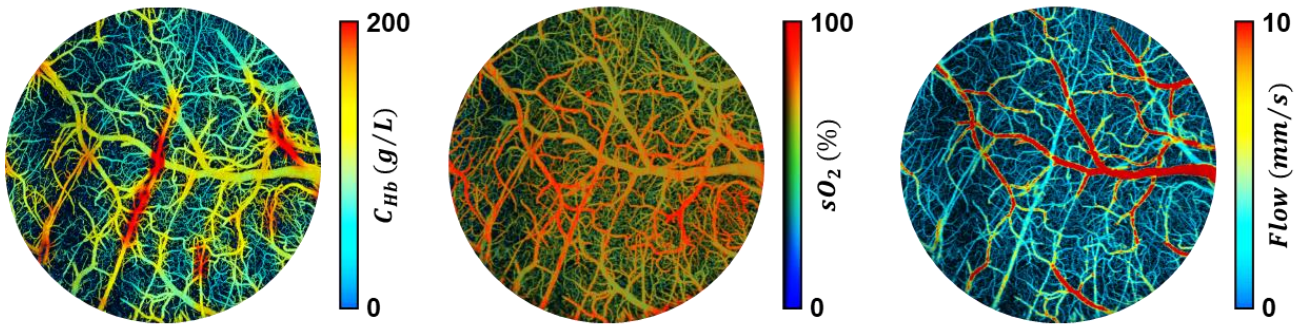
Fig. 2.2. Absolute C_{Hb}, sO_2 and blood flow map acquired by multi-parametric PAM.

2.2.2 Vessel segmentation

To extract ligation-induced changes in diameter, C_{Hb}, sO_2 and blood flow at the single-microvessel level, we have developed a MATLAB-based vessel segmentation algorithm. Briefly, by Hilbert-transforming the raw PAM signals, we generated a map of the microvascular network based on the signal amplitude (Fig. 2.3a). Then, the boundaries of one certain interested vessel will be manually identified found within the zoom-in area (Fig. 2.3b), and Otsu's algorithm was applied to obtain an appropriate intensity threshold between the vasculature and the non-vessel background (Fig. 2.3c). Using this threshold, background pixels were removed and vascular boundaries were obtained. To ensure the boundary smoothness, isolated and spur parts of the boundaries were removed. Thus, all the three

hemodynamic parameters C_{Hb}, sO_2 and blood flow of this interested vessel could be obtained (Fig. 2.3d).

Furthermore, individual vessel axis was extracted by applying a morphological function in the MATLAB

(i.e., skel) to track the vascular skeleton, from which the vessel length was obtained. By quantifying the

total number of pixels occupied by the vessel (i.e., vessel area), the average diameter of the vessel could

be estimated as the ratio of the vessel area to the length[15]. The segmentation analysis also enabled

quantification of other vascular parameters including:

$$tortuosity = \frac{L}{C} \tag{2-3}$$

$$volumetric\ flow = \frac{\pi}{8}vd^2 \tag{2-4}$$

$$oxygen\ supply = volumetric\ flow \cdot sO_2 \tag{2-5}$$

$$resistance = \frac{8\eta L}{\pi r^4} \tag{2-6}$$

$$wall\ shear\ stress = 4\eta \cdot \frac{volumetric\ flow}{\pi r^3} \tag{2-7}$$

where L is the length of the vessel segment, C is the linear distance between the two endpoints of the

vessel segment, v is the blood flow speed, d is the vessel diameter, r is the vessel radius, and η is

the blood viscosity. The blood viscosity of each vessel segment is estimated based on a previously

published four-step procedure[16-18]:

Step 1: Derive the Newtonian shear rate of each vessel segment as $\frac{8V}{D}$, in which V and D are the

PAM-measured blood flow rate and vessel diameter, respectively.

Step 2: Look up the power-law index n in Dr. Cho's paper[18]. Since the Newtonian shear rate is

measured to be >500 sec^{-1} for all the vessels of interest we imaged, n is set to 0.966.

Step 3: Derive the non-Newtonian shear rate of each vessel segment as $\frac{3n+1}{4n}\frac{8V}{D}$, which is based on

5

Dr. Bird's book[19].

Step 4: Derive the blood viscosity of each vessel segment based on the relationship of the wall shear rate and the viscosity coefficient in Dr. Bate's paper[16].
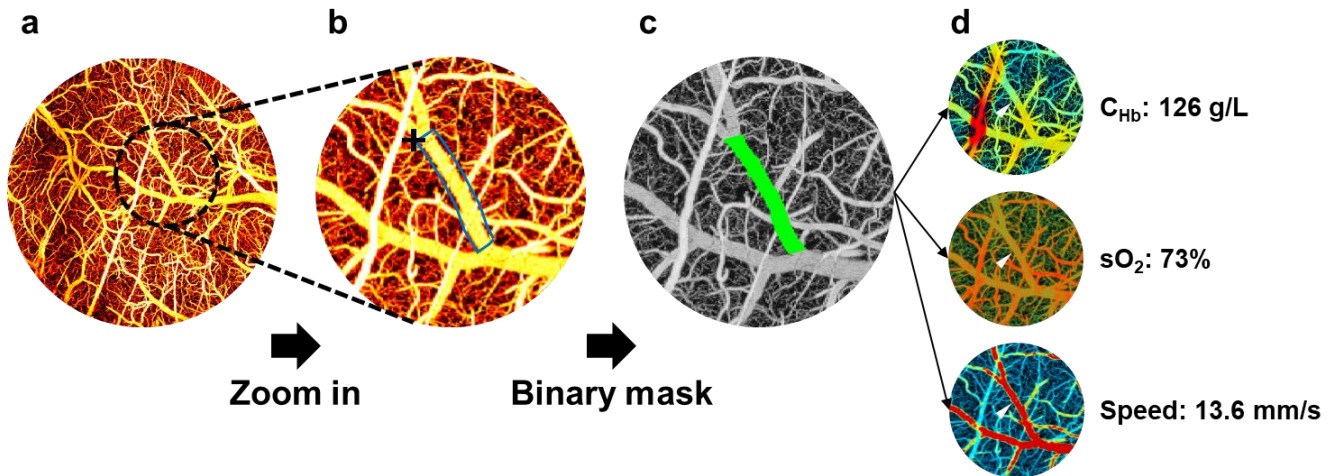
Fig. 2.3. Illustration of vessel segmentation procedures.

2.3 Quantification of MRO$_2$ /CMRO$_2$ at the microscopic level

Although PAM allows *in vivo* characterization of vascular anatomy and hemodynamics by acquisition C$_{Hb}$, sO$_2$, and blood flow—the key parameters for MRO$_2$ calculation[5,9,10], the current demonstrated method[20] of MRO$_2$ quantification is still limited to the region-related MRO$_2$ value rather than at the microscopic level. To meet the gap, a novel algorithm which could extend the measurement to microscopic level and generate MRO$_2$ maps using Fick's law was developed, with the procedures shown in Fig. 2.4.

Specifically, the high resolution of the current multi-parametric PAM (~3 μm) allows quantification of C$_{Hb}$ (Fig. 2.5a), which could be used to generate a diameter distribution map (Fig. 2.5d). By applying

two appropriate thresholds to get rid of large trunk vessels and small capillaries, the small-vessels mask
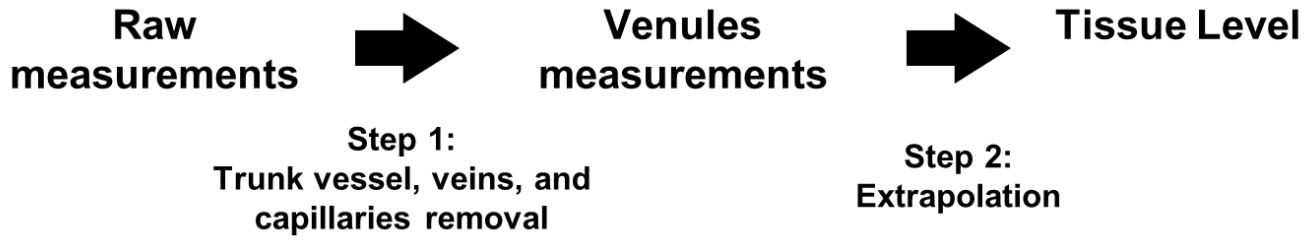
Fig. 2.4. Illustration of MRO$_2$ /CMRO$_2$ quantification at the microscopic level.

map was generated (Fig. 2.5e). Additionally, with the high resolution of sO$_2$ quantification (Fig. 2.5b),

another sO$_2$ threshold for removing arterials was also applied, and then the veins-and-capillaries mask

was also generated (Fig. 2.5c). With the combination of the two masks, the final venules mask was finally
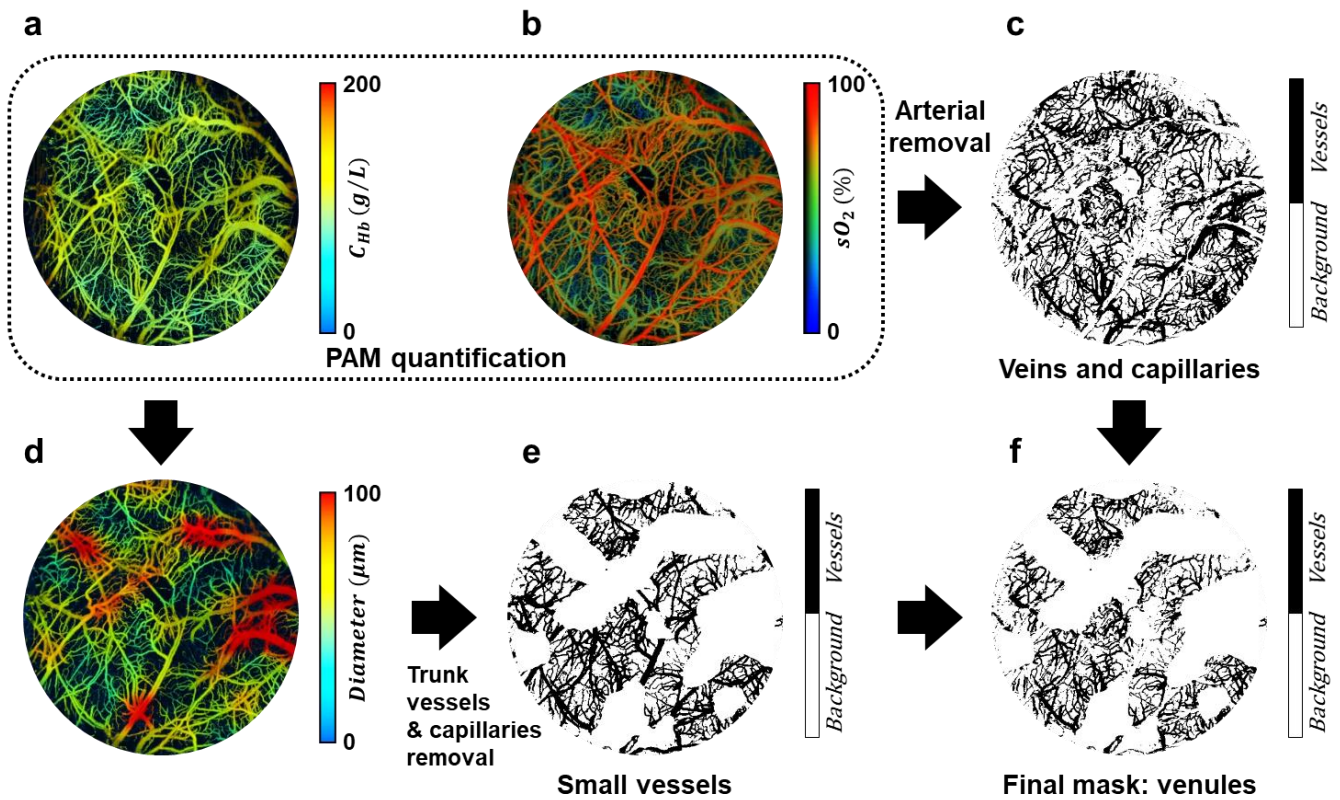
Fig. 2.5. Steps for the generation of venule mask.

7

obtained (Fig. 2.5f), which is essential for the next extrapolation step.

Oxygen extraction fraction (OEF) is defined as the ratio of blood oxygen that a tissue takes from the blood flow to maintain function and morphological integrity, which reflects the efficiency of oxygen utilization by the tissue and, therefore, is one of the hemodynamic parameters in MRO_2 quantification with the definition as:

$$OEF = \frac{s_aO_2 - s_vO_2}{s_aO_2} \qquad (2\text{-}8)$$

where s_aO_2 is the average arterial sO_2 (assumed to be 0.98)[21] and s_vO_2 is venular sO_2. Assuming the blood flow is laminar[22], the PAM-measured flow speed along the vessel axis v (Fig. 2.6c) and lumen diameter d (Fig. 2.6d) could be used to compute the cerebral blood flow (CBF) of an individual vessel segment as:

$$CBF = \frac{(\pi v d^2)}{8} \; (mL/min) \qquad (2\text{-}9)$$

Together with the C_{Hb} (Fig. 2.6a) and sO_2 (Fig. 2.6b) quantifications, by applying the venule mask obtained in step 1, C_{Hb}, OEF and CBF measurement within each segment that contains a single venular cross-section was obtained (Fig. 2.6e, the first column). Then all the measurements to the tissue level were extrapolated by superposing the measurements of individual segments[11], with the weighting factor in superposition defined as an exponential decay with a length constant of 40 μm[23] between the centroid of vessel segment and the location of the tissue of interest[24]. For each iteration, the tissue level quantifications were grown further to the non-venules area (Fig. 2.6e, the second and third column), until the final tissue-level C_{Hb}, OEF, and CBF maps were obtained (Fig. 2.6f). Besides, the tissue-level CBF from mL/min was converted to the standard unit of mL/g/min. Knowing the pixel size of the CBF image

$(2.5\times5~\mu m^2)$ and assuming the average thickness of the mouse cortex to be ~1 mm[25], each image pixel was corresponded to a cortical tissue volume of 12.5×10^{-9} mL. With the brain tissue density (1.05 g/mL)[26], the tissue weighted CBF was converted from mL/min to mL/g/min by the division of the corresponding tissue weight of 12.5×10^{-9} mL $\times$ 1.05 g/mL = 1.3×10^{-8} g.
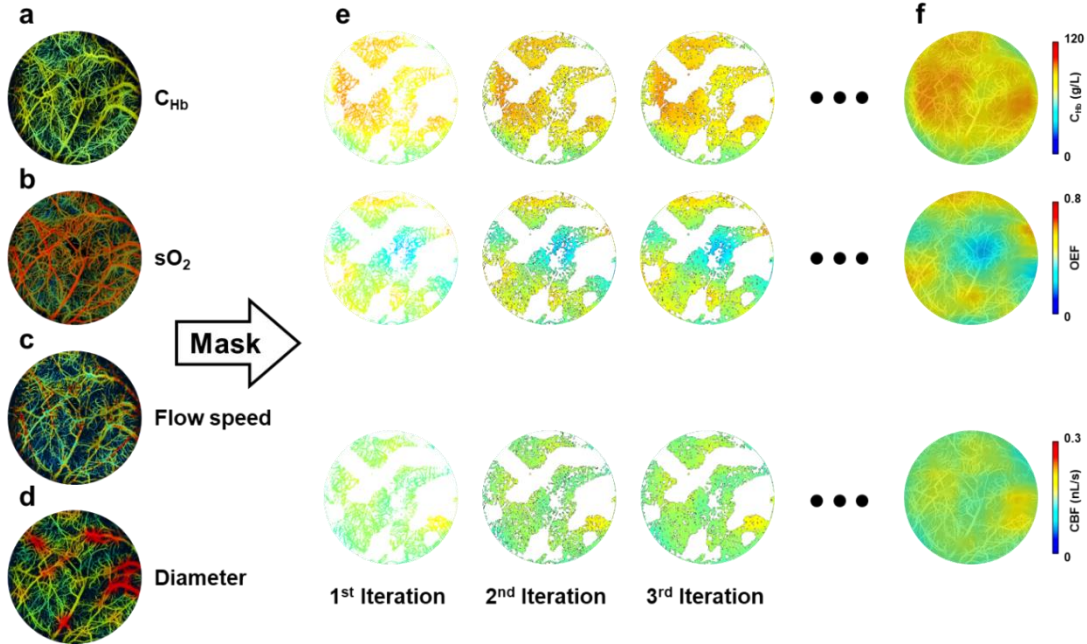
Fig. 2.6. Reproduction of tissue-level C_{Hb}, OEF and CBF maps.

By applying the equation:

$$CMRO_2 = 0.014 \cdot C_{Hb} \cdot s_aO_2 \cdot OEF \cdot CBF \qquad (2\text{-}10)$$

the CMRO$_2$ map was finally derived (Fig. 2.7a). This example was from a photothrombosis-based ischemic stroke model, and the obtained CMRO$_2$ showed a strong spatial correlation with the triphenyltetrazolium chloride (TTC) staining analysis (Fig. 2.7b, black circle: infarct region), which could validate this approach.
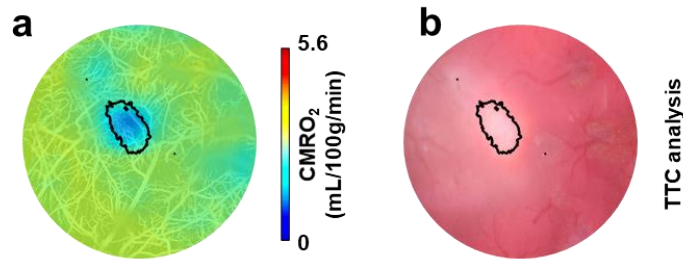
Fig. 2.7. Tissue-level CMRO$_2$ map with the TTC analysis.

2.4 Contour cortex-wide multi-parametric PAM

2.4.1 Ultrasound-aided contour multi-parametric PAM

In this section, an ultrasound-aided multi-parametric PAM platform was developed, which is capable of imaging C$_{Hb}$, sO$_2$, and CBF at the same spatiotemporal scale. With the ultrasonically extracted contour map of the mouse skull, the PAM can dynamically focus on the underlying cortical vasculature when scanning across the uneven brain surface to maintain high spatial resolution and sensitivity. Statistical, spectral, and correlation analysis of the same PAM dataset allows simultaneous quantification of C$_{Hb}$, sO$_2$, and CBF at the microvascular level.

Our ultrasound-aided multi-parametric PAM platform (Fig. 2.8) employs two nanosecond-pulsed lasers (Edgewave, BX40-2-G and BX40-2-GR; wavelengths: 532 and 559 nm; repetition rate: 30 kHz) for dual-wavelength photoacoustic excitation. The two beams with orthogonal polarizations are combined through a broadband polarizing beamsplitter (PBS; Edmund Optics, 48–545), attenuated by a neutral-density filter (NDF; Thorlabs, NDC-50 C-2M), and reduced to the same diameter by an iris (Thorlabs, SM1D12D) for fiber-optic coupling. To enhance the coupling efficiency, the dual-color beam

is focused by a condenser lens (Thorlabs, LA1608) and spatially filtered by a 50-μm-diameter pinhole (Thorlabs, P50C), before being coupled into a single-mode fiber (SMF; Thorlabs, P1-460B-FC-2) through a microscope objective (Newport, M-10X). To compensate for the fluctuation in laser intensity, ~5% of laser energy is tapped off by a beam sampler (BS; Thorlabs, BSF10-A) and monitored by a photodiode (PD; Thorlabs, FDS100). As shown in the blow up of the imaging head (boxed region in Fig. 2.8), the near diffraction-limited fiber output is mapped into the object to be imaged by two identical doublets (Thorlabs, AC127-025-A) through an iris (Thorlabs, SM05D5), a two-axis galvo scanner (Cambridge, 6215HSM40B), a correction lens (Thorlabs, LA1207-A), and a home-made ring-shaped ultrasonic transducer (inner diameter: 2.2 mm; outer diameter: 4.0 mm; focal length: 6.0 mm; center frequency: 35 MHz; 6-dB intensity bandwidth: 70%). The LabVIEW-controlled galvo scanner can steer the laser beam through the central opening of the transducer for automated confocal alignment of the optical-acoustic dual foci. The iris is utilized to reduce the beam diameter to the dimension of the galvo mirrors, and the correction lens is used to compensate for the optical aberration at the interface between the ambient air and ultrasound-coupling liquid (water in our system). For the contour scan, the imaging head is motorized by a three-axis scanner, which consists of two transverse stages (PI miCos GmbH, PLS-85) for raster scan and one vertical stage (THK, KR15; motor: Circuit Specialists, 28BYG201) for dynamic adjustment of the focal plane. A pulser-receiver (Olympus, 5900PR) is utilized to drive the ultrasonic transducer for SAM.

Fig. 2.8. Schematic of the ultrasound-aided multi-parametric PAM.

After the system performance test with resolution target (R1DS1P, Thorlabs) and a 7-µm carbon fiber (S-CF706-T700, CST), the phantom and *in vivo* tests were performed following a novel ultrasound-aided contour extraction procedure. Specially, this three-step procedure begins with a rapid ultrasonic scan of the region of interest. The B-scan speed and the repetition rate of the pulser-receiver are set to 5 mm/s and 1 kHz, respectively. With a relatively large scanning interval between adjacent B-scans (40 µm), which is comparable to the lateral resolution of SAM, it takes only 4 minutes to image a 6×8 mm^2 region. Then, a self-developed MATLAB program is applied to identify the depth of the maximum signal in each A-line. Integrating the depth information extracted from individual A-lines leads to a three-dimensional (3-D) map of the surface contour. Finally, the ultrasonically extracted contour map is interpolated (down to the same step sizes planned for the contour scan) and smoothed (with a span of 15% of the B-scan length) for the contour-guided multi-parametric PAM.

12

With this procedure, we tested the performance of our ultrasound-aided contour scan using a plastic ball coated with black ink (diameter: 20 mm). First, as shown in Fig. 2.9a, the surface contour of the ball was extract by a rapid SAM scan. Then, a pair of PAM images with (Fig. 2.9b) and without (Fig. 2.9c) ultrasound-aided contour scan were acquired for comparison. Visibly, the sphere-shaped ball surface shown in the conventional PAM image became flat in the contour image, due to the dynamically adjusted focal plane. Moreover, the top surface and lower periphery of the ball—which were out of focus and thus dim and fuzzy in the conventional PAM image—became bright and clear in the contour image, indicating the improvement in both sensitivity and spatial resolution. Following the phantom study, we further tested the system performance *in vivo*. Similarly, a 6×8 mm^2 region of the mouse brain was imaged by SAM to map the skull contour (Fig. 2.9d). Then, the same region of interest was imaged by our dual-contrast platform with and without the contour guidance. Since PAM and SAM shared the same acoustic detection, the concurrently acquired photoacoustic and ultrasonic images were automatically co-registered and readily fusible. As shown in Fig. 2.9e, the entire mouse skull (imaged by SAM) and underlying cortical vasculature (image by PAM) are visually flat, due to the contour-guided dynamic focusing. Better maintaining the spatial resolution and sensitivity, the contour scan clearly resolved the microvasculature near the junction of parietal and temporal cortices, which were out of the focal plane of conventional PAM (Fig. 2.9f).
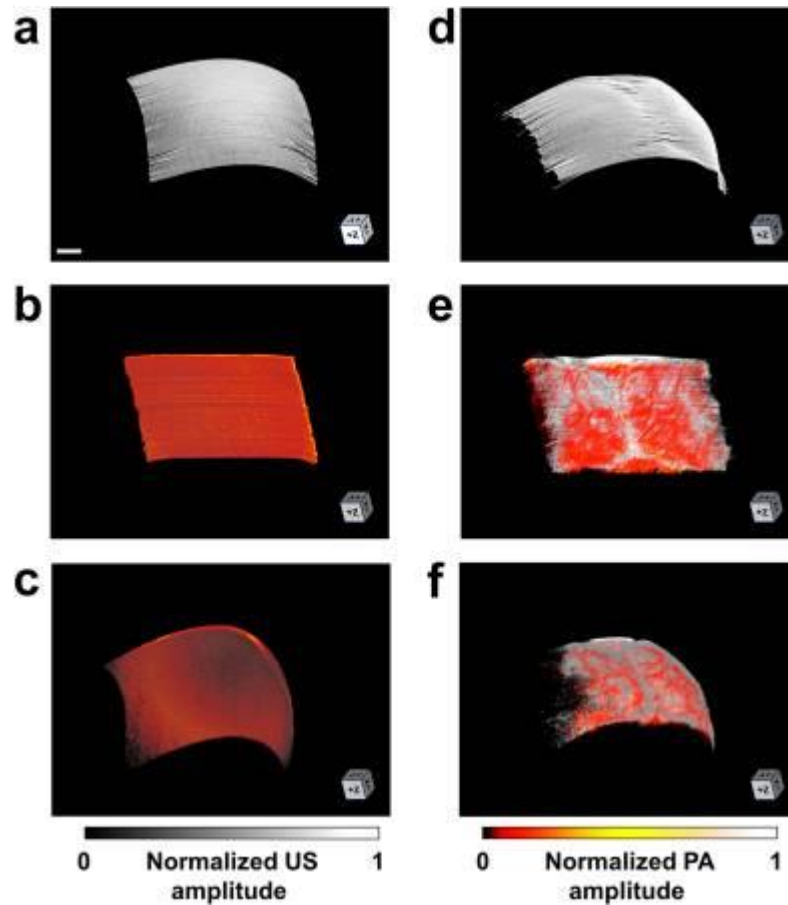
Fig. 2.9. Phantom (a-c) and *in vivo* (d-f) tests of the ultrasound-aided contour scan.

Capitalizing on the high spatial resolution and wide field of view of the ultrasound-aided contour PAM, we demonstrated—for the first time—simultaneous transcranial mapping of C_{Hb}, sO_2, and CBF over the entire mouse cortex. C57BL/6 mice (4–6 weeks old, Jackson Laboratory) were used for these *in vivo* studies. Throughout the experiments, the mice were maintained under anesthesia with 1.0–1.5% vaporized isoflurane and the body temperature was kept at 37 °C using a temperature-controlled heating pad (Cole-Parmer, EW-89802-52; Omega, SRFG-303/10). All experimental procedures were carried out in conformity with the laboratory animal protocol approved by the Animal Care and Use Committee at

the University of Virginia. Relying on the 3-D skull anatomy acquired by SAM, the vascular networks in the skull and underlying cortex were clearly separated (Fig. 2.10a). Note that the depth range (up to 400 μm) does not reflect the maximum penetration of PAM, because the maximum rather than the deepest signal is projected along each A-line.

The C_{Hb} was quantified in absolute values as shown in Fig. 2.10b. The average C_{Hb} was measured to be 113.7 ± 34.7 g/L, which was in agreement with the reported value[13]. Interestingly, the average C_{Hb} value in the skull (136.1 ± 28.7 g/L) was slightly higher than that in the cortex (100.1 ± 20.8 g/L). For the sO_2 measurement, PAM clearly identified a pair of cortical arteriole and venule partially shadowed by the microvessels in the interparietal skull (indicated by the white arrows in Fig. 2.10c). Also, PAM quantified the speed of the blood flow in individual vessels (Fig. 2.10d). It is worth noting that the blood flow in the mouse brain has both transverse and axial components, which is in contrast to the ear where blood circulates within the transverse plane (i.e., perpendicular to the imaging head). In light of this, we quantified the angle between the vessel axis and the transverse plane to derive the total CBF from its transverse component measured by the correlation analysis. Taking into consideration the relative movement between the cross-sectional scanning (i.e., B-scan) stage and RBC, PAM further determined the CBF direction by capturing the subtle difference in the relative flow speeds measured using forward and backward B-scans. As shown in Fig. 2.10d, PAM can accurately trace the direction of blood flow in individual vessels (indicated by warm and cold colors), which nicely corresponds to the sO_2 (i.e., the arterial blood flows from parent to daughter branches, while the venous blood flows oppositely). Strikingly, our PAM was able to pinpoint the direction of the blood flow in an arteriole, whose orientation

was nearly orthogonal to the B-scan axis. As indicated by the white arrow in Fig. 2.10d, the two daughter branches bifurcated from the arteriole show different colors, indicating that they were flowing toward opposite directions along the B-scan axis but both away from the parent branch.
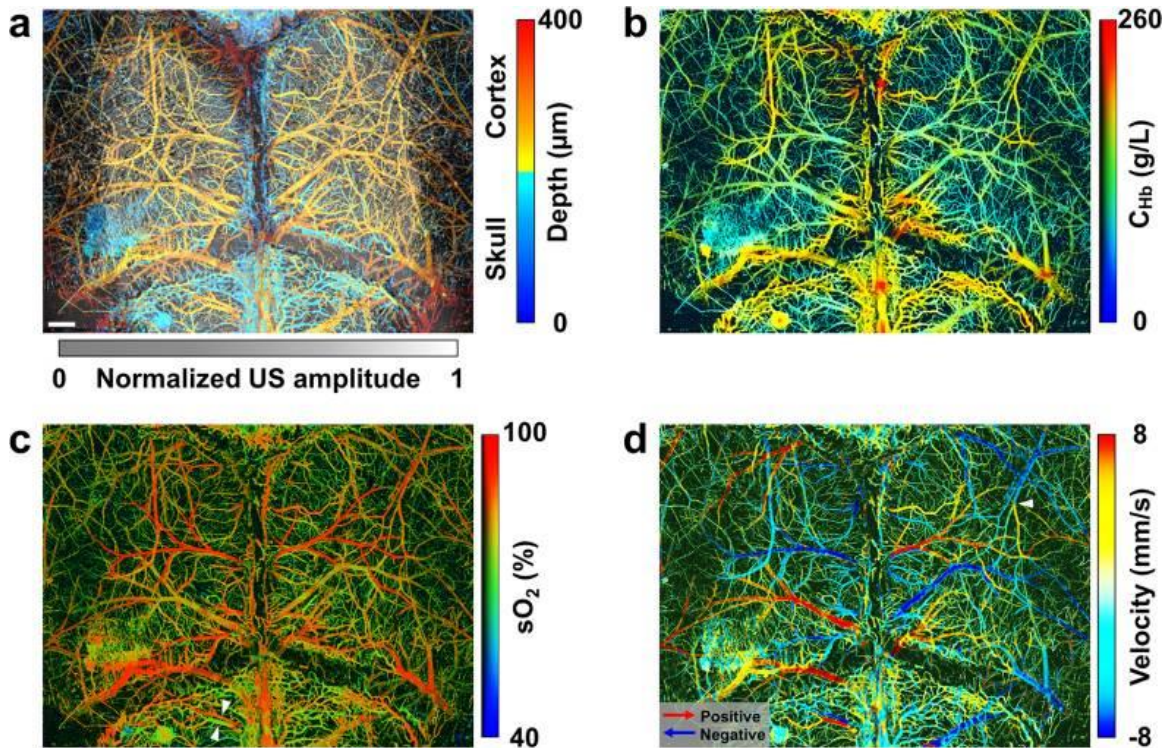
Fig. 2.10. Ultrasound-aided multi-parametric PAM of the mouse brain through the intact skull.

With the ultrasonically extracted contour map of the mouse skull, our PAM can dynamically focus on the underlying cortical vasculature when scanning across the uneven brain surface to maintain high spatial resolution and sensitivity. Statistical, spectral, and correlation analysis of the same PAM dataset allows simultaneous quantification of C_{Hb}, sO_2, and CBF at the microvascular level. Taking advantage of bi-directional raster scan, our PAM can further determine the direction of blood flow in individual vessels.

16

2.4.2 Real-time contour multi-parametric PAM

In the previous setting, the scanning process was divided into three sequential steps: (1) perform a 2-D ultrasonic[27] or photoacoustic[28] prescan of the region of interest (ROI); (2) extract the 3-D map of the surface contour from the volumetric data acquired by the prescan; and (3) rescan the ROI with the guidance of the 3-D contour map. These additional steps (i.e., prescan and offline calculation of the surface contour map) complicate the process flow and increase the experimental time. In addition, due to the limited focus coverage of the 2-D prescan, the photoacoustic signal in the out-of-focus region (e.g., the periphery of the rodent brain) is typically weak and may even be buried in the background, adding to the challenge of accurately detecting the surface contour.

To overcome these limitations, a multi-parametric PAM implementation was developed, which is capable of extracting the surface contour in real time for large-scale, high-resolution imaging of tissues with uneven surfaces. Different from the previous contour-scanning method that requires the prescan and offline calculation of the contour map, this technique enables online extraction of the surface contour of current cross-sectional scan (i.e., B-scan) to guide the high-resolution acquisition of next B-scan, which leads to a simplified workflow (i.e., one single step rather than three sequential steps) and reduced imaging time. Moreover, the real-time extraction and application of the B-scan contour helps to keep the acquisition of sequential B-scans in focus and maintain the signal-to-noise ratio (SNR), thereby addressing the poor SNR-induced challenge in contour detection that is associated with the previous contour-scanning method.

Given the small interval (10 μm) of adjacent B-scans, their surface contours are expected to be

similar. Therefore, the surface contour of current B-scan can be extracted in real time and used to guide

the contour scanning of the next B-scan. The schematic diagram of the real-time contour scanning is

shown in Fig. 2.11.
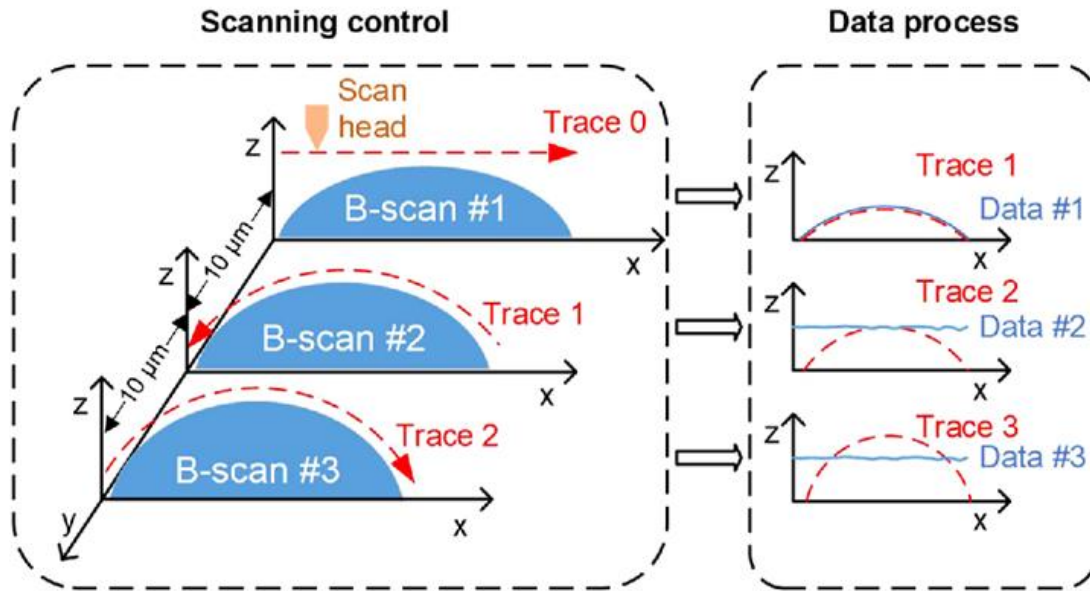
Fig. 2.11. Scheme of real-time contour scan.

The acquisition starts with a conventional B-scan (B-scan #1) along the x-axis without moving the

vertical stage. Thus, the trace of the x−z stage appears as a horizontal line, which is denoted as trace 0.

Immediately after B-scan #1, the acquired data (data #1) are processed to extract its surface contour,

which is denoted as trace 1. Then, the y stage makes a 10 μm step forward and starts B-scan #2 toward

the negative x-axis, during which the z stage moves along trace 1 in a reverse fashion. After the

completion of B-scan #2, its surface contour (trace 2) is extracted by combining trace 1 and data #2.

Similarly, B-scan #3 is acquired by following trace 2 and the surface contour (trace 3) is obtained based

on trace 2 and data #3 for the next B-scan. The same procedure is repeated until the completion of the

image acquisition.

An optically absorbing phantom with uneven surface was imaged by the PAM system to demonstrate the feasibility of the real-time contour-scan method. A piece of electrical tape (black) attached to the surface of a plastic ball, the phantom was imaged using the 2-D raster scan and the 3-D contour scan, respectively. Then, the surface contours of the tape in both images were extracted (Fig. 2.12), in which the x-axis represents the B-scan direction and "0" in the z-axis represents the position of the focal plane (negative and positive values denote that the tape is above and below the focal plane, respectively). As shown in Fig. 2.12a, the surface contour of the tape in the raster-scan image is uneven, with most of the region being out-of-focus. In contrast, the surface contour captured by the contour scan is flat, with only a 5 µm standard deviation in depth (Fig. 2.12b).
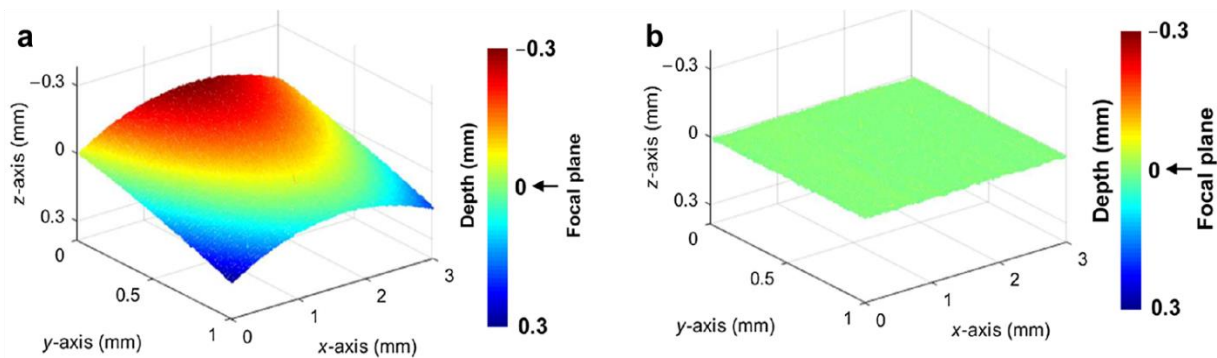
Fig. 2.12. Surface of the phantom extracted from the PAM images with (a) raster and (b) contour.

Then, the side-by-side comparison of raster scan and contour scan was further performed *in vivo*. Specifically, the entire mouse cortex was first imaged using raster scan to show the influence of the out-of-focus issue on the measurements of microvascular structure and function (i.e., C_{Hb}, sO_2, and CBF).

Then, the same ROI was reimaged using real-time contour scan to demonstrate the improvement. As shown in Fig. 2.13a, the 3-D surface contour of the mouse cortex (6mm×5mm) extracted from the experimental data acquired by raster-scan PAM shows a dome shape with a depth range of ~900 μm. In contrast, the surface contour of the same cortical ROI imaged by contour-scan PAM is relatively flat, with a 26-μm standard deviation in depth. Based on the surface contour map acquired using raster scan, the distance of each vessel away from the focal plane was quantified (Fig. 2.13b), which shows that both the central and peripheral regions of the mouse cortex were out of focus.
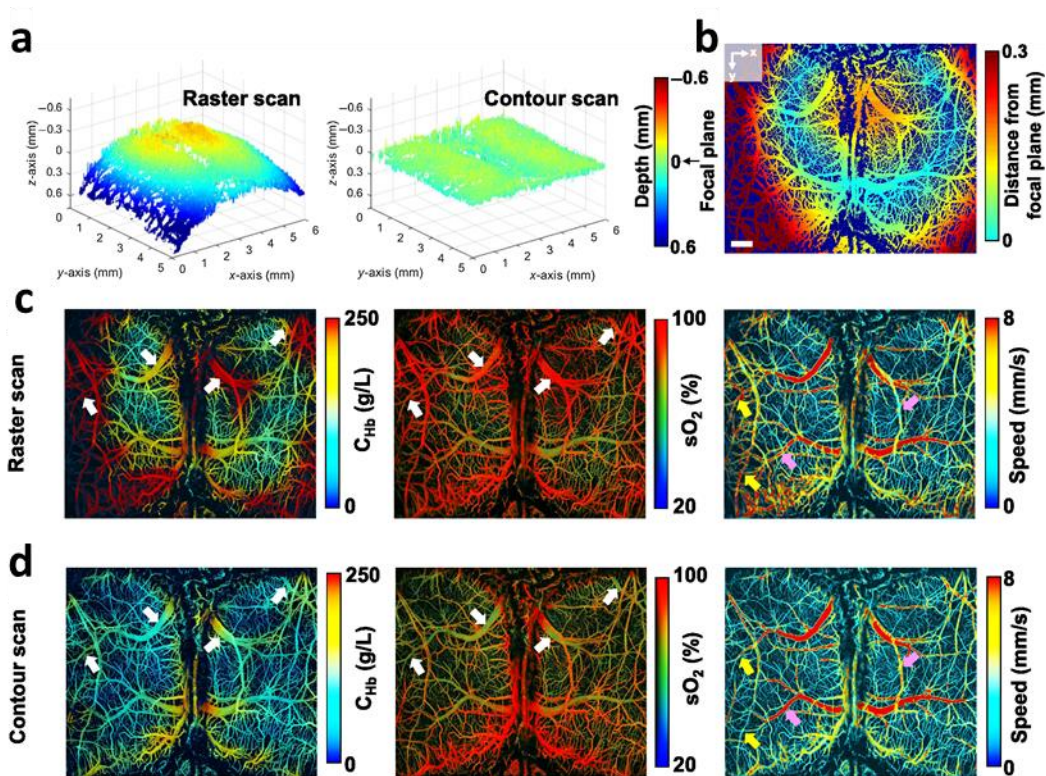
Fig. 2.13. Side-by-side comparison of raster scan and contour scan *in vivo*.

Also, side-by-side comparison of the PAM images acquired using raster scan and contour scan (Fig. 2.13c and Fig. 2.13d, respectively) clearly shows the adverse influence of the out-of-focus issue on the

20

multi-parametric hemodynamic measurements. As indicated by the white arrows, out-of-focus resulted in increased values in the C_{Hb} and sO_2 measurements. The situation in the flow measurement is more complicated, where out-of-focus could lead to either increased or decreased measurement values depending on the distance of the vessel from the focal plane (indicated by the yellow and pink arrows, respectively).

In this section, a real-time, contour-scanning, multi-parametric PAM for large-scale, high-resolution imaging of cerebral hemodynamics was developed. The performance of the system has been tested in both the phantom and the live mouse brain. Side-by-side comparison of the real-time contour scan with conventional raster scan shows that this approach can completely eliminate the inaccuracy in the structural and functional measurements induced by the out-of-focus issue in conventional PAM. This technical innovation provides a promising tool for cortex-wide functional brain imaging at the microscopic level.

2.5 Conclusion

In summary, we have developed a first-of-a-kind imaging and analysis PAM platform with the advanced multi-parametric PAM instruments and complementary analytical tools. Based on the C_{Hb} quantification method, both of the single-microvessel level and tissue level hemodynamic analysis could be achieved with the segmentation algorithm and microscopic level $MRO_2/CMRO_2$ quantification, respectively. Besides, the induction of the contour scan for the cortex-wide brain imaging also enabled cortex-wide functional brain imaging at the microscopic level for a wide range of oxygen dysfunctions including ischemic stroke and Alzheimer's disease.

Reference

[1]   Wang, T. *et al.* Multiparametric photoacoustic microscopy of the mouse brain with 300-kHz A-line rate. *Neurophotonics* **3**, 045006 (2016).

[2]   Yao, J. *et al.* High-speed label-free functional photoacoustic microscopy of mouse brain in action. *Nature Methods* **12**, 407-410 (2015).

[3]   Wang, T., Sun, N., Chen, R., Zhou, Q. & Hu, S. Isotropic-resolution photoacoustic microscopy with multi-angle illumination. *Opt. Lett.* **44**, 1-4 (2019).

[4]   Xu, Z. *et al.* Parallel Computing for Quantitative Blood Flow Imaging in Photoacoustic Microscopy. *Sensors (Basel, Switzerland)* **19** (2019).

[5]   Hu, S., Maslov, K., Tsytsarev, V. & Wang, L. V. Functional transcranial brain imaging by optical-resolution photoacoustic microscopy. *Journal of biomedical optics* **14**, 040503 (2009).

[6]   Ye, S., Yang, J., Xi, J., Ren, Q. & Li, C. Studying murine hindlimb ischemia by photoacoustic microscopy. *Chin. Opt. Lett.* **10**, 121701-121701 (2012).

[7]   Zhang, C. *et al.* Reflection-mode submicron-resolution in vivo photoacoustic microscopy. *Journal of biomedical optics* **17**, 020501 (2012).

[8]   Chen, S.-L. *et al.* Miniaturized all-optical photoacoustic microscopy based on microelectromechanical systems mirror scanning. *Opt. Lett.* **37**, 4263-4265, (2012).

[9]   Ning, B. *et al.* Simultaneous photoacoustic microscopy of microvascular anatomy, oxygen saturation, and blood flow. *Opt. Lett.* **40**, 910-913 (2015).

[10]   Ning, B. *et al.* Ultrasound-aided Multi-parametric Photoacoustic Microscopy of the Mouse Brain. *Scientific Reports* **5**, 18775 (2015).

[11]   Skeldon, A. C. *et al.* Modelling and Detecting Tumour Oxygenation Levels. *PLOS ONE* **7**, e38597 (2012).

[12]   Zhou, Y., Yao, J., Maslov, K. I. & Wang, L. V. Calibration-free absolute quantification of particle concentration by statistical analyses of photoacoustic signals in vivo. *Journal of biomedical optics* **19**, 37001 (2014).

[13]   E. Everds, N. in *The Mouse in Biomedical Research (Second Edition)*   (eds James G. Fox *et al.*) 133-XVIII (Academic Press, 2007).

[14]   Zijlstra, W. G., Buursma, A. & van Assendelft, O. W. *Visible and Near Infrared Absorption Spectra of Human and Animal Haemoglobin: Determination and Application*.   (Taylor & Francis, 2000).

[15]   Huang, W., Yen, R. T., McLaurine, M. & Bledsoe, G. Morphometry of the human pulmonary vasculature. *Journal of Applied Physiology* **81**, 2123-2133 (1996).

[16]   Bate, H. Blood viscosity at different shear rates in capillary tubes. *Biorheology* **14**, 267-275 (1977).

[17]   Russell, E. S., Neufeld, E. F. & Higgins, C. T. Comparison of Normal Blood Picture of Young Adults from 18 Inbred Strains of Mice. *Proceedings of the Society for Experimental Biology and Medicine* **78**, 761-766 (1951).

[18]   Cho, Y. I. & Kensey, K. R. Effects of the non-Newtonian viscosity of blood on flows in a diseased

arterial vessel. Part 1: Steady flows. *Biorheology* **28**, 241-262 (1991).

[19]   Bird, R. B., Armstrong, R. C. & Hassager, O. *Dynamics of polymeric liquids. Vol. 1, 2nd Ed. : Fluid mechanics*.   (John Wiley and Sons Inc.,New York, NY, 1987).

[20]   Yao, J., Maslov, K. I., Zhang, Y., Xia, Y. & Wang, L. V. Label-free oxygen-metabolic photoacoustic microscopy in vivo. *Journal of biomedical optics* **16**, 076003 (2011).

[21]   Xu, F., Liu, P., Pascual, J. M., Xiao, G. & Lu, H. Effect of hypoxia and hyperoxia on cerebral blood flow, blood oxygenation, and oxidative metabolism. *Journal of cerebral blood flow and metabolism : official journal of the International Society of Cerebral Blood Flow and Metabolism* **32**, 1909-1918 (2012).

[22]   Shih, A. Y. *et al.* Active dilation of penetrating arterioles restores red blood cell flux to penumbral neocortex after focal stroke. *Journal of cerebral blood flow and metabolism : official journal of the International Society of Cerebral Blood Flow and Metabolism* **29**, 738-751 (2009).

[23]   Nishimura, N., Schaffer, C. B., Friedman, B., Lyden, P. D. & Kleinfeld, D. Penetrating arterioles are a bottleneck in the perfusion of neocortex. *Proc Natl Acad Sci U S A* **104**, 365-370 (2007).

[24]   Piiper, J. & Scheid, P. Diffusion limitation of O2 supply to tissue in homogeneous and heterogeneous models. *Respiration Physiology* **85**, 127-136 (1991).

[25]   Braitenberg, V. & Schüz, A. *Cortex: Statistics and Geometry of Neuronal Connectivity*. (Springer Berlin Heidelberg, 2013).

[26]   Srinivasan, V. J. *et al.* Quantitative cerebral blood flow with optical coherence tomography. *Optics express* **18**, 2477-2494 (2010).

[27]   Kallinowski, F. *et al.* Blood flow, metabolism, cellular microenvironment, and growth rate of human tumor xenografts. *Cancer research* **49**, 3759-3764 (1989).

[28]   Kimmel, E. R. *et al.* Absence of Collaterals is Associated with Larger Infarct Volume and Worse Outcome in Patients with Large Vessel Occlusion and Mild Symptoms. *Journal of stroke and cerebrovascular diseases : the official journal of National Stroke Association* **28**, 1987-1992 (2019).

Chapter 3 *In vivo* imaging of hemodynamic redistribution and arteriogenesis across microvascular network

3.1 Introduction

Arterial occlusion can result in severe ischemia in downstream tissues, if collateral vessels are absent or of insufficient size[1,2]. Arteriogenesis, diameter enlargement of pre-existing artery-to-artery anastomoses or collateral vessels, is an essential mechanism that contributes to the restoration of blood oxygen supply in ischemic tissues following the onset of occlusion[3]. The response of collateral vessels to ischemia has been widely studied, and it has been shown that a sustained increase in the wall shear stress experienced by collaterals activates endothelial cells and leads to arteriogenesis[4]. However, being able to predict relative remodeling potential of individual collateral vessels within a complex microvascular network remains elusive, as these vessels can run in parallel within arterial arcades and exhibit remodeling responses that are distinct. While changes in fluid shear stress are known to drive arteriogenesis post-injury, a baseline characteristic of the collateral vessels, which influences the differential growth responses *in vivo*, has not yet been elucidated.

To date, it remains a challenge to comprehensively quantify the hemodynamics in individual microvessels across a remodeling network *in vivo*. Although multiple optical technologies—such as LSCI and TPM[5,6]—have been developed to quantify microvascular hemodynamics, they have fundamental limitations. LSCI can only access relative changes in blood flow and lacks the spatial resolution and contrast to resolve small resistance arterioles and capillaries[5]. TPM requires exogenous contrast agents to visualize microvascular structure and function, which may cause perturbations to the

natural physiology of the microcirculation and discourages chronic monitoring[7]. Moreover, the long lifetime of the phosphorescence agent required for TPM of blood oxygenation significantly limits its speed[8], making network-wide hemodynamic imaging impractical. Capitalizing on the strong optical absorption of blood hemoglobin, the primary oxygen carrier in the circulation, PAM is well suited to fill this technology void[9]. Recent advances in PAM have enabled simultaneous label-free imaging of microvascular anatomy, C_{Hb}, sO_2, and blood flow velocity (i.e., both flow speed and direction)[10,11].

Here, we have developed a hardware-software platform by integrating PAM and advanced image analysis for comprehensive assessment of network-wide hemodynamic redistribution and microvascular remodeling in a mouse model of arterial ligation[12]. Capitalizing on the label-free nature and noninvasiveness of PAM, we longitudinally monitored the ear microvasculature, including structure, C_{Hb}, sO_2 and blood flow velocity, for 21 days after ligation. With the aid of segmentation analysis (i.e., obtaining the hemodynamic parameters of individual vessels by segmenting them from the microvascular network), multifaceted collateral remodeling in both the structure (i.e., diameter, tortuosity, resistance, and wall shear stress) and function (i.e., blood perfusion, oxygenation, flow, and oxygen supply) was comprehensively quantified at the single-microvessel level. The utility of this enabling technology was demonstrated by studying the influence of obesity on the ligation-induced microvascular remodeling. Furthermore, our serial monitoring of individual remodeling collaterals *in vivo* provides direct evidence that collateral baseline resistance influences the degree of remodeling experienced by said collateral following chronic up-stream occlusion.

3.2 Material and methods

3.2.1 Animals

C57BL/6BrdCrHsd-*Tyr*^c (C57BL/6 albino) mice (female, 30 weeks old, Envigo) were used for longitudinally monitoring network-wide hemodynamic redistribution and collateral, studying the relationship between the initial vascular resistance and the extent of collateral remodeling, and studying microvascular remodeling in the high-fat diet-induced obesity model. In this model, the animals were fed on either normal or high-fat diet (Research Diets, D12451) starting at 6 weeks of age for 24 weeks before ligation surgery. SKH1-Hrhr mice (male, 20 weeks old, Charles River) were used for studying the competition of parallel collaterals remodeling within an individual microvascular network. SKH1-Hrhr mice (male, 20 weeks old, Charles River) and BALB/c mice (male, 20 weeks old, Charles River) were also used for studying the relationship between the initial vascular resistance and the extent of collateral remodeling. All animal procedures were carried out in conformity with the protocols approved by the Animal Care and Use Committee at the University of Virginia.

3.2.2 Mouse model of arterial ligation

The ligation procedure was adapted and modified from Billaud et al.[12] Briefly, depilation of the mouse ear was performed 24 hours prior to the initial PAM experiment. Mice were anesthetized with 1.5% isoflurane. Following sterile preparation, both the central and anterior (towards snout) primary feeding arteries were surgically ligated[12], leaving the posterior (towards tail) feeding artery intact (Fig. 3.1). The anterior feeding artery was ligated as close to the base of the ear as possible, proximal to any bifurcations in the lobe. Incisions were closed with cyanoacrylate glue. The animals used for technical demonstration

of segmentation-based single-vessel analysis and multi-parametric quantification of collateral remodeling received ligation of the central feeding artery only. We sought to induce a larger shear stress change in collateral vessels with the double-ligation surgery; however, our analysis did not reveal any significant differences compared to single ligation of the central feeder only.
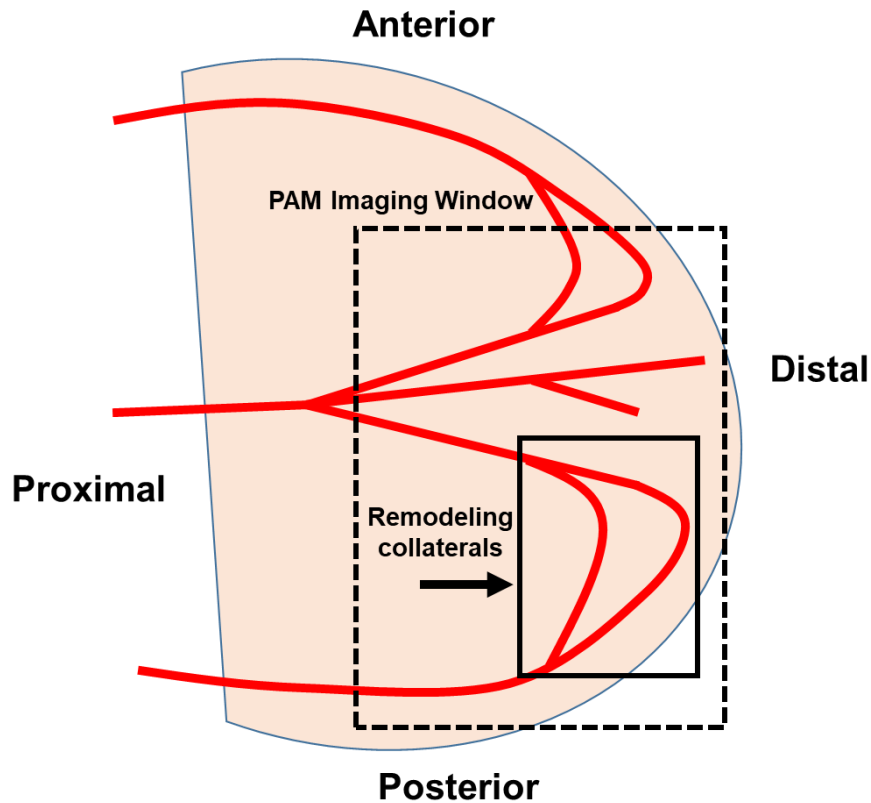
Fig. 3.1. Schematic of ear ligation with both the middle and anterior feeding arteries ligated.

3.2.3 PAM system

As shown in Fig. 3.2a, two nanosecond-pulsed lasers (Edgewave, BX40-2-G and BX40-2-GR; wavelengths: 532 and 559 nm; repetition rate: up to 30 kHz) were used for simultaneous multi-parametric PAM of C_{Hb}, sO_2, and blood flow at the microscopic level. Two neutral-density filters (NDF; Thorlabs,

27

NDC-50C-2M) were used to attenuate the two laser outputs, respectively. Then, the two beams with orthogonal polarization states were combined using a polarizing beam splitter (PBS; Edmund optics, 48-545). To compensate for the fluctuation in laser intensity, ~5% of the laser energy was tapped off by a beam sampler (BS; Thorlabs, BSF10-A) and monitored by a high-speed photodiode (PD; Thorlabs, FDS100). The combined beam was then coupled into a single-mode fiber (SMF; Thorlabs, P1-460B-FC-2) through an objective lens (Newport, M-10X) and delivered to the scanning head (Fig. 3.2b), where two identical doublets (DL; Thorlabs, AC127-025-A) were used to map the fiber output into the tissue to be imaged. A ring-shaped ultrasonic transducer (UT; inner diameter: 2.2 mm; outer diameter: 4.0 mm; center frequency: 35 MHz; 6-dB bandwidth: 70%) was used for convenient confocal alignment of the optical excitation and ultrasonic detection. For acoustic coupling, the transducer was immersed in a water tank. A correction lens (CL; Thorlabs, LA1207-A) was placed before the transducer to compensate for the optical aberration at the air-water interface. The scanning head was mounted on a 3-axis motorized linear stage system, with two transverse stages (PI GmbH & Co. KG, PLS-85) for bi-directional raster scan and a vertical stage (THK, KR15) for automated adjustment of the focal plane. A self-developed LabVIEW program was used to synchronize the laser triggers, photodiode monitoring, stage movement, and data acquisition by a digitizer (AlazarTech, ATS9350). The acquired data were arranged into individual depth-resolved A-lines (i.e., the time-resolved photoacoustic signal excited by each laser pulse, profiling the one-dimensional depth distribution of vessel cross-sections within the laser excitation zone), with multiple A-lines forming a B-scan (i.e., a combination of multiple A-lines collected by scanning across the tissue, forming a two-dimensional cross-sectional view of the vasculature; Fig. 3.2c).
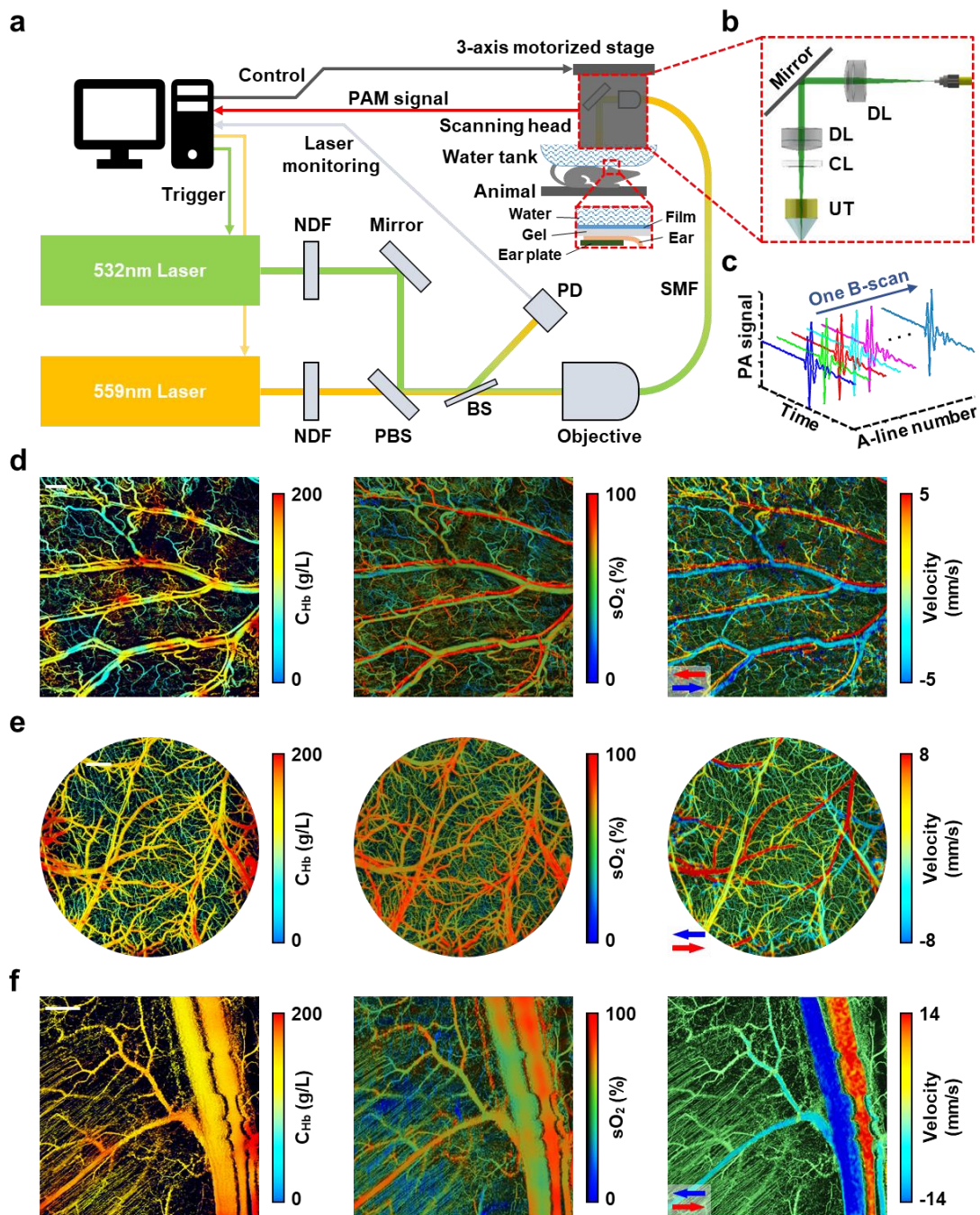
Fig. 3.2. Multi-parametric PAM in the hardware-software platform. (a) System schematic, (b) Blow-up of the scanning head boxed in (a). (c) Sequentially acquired A-line signals for multi-parametric quantification. Multi-parametric PAM of (d) the mouse ear, (e) the mouse brain, and (f) the mouse hindlimb (scale bars: 500 μm). The red and blue arrow pairs in (d–f) indicate the flow directions.

Using this enabling technology, we have achieved simultaneous imaging of the microvascular C_{Hb}, sO_2 and blood flow velocity in the mouse skin (e.g., the ear; Fig. 3.2d), brain (Fig. 3.2e) and muscle (e.g., the hind limb; Fig. 3.2f). The multi-parametric images show clearly resolved microvascular networks in these tissue sites, with clear differences in sO_2 and flow direction between arteries/arterioles and veins/venules. These results demonstrate the broad applicability of multi-parametric PAM to study the microvascular network *in vivo*. The mouse ear was chosen for this study predominantly for the accessibility of the feeding arteriole(s) to ligation and the ability to serially image the microvasculature throughout ear without further surgical intervention (e.g. installation of a window chamber).

3.2.4 Procedures for PAM imaging

The mouse ear was placed on a home-made plastic plate and in gentle contact with the water tank, which was filled with temperature-maintained (37°C) deionized water. For effective acoustic coupling, thin layers of transparent ultrasound gel were applied between the ear, the plate, and the plastic membrane at the bottom of the water tank. Throughout the PAM experiment, the mouse was maintained under general anesthesia with 1.0–1.5% isoflurane and the body temperature was kept at 37°C using a temperature-controlled (Cole-Parmer, EW-89802-52) heating pad (Omega, SRFG-303/10). For chronic monitoring of the microvascular network, the ear was repeatedly imaged before, right after, and up to 21 days following the arterial ligation. Note that the acquisition of blood flow requires dense spatial sampling, and thus is relatively time consuming. For an area of 6×6 mm^2 (e.g., Fig. 3.5), the total acquisition time is ~68 minutes.

3.2.5 Statistical analysis

The two-way repeated measures ANOVA was used to compare the microvascular remodeling in the obese and control mice in Fig. 3.11. The parallel-line statistical test was used to compare the line slopes in Fig. 3.12. For multiple comparisons between groups at a certain time point in Fig. 3.11, the Tukey correction was used to control the Type I error rate differences. In all statistical analysis, $p < 0.05$ was considered significant. All data were presented in the form of mean $\pm$ standard deviation.

3.3 Results

3.3.1 Longitudinal monitoring of network-wide hemodynamic redistribution and collateral remodeling

Capitalizing on the wide field of view of multi-parametric PAM (i.e., up to 20 mm^2), we performed simultaneous imaging of C_{Hb}, sO_2 and blood flow speed over the entire mouse ear before, immediately following, and up to 21 days after arterial ligation (Fig. 3.3a–c). Right after the ligation, a dramatic decrease in the blood flow speed was observed in the occluded feeding artery (yellow arrows in Fig. 3.3c). In contrast, the flow speeds in the two unligated feeding arteries (white arrows in the insets of Fig. 3.3c), which are of the same order as the ligated artery, started to elevate and ultimately (on day 21) became much higher than the corresponding flow speeds before ligation. Accompanying the redistribution of blood flow was the change in sO_2. In response to the ligation-induced ischemia, there was an immediate decrease in the sO_2 of the downstream microvasculature (circled area in Fig. 3.3b). The tissue hypoxia in this individual was gradually mitigated after three days, likely due to the observed increase in blood flow through the collateral vessels during this time. Not surprisingly, there was no significant change in C_{Hb} in response to the ligation (Fig. 3.3a). However, some collaterals that were

poorly perfused and thus barely visible before ligation were 'recruited' for the hemodynamic

redistribution afterwards (white arrows in the insets of Fig. 3.3a).
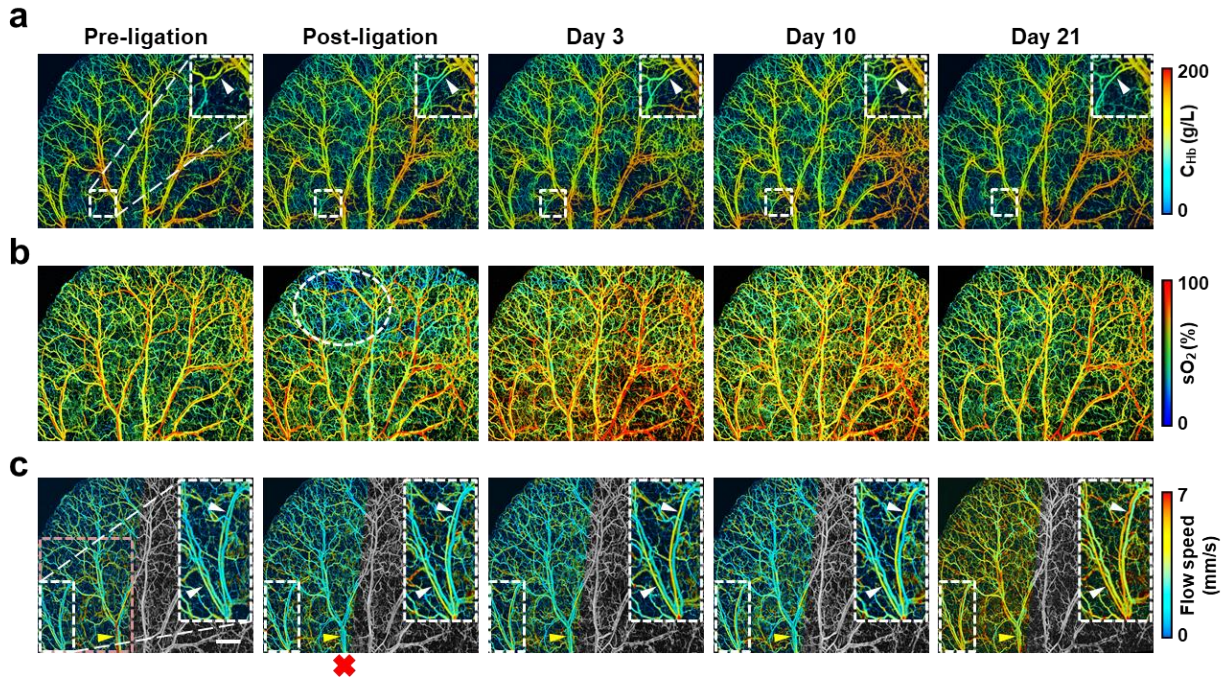
Fig. 3.3. Longitudinal monitoring of hemodynamic redistribution and collateral remodeling across a microvascular network. (a–c) Multi-parametric PAM of C_{Hb}, sO_2 and blood flow speed in the mouse. ear before, right after, and up to 21 days following the arterial ligation (scale bar: 1mm). The red cross in (c) indicates the ligated arteriolar tree, and the ligation site lies outside PAM images. The insets in (a, c) are the blowups of the white boxed regions at the lower left corners of the two panels.

With the aid of vessel segmentation, we were able to dynamically quantify the network-wide

microvascular remodeling in terms of diameter alterations and blood flow speed changes at the single-

vessel level. As shown in Fig. 3.4a, about two-thirds of the arteries/arterioles in the microvascular

network showed noticeable vasodilation (up to 65.0%; highlighted in green) immediately after ligation.

Despite diameter reduction in some instances on day 3, over half of the microvessel segments reached

their maximum diameters on day 10. Interestingly, the diameters of most enlarged collaterals decreased on day 21.
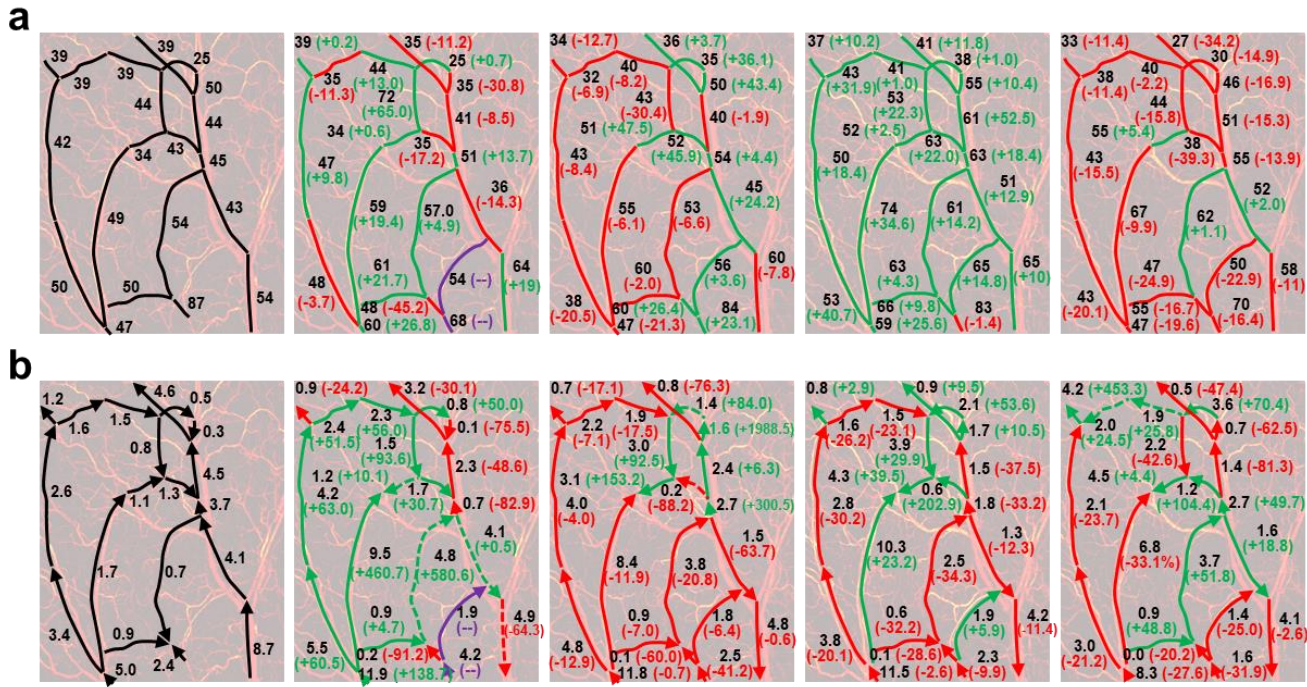
Fig. 3.4. Single-vessel analysis of collateral remodeling in (a) diameter and (b) volumetric blood flow over the yellow boxed region in Fig. 3.3c. Data are shown in absolute value (a: μm, b: nL/s), as well as the relative changes (%) between two adjacent time points in brackets. Increased and decreased values are labeled in green and red, respectively. Purple is used to label vessel segments that are missing in one of the two time points. In (b), solid and dashed lines indicate segments without and with reversed flow direction, respectively. Arrows indicate the flow direction.

In contrast to the remodeling in collateral vessel diameter, which peaked on day 10, adaptations of the hemodynamics occurred in a more acute fashion. As shown in Fig. 3.4b, a network-wide increase in collateral blood flow speed was observed right after the ligation (up to 580.6%; highlighted in green) in response to the altered pressure gradients following ligation. Along with the increased flow speed, the

flow directions in the collateral exhibiting the maximum flow increase (i.e., 580.6%), the ligated feeding

artery, and its daughter branch were all reversed (highlighted in dashed lines), redirecting the blood flow

from the adjacent, perfused region to the ligated region. The flow redistribution across the microvascular

network continued from day 3 through day 21.

As a control experiment, we repeated the longitudinal monitoring in the mouse ear with unperturbed

microvascular network (Fig. 3.5 and Fig. 3.6). Our results showed no changes in the vascular structure

and hemodynamics throughout the 21-day monitoring period.
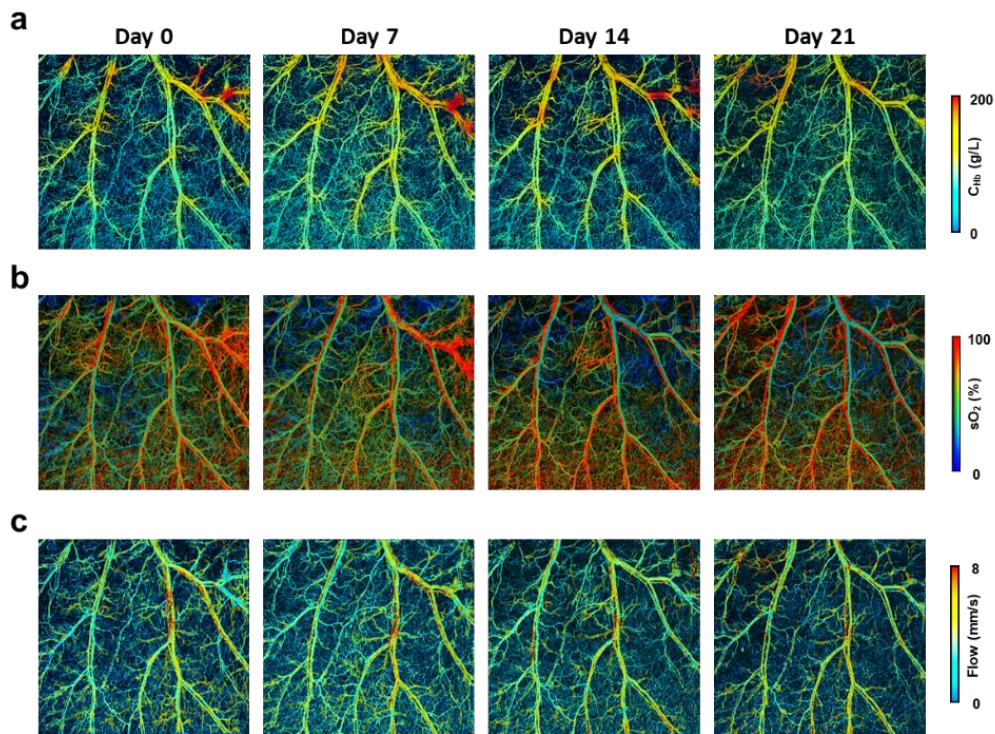
Fig. 3.5. Reproducibility of Multi-parametric PAM in unperturbed microvascular network in the mouse ear without ligation surgery.
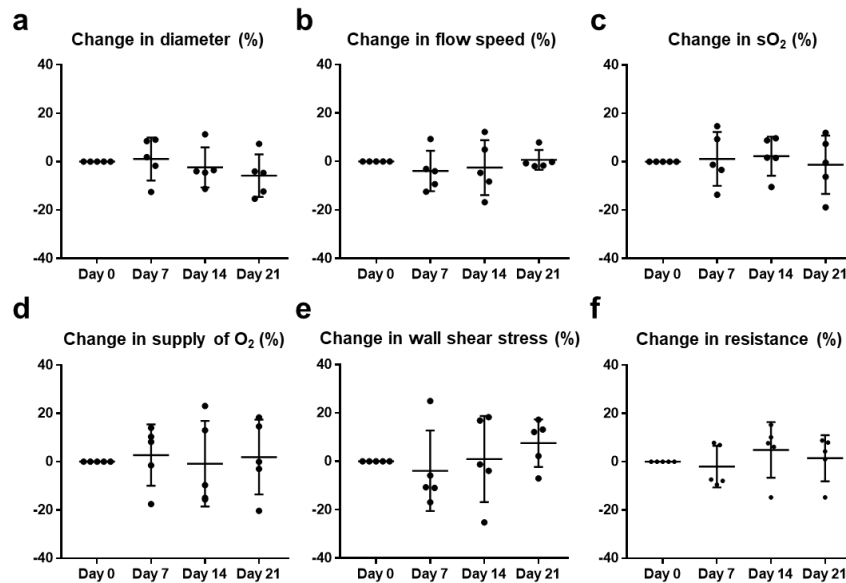
Fig. 3.6. Single-vessel analysis of the mouse ear without ligation surgery in (a) vessel diameter, (b) blood flow speed, (c) sO_2, (d) blood oxygen supply, (e) wall shear stress, and (f) vascular resistance, respectively.

3.3.2 Multi-parametric analysis of the competition in collateral remodeling

Combining the multi-parametric measurements and segmentation analysis, the hardware-software platform enabled us to comprehensively and dynamically characterize the differential response in remodeling between collaterals that perfuse a complex microvascular network. As shown in Fig. 3.7a, we performed arterial ligation in a mouse ear (the secondary arteriolar branches off the ligated primary feeding arteriole are indicated by a red cross) and then monitored the remodeling of three parallel collaterals (pseudo-colored in red, green and blue, respectively) for 21 days. Notably, the three parallel collaterals exhibited different structural characteristics prior to the ligation. For example, their diameters prior to ligation were 29 μm, 36 μm, and 34 μm; and their lengths were 2.75 mm, 7.02 mm, and 7.88

mm. Even though each parallel collateral had the opportunity to experience a change in blood flow-induced shear stress as a result of the redistributed blood flow due to the ligation, the segmentation-based single-vessel analysis revealed striking differences in the remodeling responses of the three vessels. Structurally, comparable levels of vasodilation were observed in all three collaterals right after ligation. However, diameter changes started to differentiate after 3 days. At the end of the 21-day monitoring, the proximal collateral (labeled in red) showed the strongest remodeling response, which was 1.5-folder and 3.2-folder higher than those of the medial collateral (green) and distal collateral (blue), respectively (Fig. 3.7b). In contrast to the substantial diameter change, the relative changes in tortuosity were smaller, but still notable. Functionally, the proximal collateral showed an acute and pronounced increase in the blood flow right after ligation, which contributed most significantly to the timely redistribution of blood supply and was distinct from the delayed flow increase in the medial collateral and the decrease in the distal collateral. Moreover, while the flow in the proximal collateral remained at a high level throughout the 21-day period, the flow in the medial collateral gradually diminished after peaking on day 3 (Fig. 3.7c). Along with the flow upregulation was the sO_2 increase in the proximal and medial collaterals. Similar to the flow response, the sO_2 change in the distal collateral was opposite to those in the other two collaterals, decreasing right after ligation and gradually returning to the pre-ligation level after 21 days (Fig. 3.7d). Together, the changes in the structural and functional parameters led to a boost in oxygen supply through the proximal collateral, which was 2.3-fold and 14.1-fold higher than those through the medial and distal collaterals, respectively (Fig. 3.7e). Overall, these results revealed the dynamic differential remodeling responses in the remodeling of the three collaterals, with the proximal collateral remodeling the most and

the distal collateral the least.

Given that wall shear stress is a regulatory factor of arteriogenesis[13], we compared the shear stress values of the three competing collaterals. As expected, the shear stress increased significantly in the proximal and medial collaterals after ligation and then gradually returned to the baseline levels by day 21. The proximal collateral, which experienced the largest increase in shear stress, exhibited the most pronounced arteriogenesis; and the distal collateral that experienced decreased shear stress over time showed the weakest (Fig. 3.7f). Given that arteriogenesis leads to reduced vascular resistance[13], we also
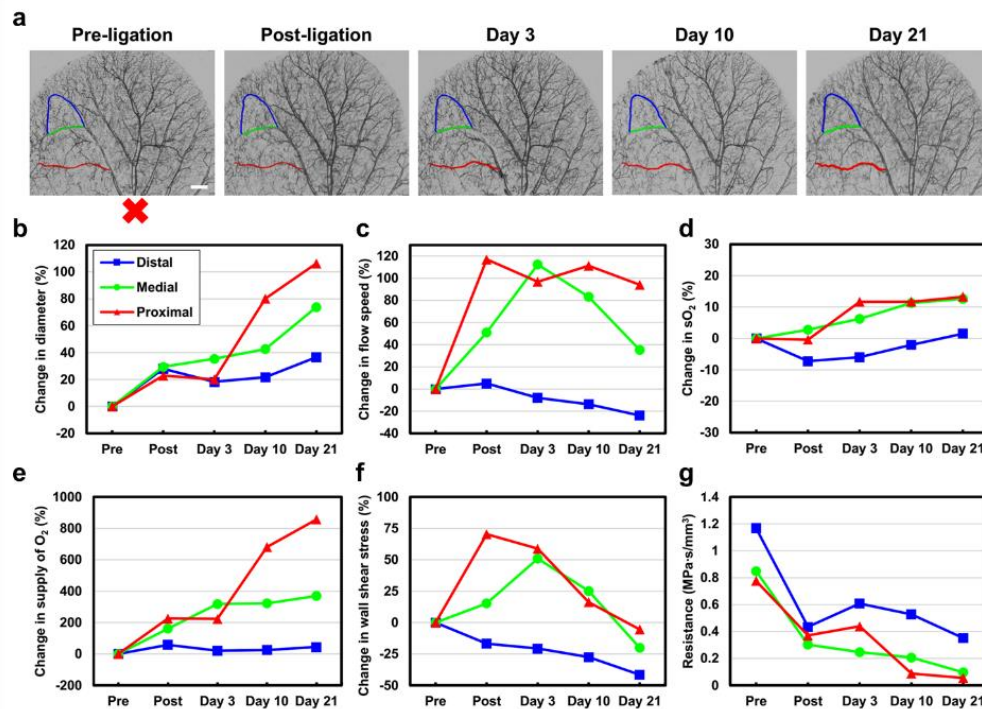
Fig. 3.7. Multi-parametric analysis of the competition in collateral remodeling. (a) Longitudinal monitoring of the ear microvascular network before, right after, and up to 21 days following the arterial ligation (scale bar: 1mm). The three collateral arterioles are labeled in red, green and blue, respectively. Red cross indicates the ligated arteriolar tree. (b–g) Multifaceted collateral remodeling quantified as relative changes (%) in vessel diameter, blood flow speed, sO_2, blood oxygen supply, wall shear stress, and vascular resistance, respectively.

examined the dynamic changes in the resistances of the three collaterals. Indeed, all of them showed

reduced vascular resistance over the 21-day period (Fig. 3.7g).

3.3.3 Correlation between initial vascular resistance and collateral remodeling

Interestingly, in Fig. 3.7b–g, the proximal and medial collaterals with much lower initial resistances

showed a significantly greater extent of arteriogenesis compared to the distal collateral. To examine

whether vascular resistance is a factor that influences differential collateral remodeling in a

microvascular network containing multiple collaterals, we analyzed the relationship between the initial

resistance and key remodeling parameters, including the vessel diameter, tortuosity, volumetric blood

flow, and wall shear stress. Our results showed a strong negative correlation between the initial resistance

and each of these structural and functional parameters. Collaterals with lower initial resistances tended

to have larger diameter increases after 21 days (Fig. 3.8a), more pronounced blood flow increases (Fig.

3.8b), larger increases in tortuosity (Fig. 3.8c), and greater elevation in the wall shear stress post-ligation

(Fig. 3.8d).
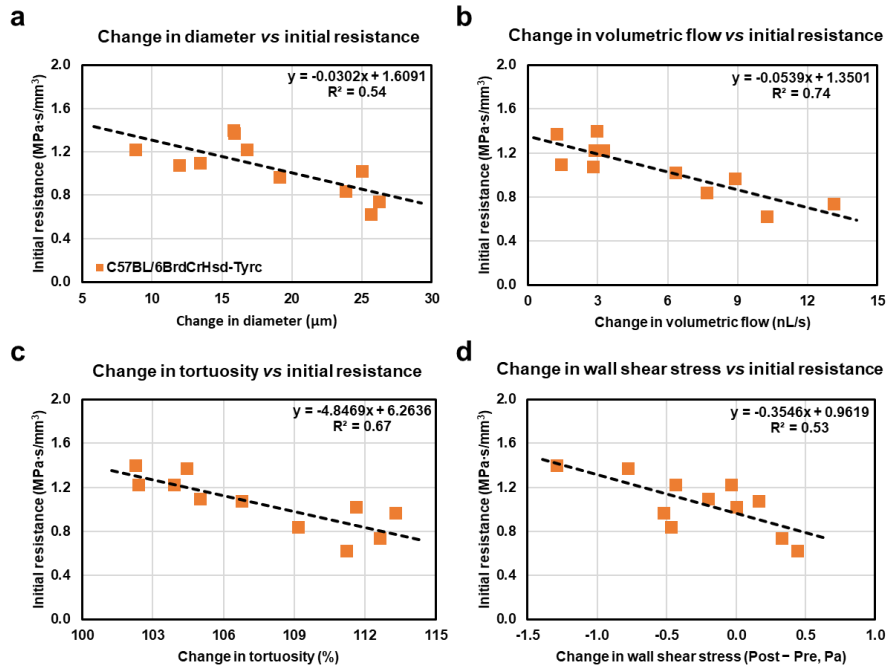
Fig. 3.8. Relationship between initial vascular resistance and the extent of collateral remodeling. (a-d) Inverse correlation between initial resistance and changes in vessel diameter, volumetric blood flow, tortuosity and wall shear stress, respectively. The analyses are based on 11 collateral arterioles from 6 mice.

Overall, the multifaceted structural and functional remodeling of the collateral microvessels showed strong dependence on the initial resistance. The lower the resistance of the collateral vessel pre-ligation, the more extensive the diameter enlargement that occurred in the vessel by day 21. To ensure the generality of the correlation analysis, we repeated this study in two other mouse strains (i.e., male SKH1-Hrhr and male BALB/c). As shown in Fig. 3.9, the linear relationship between initial resistance and extent of collateral remodeling holds across all three different strains and both sexes.
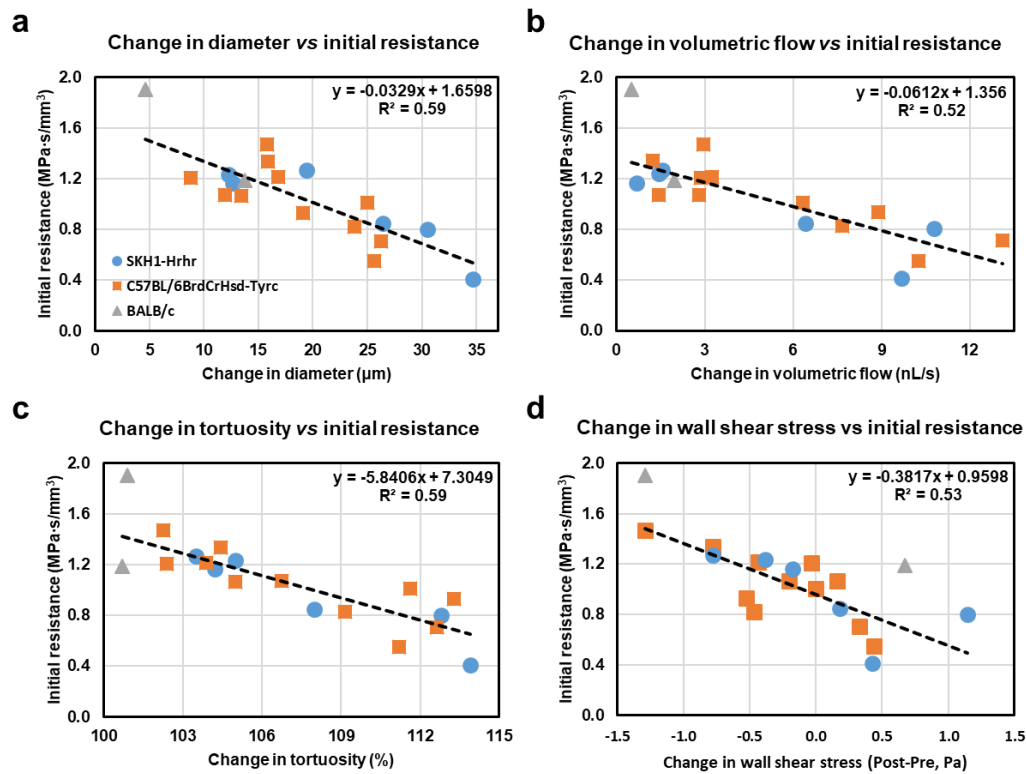
Fig. 3.9. Relationship between initial vascular resistance and the extent of collateral remodeling. (a–d) Inverse correlation between initial resistance and changes in vessel diameter, volumetric blood flow, tortuosity and wall shear stress, respectively. The analyses are based on 19 collateral arterioles from 10 mice of 3 different strains.

3.3.4 Characterization of disease-induced impairment in collateral remodeling

To demonstrate the utility of this platform for understanding how microvascular remodeling is impaired in diseases, we longitudinally monitored the ligation-induced hemodynamic changes in both control (body weight: 22.8±0.5 g; Fig. 3.10a) and obese mice (body weight: 44.3±1.3 g; Fig. 3.10b). Representative collateral remodeling was highlighted in Fig. 3.10c and Fig. 3.10d, which are the blowups of the boxed region in Fig. 3.10a and Fig. 3.10b, respectively. To better visualize the changes at the

40

microscopic level, we removed the trunk vessels using segmentation and extrapolated the microvascular

measurements to the tissue level based on the established oxygen diffusion model and the blood-flow

reduction model[14,15]. As shown in Fig. 3.10e, more severe tissue hypoxia (highlighted by dashed circles)

and much weaker flow increase were observed in the obese mouse right after the ligation. Through the

21-day collateral remodeling, the blood oxygenation in the control mouse was completely recovered to

the pre-ligation level, while the obese mouse remained hypoxic. Moreover, the microvascular flow in the

control mouse was first significantly increased (up to 112.5%) and then partially regressed over the 21

days, in contrast to the moderately upregulated flow (up to 36.8%) in the obese mouse.
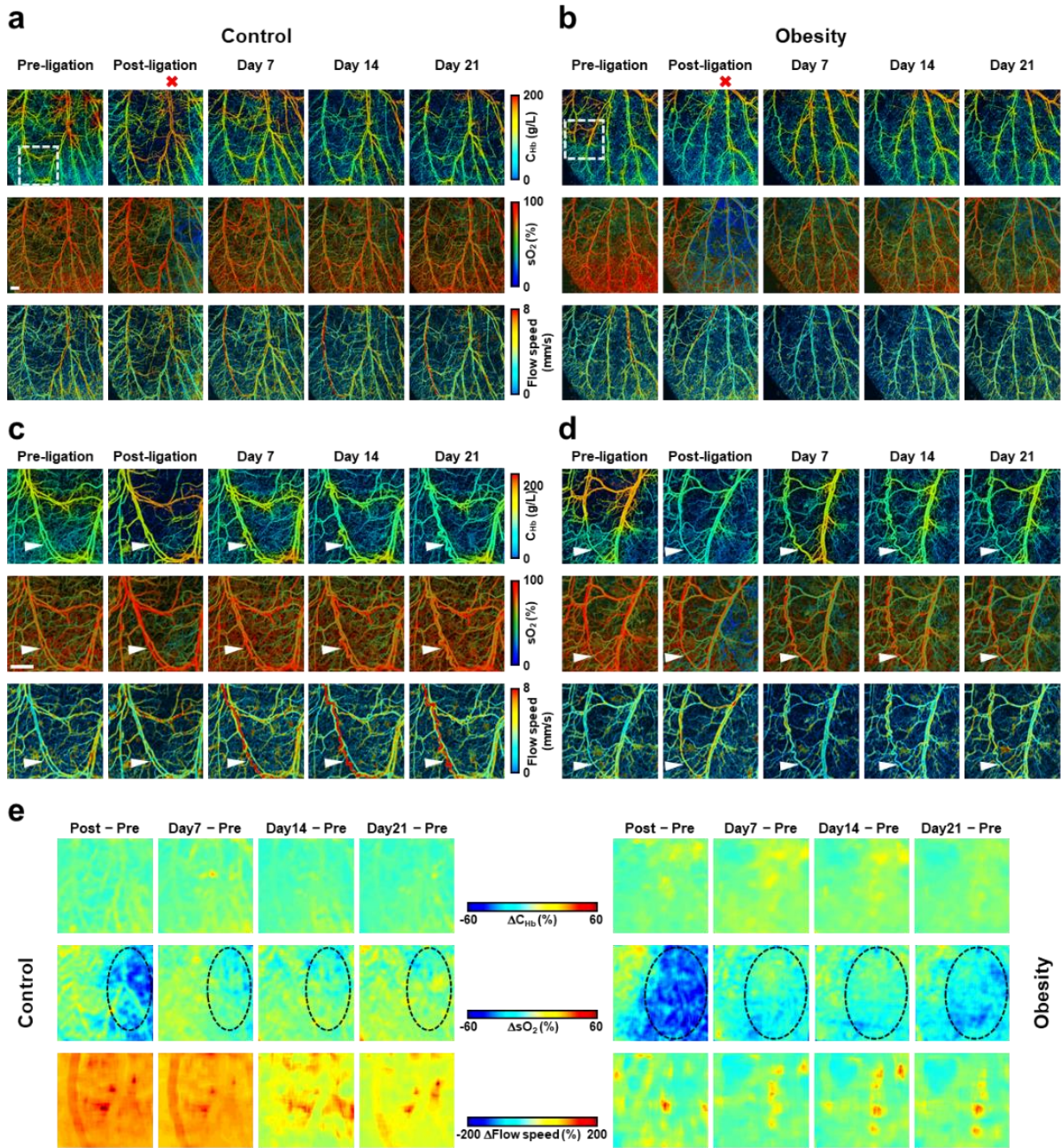
Fig. 3.10. Influence of obesity on the ligation-induced hemodynamic redistribution. (a, b) Multi-parametric PAM images. The red crosses in (a) and (b) indicate the ligated arteriolar trees, and the ligation site lies outside PAM images. (c, d) Blowups over the white boxed region in (a) and (b). White arrows: remodeling collateral vessels. (e) Tissue-level hemodynamic responses to the ligation extracted by taking the differences between the measurements acquired at each of the post-ligation points and that acquired before ligation. Black dash area: the hypoxia region (scale bar: 500μm).

Single-vessel analysis revealed that, compared to the control mice, the obese mice showed less pronounced and less sustained increases in the collateral diameter (Fig. 3.11a), blood flow (Fig. 3.11b), and tortuosity (Fig. 3.11c) in response to the arterial ligation throughout the monitoring period, with most striking differences after 14 days. Due to the impaired remodeling ability, the obese mice were never able to fully recover from the ligation-induced tissue hypoxia (i.e., the average venous sO_2 was always below the pre-ligation level as shown in Fig. 3.11d), even though there was not a difference in the pre-ligation venous sO_2 between the two groups. Note that given the considerable variability across individual animals (e.g., the diameters of the eleven vessels from six control mice spanned a wide range of 21–49 µm), normalized rather than absolute changes from the corresponding baseline values were analyzed.
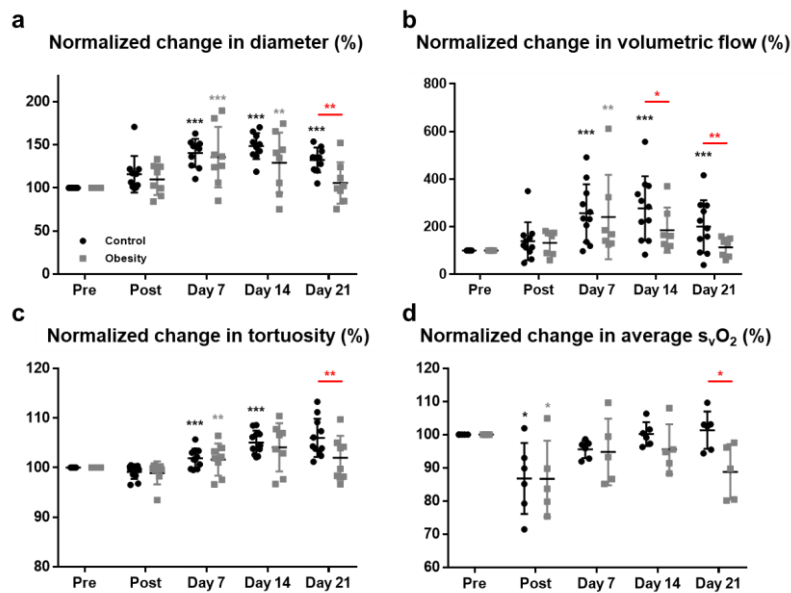
Fig. 3.11. Influence of obesity on the ligation-induced remodeling in microvascular structure and function. Colored asterisks indicate the statistical significance over the pre-ligation values, while black asterisks indicate that between the two animal groups at the same time point. Data were presented as mean±SD. (*: p<0.05, **: p<0.01, and ***: p<0.001).

Interestingly, despite the compromised ability for remodeling, the inverse relationship between the initial resistance and the extent of remodeling still held in the obese mice. The structural and functional remodeling parameters, including the vessel diameter (Fig. 3.12a), blood flow (Fig. 3.12b), and vascular tortuosity (Fig. 3.12c), all showed negative correlations with the initial resistance in both the obese and control mice. Although the slopes of the linear correlation were similar between the two animal groups, the intercepts were different.
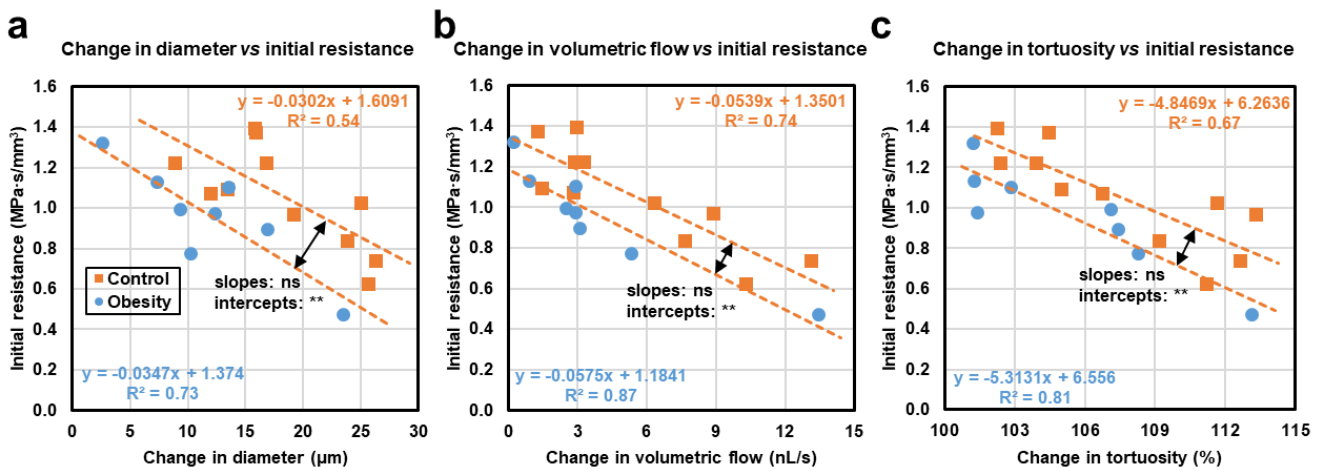
Fig. 3.12. Influence of obesity on the relationship between initial vascular resistance and the extent of collateral remodeling. Inverse correlation between initial resistance and changes in (a) vessel diameter, (b) volumetric blood flow and (c) tortuosity, respectively, in the control and obese mice. Statistical significance between the linear fittings of the two groups is indicated below each panel. (ns: not significant, **: p<0.01).

3.4 Discussion

Longitudinal monitoring of the hemodynamic alterations that occur throughout microvascular networks as a result of arteriogenesis has not been possible to date using existing imaging technologies.

However, this information is important for understanding the mechanisms that govern microvascular remodeling in ischemic disease and the functional consequences of microvascular adaptations in response to ischemia. To address this technical challenge, we have developed a hardware-software integrated platform, which is uniquely capable of comprehensive, quantitative, longitudinal and label-free imaging of arteriogenesis at the single-vessel level across the entire microvascular network at different tissue sites *in vivo* (Fig. 3.2). In terms of the hardware, the multi-parametric PAM enables large-scale, high-resolution and noninvasive imaging of microvascular structure as well as blood perfusion, oxygenation and flow, permitting network-wide monitoring over a prolonged period without the influence of exogenous contrast agents (Fig. 3.3). In terms of the software, the vessel segmentation analysis allows not only extracting the structural and functional parameters within individual microvessels across the entire network (Fig. 3.4), but also quantification of other important parameters including vessel diameter, tortuosity, resistance, wall shear stress, and oxygen supply (Fig. 3.7b–g).

In an established mouse model of arterial ligation, we applied this enabling technology to studying network-wide hemodynamic redistribution and microvascular remodeling. Our results revealed striking differences in the structural and functional remodeling of three parallel collateral vessels (Fig. 3.7). Moreover, we observed that the collateral which demonstrated the greatest remodeling response had the lowest initial resistance; and that the collateral with the highest initial vascular resistance showed the least arteriogenesis. These interesting observations led us to hypothesize that the initial resistance is a factor that dictates the fate of collateral remodeling. We tested this hypothesis in mice across three different strains, all showing negative correlations between the initial resistance and each of the three

major remodeling parameters—diameter, tortuosity and blood flow. Moreover, our analysis revealed an inverse relationship between the initial resistance and the change in wall shear stress, which is known to regulate arteriogenesis (Fig. 3.8)[14].

These new observations aligned with and expanded our current understanding of arteriogenesis. According to our finding (Fig. 3.8b), the collateral arteriole with relatively low initial resistance is more easily able to recruit blood flow and facilitate hemodynamic redistribution in cases of arterial occlusion. The flow upregulation results in a significant increase in the shear stress (Fig. 3.7g). It has been previously shown that increases in shear stress induce the expression of nitric oxide synthase, which, in turn, increases the production and availability of nitric oxide for vasodilation. The effects of this are evident in the relative changes between the pre- and post-ligation time points in Fig. 3.7b[16]. Moreover, the increased shear stress triggers the production of a multitude of inflammatory cytokines and adhesion molecules, which then drive the recruitment of bone marrow-derived cells to the collateral[17-19]. These recruited cells break down the extracellular matrix and stimulate proliferation through paracrine signaling, thereby initiating a switch in mural cells of the vessel wall to a proliferative phenotype. This leads to the beginning of a growth phase, during which the lumenal diameter expands, as seen between days 3 and 21 in Fig. 3.7b[19]. As the remodeling proceeds, hemodynamics across the vascular network gradually shift towards the normal physiological levels (Fig. 3.3 and Fig. 3.4) and the maturation phase begins. During this phase, anti-inflammatory markers increase[18], accumulated bone marrow-derived cells disperse[19,20], and smooth muscle cells return to a contractile phenotype[21]. While larger-diameter remodeling collaterals tend to stabilize, less-developed small collaterals may instead partially regress. Both processes are

reflected in diameter changes of various individual collateral segments between days 10 and 21 in Fig. 3.4a[22]. It is worth noting that we and others have previously demonstrated that ligation of feeding arteries causes diameter expansion of collateral vessels accompanied by smooth muscle cell proliferation in the ear[12], adipose tissue[23], and skeletal muscle[24]. Therefore, here, we chose to use sustained and progressive diameter expansion (over multiple time points spanning weeks) as an indicator of arteriogenesis, with the assumption that this process has been previously shown to be a consequence of vascular smooth muscle cell and endothelial cell proliferation within the collateral vessel wall.

Using this platform, we studied the influence of obesity on microvascular remodeling. Our results showed that obesity significantly impaired the ability of the microvasculature for sustained arteriogenesis and flow upregulation in response to arterial ligation, resulting in much lower blood supply and tissue oxygenation compared to the control mice (Fig. 3.10 and 3.11); and the impaired hemodynamic response of the obese mouse to ischemia was likely due to the compromised remodeling ability. Given the observation that the obesity-induced deficit in arteriogenesis occurred after day 7 post-ligation, we hypothesize that impaired maturation and stabilization of growing collateral vessels may be responsible. However, additional work is required to validate this hypothesis. Interestingly, although the remodeling ability was impaired in the obese mice, the inverse relationship between the initial resistance and the extent of remodeling still held (Fig. 3.12). However, the lower intercepts in the obese group suggested that, even with similar initial resistance, the collaterals in the obese mice tended to remodel less compared to those in the control mice.

While Cui et al.[25] reported elevated blood glucose and decreased serum insulin levels in C57BL/6

mice fed Research Diets D12451, van Weel et al.[26] did not find evidence of insulin resistance having a detrimental effect on arteriogenesis in obese Ob/Ob mice fed a normal diet. Further, Pettersson et al.[27] demonstrated that female C57BL/6 mice were protected, relative to males, from metabolic syndrome following 14 weeks on a similar obesogenic diet. Therefore, it is unclear what contribution, if any, insulin resistance makes to the defect in arteriogenesis observed in the present study. Chen et al.[28] provided evidence that a change occurs in white adipose tissue of mice during high fat diet-induced obesity which disrupts normal cell signaling. This group reported improved arteriogenesis and increased markers of M2 macrophages in the skeletal muscle of high-fat diet-fed mice, which had received transplant of white adipose tissue from lean donors following a ligation surgery. Huang et al.[29] demonstrated that hypercholesterolemia can induce metabolic syndrome in non-obese individuals and causes dysfunction in adipocytes, resulting in increased production of inflammatory cytokines and adipocyte death. This study further demonstrated that high levels of cholesterol reduced macrophage CD206 expression *in vitro*. Pettersson et al.[27] reported highly elevated serum cholesterol levels in metabolic syndrome-protected female C57BL/6 mice fed an obesogenic diet similar to the one used in the present study. Although that study did not find elevated numbers of F4/80+ macrophages in adipose tissue of obese females (unlike in males), macrophage phenotypes of obese versus lean animals were not examined. It has been previously demonstrated that adipose tissue macrophage phenotypes are altered during the progression of obesity[30].

It is important to note that female C57BL/6 mice have been demonstrated to have impaired perfusion recovery in hindlimb compared to males following femoral ligation[31], and sex needs to be considered

when interpreting results of studies of vascular remodeling. Our findings suggest that collateral remodeling in obese female C57BL/6 mice is impaired versus that in lean females most notably after 7 days, when growing collaterals should be maturing and then stabilizing. We have previously shown that many of the macrophages recruited to remodeling collateral arteries in murine models of arteriogenesis are not tissue-resident, but are derived from circulating monocytes which extravasate into the tissue through post-capillary venules[32]. These cells would likely not share the phenotypes of tissue-resident macrophages upon arrival, but disruption of the normally required phenotypic transition over time by aberrant cell signaling induced by obesity and/or hypercholesterolemia is a possible explanation for the observed deficits in arteriogenesis and tissue perfusion.

For potential translation of our findings, it is important to consider the relevance of the ear skin to other tissues that may play more important roles in cardiovascular diseases, such as the adipose and cardiac tissue. It should be noted that the primary function of the vasculature in the murine ear, which is comprised predominantly of skin and cartilage and a very small amount of adipose where the ear connects to the head, is to aid in thermoregulation[33]. This function is enabled by dense microvasculature, which can be described as an arborized network that enters the lobe as paired arterioles and venules that branch into interdigitating capillaries spanning the surface of the ear. Also sometimes present in this tissue are 20-50 μm collateral arterioles that connect arterioles directly to other arterioles. This network anatomy is similar to microvascular beds found in other murine tissues that we have studied, including the adipose and skeletal muscle[23,32]. Despite the similarities in microvascular network architecture between skin, adipose, and muscle, it is likely that these microvascular beds differ at the cellular level. For example,

the profile of selectin expression by endothelial cells is known to be different between skin and muscle, even in response to the same inflammatory stimulus[34]. Therefore, phenotypic heterogeneities in vascular cells across different microvascular beds motivate future studies that should be conducted to confirm the extent to which the microvascular remodeling phenomena observed in the murine ear are also relevant in the cardiac and adipose tissue.

3.5 Conclusion

In summary, we have developed a first-of-a-kind imaging and analysis platform for longitudinal monitoring of hemodynamic redistribution and arteriogenesis across the complex microvascular network *in vivo*. Using this enabling technology, we found a novel inverse correlation between the initial vascular resistance and the extent of collateral remodeling. Interestingly, obesity does not affect this inverse relationship, but impairs arteriogenesis after day 7. This new knowledge could potentially prove useful for targeting individual collaterals of high remodeling potential, should focused local delivery of therapeutic compounds be desired[35].

Reference

[1]   Brunner, F., Tomandl, B., Hanken, K., Hildebrandt, H. & Kastrup, A. Impact of collateral circulation on early outcome and risk of hemorrhagic complications after systemic thrombolysis. *International Journal of Stroke* **9**, 992-998 (2014).

[2]   Kimmel, E. R. *et al.* Absence of Collaterals is Associated with Larger Infarct Volume and Worse Outcome in Patients with Large Vessel Occlusion and Mild Symptoms. *Journal of Stroke and Cerebrovascular Diseases* **28**, 1987-1992 (2019).

[3]   Fulton, W. F. ANASTOMOTIC ENLARGEMENT AND ISCHAEMIC MYOCARDIAL DAMAGE. *Br Heart J* **26**, 1-15 (1964).

[4]   Pipp, F. *et al.* Elevated Fluid Shear Stress Enhances Postocclusive Collateral Artery Growth and Gene Expression in the Pig Hind Limb. *Arteriosclerosis, Thrombosis, and Vascular Biology* **24**, 1664-1668 (2004).

[5]   Rege, A., Thakor, N. V., Rhie, K. & Pathak, A. P. In vivo laser speckle imaging reveals microvascular remodeling and hemodynamic changes during wound healing angiogenesis. *Angiogenesis* **15**, 87-98 (2012).

[6]   Letourneur, A., Chen, V., Waterman, G. & Drew, P. J. A method for longitudinal, transcranial imaging of blood flow and remodeling of the cerebral vasculature in postnatal mice. *Physiological Reports* **2**, e12238 (2014).

[7]   Pierce, M. C., Javier, D. J. & Richards-Kortum, R. Optical contrast agents and imaging systems for detection and diagnosis of cancer. *International Journal of Cancer* **123**, 1979-1990 (2008).

[8]   Sakadžić, S. *et al.* Two-photon high-resolution measurement of partial pressure of oxygen in cerebral vasculature and tissue. *Nature Methods* **7**, 755-759 (2010).

[9]   Wang, L. V. & Hu, S. Photoacoustic Tomography: In Vivo Imaging from Organelles to Organs. *Science* **335**, 1458-1462 (2012).

[10]   Ning, B. *et al.* Simultaneous photoacoustic microscopy of microvascular anatomy, oxygen saturation, and blood flow. *Opt. Lett.* **40**, 910-913 (2015).

[11]   Ning, B. *et al.* Ultrasound-aided Multi-parametric Photoacoustic Microscopy of the Mouse Brain. *Scientific Reports* **5**, 18775 (2015).

[12]   Billaud, M. *et al.* A New Method for In Vivo Visualization of Vessel Remodeling Using a Near-Infrared Dye. *Microcirculation* **18**, 163-171 (2011).

[13]   Heuslein Joshua, L. *et al.* Mechanisms of Amplified Arteriogenesis in Collateral Artery Segments Exposed to Reversed Flow Direction. *Arteriosclerosis, Thrombosis, and Vascular Biology* **35**, 2354-2365 (2015).

[14]   Piiper, J. & Scheid, P. Diffusion limitation of O2 supply to tissue in homogeneous and heterogeneous models. *Respiration Physiology* **85**, 127-136 (1991).

[15]   Nishimura, N., Schaffer, C. B., Friedman, B., Lyden, P. D. & Kleinfeld, D. Penetrating arterioles are a bottleneck in the perfusion of neocortex. *Proc Natl Acad Sci U S A* **104**, 365-370 (2007).

[16]   Davies, P. F. Hemodynamic shear stress and the endothelium in cardiovascular pathophysiology. *Nature Clinical Practice Cardiovascular Medicine* **6**, 16-26 (2009).

[17]   Meisner, J. K. & Price, R. J. Spatial and Temporal Coordination of Bone Marrow-Derived Cell Activity during Arteriogenesis: Regulation of the Endogenous Response and Therapeutic Implications. *Microcirculation* **17**, 583-599 (2010).

[18]   Lee, C. W. *et al.* Temporal patterns of gene expression after acute hindlimb ischemia in mice: insights into the genomic program for collateral vessel development. *Journal of the American College of Cardiology* **43**, 474-482 (2004).

[19]   Scholz, D. *et al.* Ultrastructure and molecular histology of rabbit hind-limb collateral artery growth (arteriogenesis). *Virchows Archiv* **436**, 257-270 (2000).

[20]   Arras, M. *et al.* Monocyte activation in angiogenesis and collateral growth in the rabbit hindlimb. *The Journal of Clinical Investigation* **101**, 40-50 (1998).

[21]   Wolf, C. *et al.* Vascular Remodeling and Altered Protein Expression During Growth of Coronary Collateral Arteries. *Journal of Molecular and Cellular Cardiology* **30**, 2291-2305 (1998).

[22]   Schaper, W. & Scholz, D. Factors Regulating Arteriogenesis. *Arteriosclerosis, Thrombosis, and Vascular Biology* **23**, 1143-1151 (2003).

[23]   Seaman, S. A., Cao, Y., Campbell, C. A. & Peirce, S. M. Macrophage Recruitment and Polarization During Collateral Vessel Remodeling in Murine Adipose Tissue. *Microcirculation* **23**, 75-87 (2016).

[24]   Mac Gabhann, F. & Peirce, S. M. Collateral capillary arterialization following arteriolar ligation in murine skeletal muscle. *Microcirculation* **17**, 333-347 (2010).

[25]   Cui, L., Liu, M., Chang, X. & Sun, K. The inhibiting effect of the Coptis chinensis polysaccharide on the type II diabetic mice. *Biomedicine & Pharmacotherapy* **81**, 111-119 (2016).

[26]   van Weel, V. *et al.* Hypercholesterolemia Reduces Collateral Artery Growth More Dominantly Than Hyperglycemia or Insulin Resistance in Mice. *Arteriosclerosis, Thrombosis, and Vascular Biology* **26**, 1383-1390 (2006).

[27]   Pettersson, U. S., Waldén, T. B., Carlsson, P.-O., Jansson, L. & Phillipson, M. Female Mice are Protected against High-Fat Diet Induced Metabolic Syndrome and Increase the Regulatory T Cell Population in Adipose Tissue. *PLOS ONE* **7**, e46057 (2012).

[28]   Chen, L. *et al.* Transplantation of Normal Adipose Tissue Improves Blood Flow and Reduces Inflammation in High Fat Fed Mice With Hindlimb Ischemia. *Frontiers in Physiology* **9** (2018).

[29]   Jiung-Pang, H. *et al.* Role of dysfunctional adipocytes in cholesterol-induced nonobese metabolic syndrome. *Journal of Molecular Endocrinology* **60**, 309-323 (2018).

[30]   Shaul, M. E., Bennett, G., Strissel, K. J., Greenberg, A. S. & Obin, M. S. Dynamic, M2-Like Remodeling Phenotypes of CD11c+ Adipose Tissue Macrophages During High-Fat Diet–Induced Obesity in Mice. *Diabetes* **59**, 1171-1181 (2010).

[31]   Peng, X. *et al.* Gender differences affect blood flow recovery in a mouse model of hindlimb ischemia. *American Journal of Physiology-Heart and Circulatory Physiology* **300**, H2027-H2034 (2011).

[32]   Bruce Anthony, C. *et al.* Monocytes Are Recruited From Venules During Arteriogenesis in the Murine Spinotrapezius Ligation Model. *Arteriosclerosis, Thrombosis, and Vascular Biology* **34**, 2012-2022 (2014).

[33]   Al-Hilli, F. & Wright, E. A. The effects of environmental temperature on the body temperature

and ear morphology of the mouse. *Journal of Thermal Biology* **13**, 197-199 (1988).

[34]   Hickey, M. J. *et al.* Varying roles of E-selectin and P-selectin in different microvascular beds in response to antigen. *Journal of immunology (Baltimore, Md. : 1950)* **162**, 1137-1143 (1999).

[35]   Patel, S. R., Bellary, S., Karimzad, S. & Gherghel, D. Overweight status is associated with extensive signs of microvascular dysfunction and cardiovascular risk. *Scientific Reports* **6**, 32282 (2016).

Chapter 4 Modified VEGF-A mRNA induces sustained multifaceted microvascular response and accelerates diabetic wound healing

4.1 Introduction

Tissue ischemia due to the lack of proper vascularization is a major complication that underlies a wide variety of devastating diseases, including coronary artery disease, heart failure, critical limb ischemia, and chronic diabetic ulcers with impaired wound healing ability[1-4]. These areas with large unmet medical needs would greatly benefit from novel and effective pharmacological treatments. Targeting the stimulation of angiogenesis, arteriogenesis, and lymphangiogenesis, therapeutic vascular growth has been put forward as a promising strategy for management of such indications[5,6]. Administered in the form of recombinant protein or via naked or adenoviral vector-mediated gene transfer, the vascular endothelial growth factor A (VEGF-A; especially its primary isoform with 165 amino acids, VEGF-A165) has shown potential beneficial effects in cardiovascular diseases and wound healing and has received increasing attention[6,7]. However, randomized controlled trials have not lived up to expectations and the clinical efficacy remains inconclusive[8,9]. Although the overall reason(s) for the underwhelming clinical benefit is unclear, possible limiting factors of current VEGF-A therapies include suboptimal pharmacokinetics and insufficient local concentration of the protein, poor gene transfer efficiency, inappropriate timing of dosing, regression of immature vessels, and growth factor-related adverse effects, such as edema and systemic hypotension[5].

To circumvent these issues associated with recombinant protein and gene transfer-based therapies, chemically modified mRNA has been developed as a novel non-immunogenic and non-integrating

modality for efficient and transient expression of target proteins in selected tissues *in vivo*[10,11]. Encoding VEGF-A165, AZD8601 is a new, purified and clinical-grade modified mRNA optimized to ensure efficient transfection and protein production with minimal innate immune response[12,13]. Recently, it was demonstrated in the subacute setting of porcine myocardial infarction that intracardiac injection of AZD8601 formulated in a biocompatible citrate/saline vehicle resulted in improved left ventricular function, increased neovessel formation, and attenuated cardiac fibrosis 2 months after injection[12,13]. Moreover, AZD8601 has been brought into clinical testing in patients with type-2 diabetes mellitus and in patients undergoing open heart surgery, with the primary objective to assess the safety and tolerability of this new therapeutic (ClinicalTrials.gov Identifiers: NCT02935712 and NCT03370887). Although promising, the functional pharmacodynamic effects and the potential therapeutic benefits of this emerging therapeutic on the microvasculature needs further characterization *in vivo*.

In this chapter, we quantitatively characterize the dynamic changes in the microvascular structure and function following single or repeated intradermal injections of AZD8601 in the live mouse ear. With the aid of label-free, noninvasive multi-parametric PAM)[14,15], we demonstrate the pronounced, sustained and dose-dependent effects of AZD8601 on the microvasculature through side-by-side comparison against recombinant human VEGF-A protein, a non-translatable variant of AZD8601 (NT-VEGF-A mRNA), and citrate/saline vehicle. Furthermore, we dynamically evaluate the bioactivity of AZD8601 in an established mouse model of diabetic wound healing *in vivo*. Capitalizing on a boron nanoparticle-based tissue oxygen sensor[16], we demonstrate the dose- and time-dependent effects of AZD8601 on the re-vascularization and re-oxygenation of the wound bed, which leads to accelerated re-epithelialization

during the early phase of diabetic wound healing.

4.2 Methods

4.2.1 Study design

The central goal of this study was to comprehensively characterize the microvascular response to AZD8601 and evaluate its bioactivity in diabetic wound healing *in vivo*. To this end, we employed two state-of-the-art technologies: multi-parametric PAM and boron nanoparticle-based tissue oxygen sensing. First, we quantified the acute (30 minutes to 6 hours post-injection) and chronic (up to 28 days) responses of the microvascular structure and function, as well as the associated oxygen extraction and metabolism, to AZD8601 intradermally injected in the mouse ear. Then, we compared the multifaceted response to AZD8601 with those to VEGF-A protein, NT-VEGF-A mRNA, and citrate/saline vehicle (n = 8/group). In parallel, we studied the dose dependence of the microvascular response on AZD8601. The PAM-based *in vivo* characterization was compared with the transfection efficiency, pharmacokinetics and hybridization of AZD8601 characterized by biochemical assays. Following the characterization, we evaluated the bioactivity of AZD8601 in a mouse model of diabetic wound healing in three separate trials. Trial 1 (n = 7–8/group) was designed to address the influence of single (i.e., dosing on day 0 only) or double (dosing on day 0 and day 3, respectively) dosing. Trial 2 (n = 3–4/group) combined the boron nanoparticle-based tissue oxygen sensor and standard wound healing analysis protocol to examine the effects of AZD8601 on the re-oxygenation of the wound bed and the healing rate. Trial 3 (n = 6/group) was designed as a dose-response study (30, 100 and 200 μg AZD8601), including a positive control (recombinant VEGF-A165 protein).

4.2.2 Transfection efficiency in human aortic smooth muscle cells *in vitro*

The transfection potential of both AZD8601 and NT-VEGF-A mRNA (Moderna Therapeutics) were assessed in human aortic smooth muscle cells. Ten thousand cells were seeded into 96-well plates in smooth muscle growth medium (SmGM-2; Lonza). In the following day, transfection was undertaken in the serum-free medium. Following the manufacturer's instruction, 250 ng of AZD8601 or NT-VEGF-A mRNA (Moderna Therapeutics) was mixed with Lipofectamine 2000 and then added to the cells. After 4 hours, the transfection medium was removed and changed to fresh serum-free media that was collected after 24 hours and kept at $-80\,°C$. The experiment was repeated three times. The amount of VEGF-A protein in the supernatant post transfection was measured using a human VEGF-A ELISA kit (Novex, Invitrogen). The absorbance was measured at 450 nm using a SpectraMax reader (Molecular Devices).

4.2.3 *In situ* hybridization for AZD8601 and immunohistochemistry for VEGF-A protein in skin

At predefined time points after intradermal injection of AZD8601 on the back of male db/db mice, skin biopsies with an area of $0.785\ mm^2$ was taken from the back of male db/db mice using a 10-mm biopsy punch. The biopsy was put in 4% formaldehyde for immersion fixation and cut in three slices. Subsequently, the pieces were embedded in paraffin and further sectioned into 4-µm slices. RNAscope-automated *in situ* hybridization assay for detection of AZD8601 was carried out in the Bond RX platform (Leica Biosystems) and all *in situ* hybridization reagents were products of the Advanced Cell Diagnostics. Briefly, target retrieval was performed at $95\,°C$ for 15 minutes using Leica Epitope Retrieval Buffer 2 followed by protease treatment at $42\,°C$ for 15 minutes. The probe (RNAscope LS2.5 Probe-Hs-VEGFA-noXrodent cat. nr 412018; Advanced Cell Diagnostics) were hybridized for 2 hours at $42\,°C$ followed by

RNAscope amplification, and 3,3′-diaminobenzidine was used to visualize staining. Immunohistochemistry for detection of VEGF-A protein was carried out in the Ventana discovery Ultra immunostainer, and all reagents were Ventana products (Roche). Antigen retrieval was done in Ventana Cell Conditioner 1 for 24 minutes at 95 °C. VEGF-A primary antibody was added for 1 hour at 37 °C (dilution 1:100, Cat. # RB-9031-P0; Thermo Fisher Scientific), followed by secondary anti-rabbit HQ reagent and anti-HQ HRP Purple chromogenic detection.

4.2.4 Quantification of VEGF-A protein in mouse skin

At predefined time points after intradermal injection of AZD8601 on the back of male db/db mice, tissue biopsies from the injection site on the back or the entire ear was sampled and snap frozen in liquid nitrogen and stored at −80 °C until processed. Tris lysis buffer containing phosphatase inhibitors I and II and protease inhibitor (R60TX; Meso Scale Diagnostics) was added to the frozen tissue biopsies and kept at −20 °C prior to homogenization. Stainless steel beads (2.8 mm) were then added, and the samples were homogenized using the Precellys homogenizer. The homogenates were centrifuged, and the supernatants were stored at −80 °C pending analysis. Concentrations of VEGF-A165 were determined using a sandwich immunoassay with electrochemical luminescent detection. V-PLEX Human VEGF assay kit (K151RHD, Meso Scale Diagnostics) was used to measure the VEGF-A165 concentration in the tissue homogenates. Standards were serially diluted in MSD diluents. Samples with high concentration were diluted with MSD diluents prior to analysis to fit within the standard curve, and the plates were read on the MSD's Sector Imager 6000.

4.2.5 Multi-parametric PAM of the mouse ear microvasculature

Six-week-old C57BL/6BrdCrHsd-Tyrc mice (Envigo) were used for this study. Multi-parametric PAM of the microvascular response in the mouse ear is completely label-free and noninvasive. Thus, the same ear was repeatedly imaged for time-lapse monitoring of drug effects (100 µg AZD8601, 100 µg NT-VEGF-A mRNA, 1 µg recombinant VEGF-A165 protein (R&D Systems), and 10 µL citrate/saline vehicle) on the microvascular diameter, sO_2, blood flow, angiogenesis and neovascularization over a prolonged period of 28 days.

Prior to intradermal injection of the drugs, a set of baseline images of the mouse ear were acquired using multi-parametric PAM. Then, the drug-treated ear was repeatedly imaged for 6 hours to capture acute microvascular responses and reimaged on a weekly basis to record chronic responses and possible angiogenesis and/or neovascularization. In cases of multiple injections, the drugs were injected at the same location in the ear on day 0, 2 and 4.

To avoid motion artifacts, PAM of the mouse ear was conducted under general anesthesia, which was inducted with 2% isoflurane vaporized by medical-grade air (Praxair) at a flow rate of 1–1.5 L/min. After the induction of anesthesia, the mouse was transferred to a nearby stereotaxic stage in the PAM system, and a thin layer of ultrasonic gel (Parker) was gently applied to the ear surface for ultrasound coupling. Care was taken to avoid trapping air bubbles inside the gel. Then, the ear was placed beneath a container filled with temperature-controlled deionized water (37 °C) and slowly raised until the gel was in gentle contact with the bottom of the container, which was covered by a thin membrane of polyethylene (S. C. Johnson & Son). The imaging head of the PAM was then lowered and immersed in the water

container. Air bubbles trapped under the imaging head were removed. Throughout the PAM experiment, the mouse was maintained under general anesthesia with 1.5% isoflurane and its body temperature was kept at 37 °C using a heating pad (SRFG-303/10; Omega) and a temperature controller (EW-89802-52; Cole-Parmer). Ointment was applied to the mouse eyes to prevent drying and accidental laser damage. The laser fluence was carefully controlled to comply with the safety standards of the American National Standards Institute (i.e., 20 mJ/cm^2). At the conclusion of the experiment, the mouse ear was cleaned with deionized water before being transported back to its home cage.

Three microvascular parameters (i.e., structure, sO$_2$ and blood flow) were simultaneously acquired by multi-parametric PAM, and further extracted using our self-developed vessel segmentation algorithm demonstrated in Chapter 2, with which volumetric blood flow, OEF and oxygen metabolism can be derived. Eight mice were studied per group, and the measurements of different animals within each group were combined for statistical analysis.

4.2.6 Assessment of diabetic wound healing

Eight-week-old B6.BKS(D)-Leprdb/J mice (Jackson Laboratory) were used for the wound healing study. Prior to wounding, mice were fasted for 4 hours on wood chip bedding with access to water. Initial fasted glucose measurements were taken on blood drawn from tail veins. At the terminal endpoint of the study and prior to tissue harvest, mice were anesthetized via inhalation of 2% isoflurane/98% oxygen mixture and fed glucose measurements were taken from blood obtained via cardiac puncture.

Mice were anesthetized by inhalation of 2% isoflurane/98% oxygen mixture. Dorsa were shaved and depilated before being sterilized with three alternating scrubs of povidone-iodine and 70%

isopropanol. Full-thickness cutaneous wounds, which were 1 cm in diameter, were surgically made on the dorsum of each mouse. An analgesic (buprenorphine, 0.1 mg/kg) was administered following the surgery and the wounds were covered with a Tegaderm dressing. Mice were singly housed with food and water available ad libitum.

Ten μL of AZD8601 (0.75, 2.5, or 5 mg/mL in 10 mmol/L citrate/130 mmol/L saline) or citrate/saline vehicle (10 mmol/L/130 mmol/L) were injected intradermally at four equidistant points around the wound edge. Study groups indicated as "single-injected" received injections on day 0 only. Study groups indicated as "double-injected" received injections on day 0 and 3. The injections were placed at the 0, 90, 180, and 270 degree positions on day 0. Injections administered on day 3 were placed at the 45, 135, 225, and 315 degree positions. Seventy-two μL of recombinant VEGF-A protein (1 μg/μL in 0.9% saline with 0.1% bovine serum albumin; R&D Systems) was administered topically to the wounds of one treatment group. This group received VEGF-A delivery at 0, 2, 4, 6, and 8 days post-surgery.

For bright-field imaging, Tegaderm dressings were removed when mice were anesthetized. Wounds were illuminated with a Dolan-Jenner MI 150 fiber optic illuminator (Edmund Optics) and photographed with an iPhone 6 (Apple) mounted to a clamp and affixed to a ring stand. Wounds were imaged on days 0, 3, 6, 10, 13 (all trials), and 18 (trials 1 and 2 only).

For oxygen-sensing nanoparticle imaging, a Grasshopper3 camera (GS-U3-41C6C; FLIR) was mounted to a microscope (Eclipse 80i; Nikon) equipped with a 4X objective, a fluorescence light source (X-Cite 120Q; Excelitas Technologies), a bandpass excitation filter (360/20 nm), and a long pass barrier

filter (>425 nm). Images were acquired with Flycapture2 software (FLIR). Mice were anesthetized via inhalation of 2% isoflurane and Tegaderm bandages were removed. The body temperature of the mouse was maintained throughout imaging, and wounds were irrigated with sterile 0.9% saline solution when necessary to prevent drying. Fifty μL of BF2nbm(I)PLA (Difluoroboron β-diketonate poly(lactic acid))[16] nanoparticle solution was added to the wound (when necessary, a piece of sterile gauze was used to wick saline solution from the wound immediately prior to addition of the nanoparticle solution), and fluorescent and phosphorescent signals were recorded. Nanoparticle imaging was performed prior to addition of treatments, and nanoparticle solution was flushed from the wound with sterile 0.9% saline following imaging.

The UV-illuminated wound images were analyzed using a self-developed MATLAB program. Background signals in the blue and red channels were calculated from wound images taken prior to the addition of nanoparticle solution. These background values were subtracted from red and blue intensity values acquired after the addition of the nanoparticles. The ratio of blue channel intensity to red channel intensity was computed for each pixel to represent the ratio of fluorescence (constant in the presence of BF2nbm(I)PLA) to phosphorescence (quenched in the presence of oxygen). To map the relative amount of oxygen within the wound bed, we used the ratio of the background-subtracted blue to red channel intensity values to construct a grayscale image (low oxygen: black; high oxygen: white). We selected the wound bed as the region of interest and quantified the mean gray pixel value using ImageJ (National Institutes of Health).

Mice were euthanized under general anesthesia by exsanguination via cardiac puncture followed by

CO_2 asphyxiation. Approximately 1-mL blood was collected from each mouse into a BD Microtainer MAP (Becton Dickinson) and spun at $1,000 \times g$ for 10 minutes at $4\,°C$. Plasma was isolated after centrifugation and stored in low-protein-retention micro centrifuge tubes. A $1.5 \times 1.5\,cm^2$ area of skin around the wound center was excised and snap frozen in liquid nitrogen for analysis.

4.2.7 Statistics and study approval

To quantitatively compare the differences between the multifaceted microvascular responses to AZD8601, NT-VEGF-A mRNA, VEGF-A protein, and citrate/saline vehicle as shown in Fig. 4.3b, Fig. 4.6, Fig. 4.9, and Fig. 4.10b, a two-way ANOVA analysis was used. For multiple comparison, Tukey correction was used to control the Type I error rate differences. In all studies, mice were randomly assigned to AZD8601, NT-VEGF-A mRNA, VEGF-A protein, and citrate/saline groups. The number of mice in each group were chosen by power analysis and previous experience.

All experimental protocols were approved by Animal Care and Use Committee at the University of Virginia, US, and the local ethics committee on animal experiments in Gothenburg (district of Vastra Gotaland and Varmland). All animal procedures performed in this study were in accordance with Animal Care and Use Committee at the University of Virginia, US, and the local ethics committee on animal experiments in Gothenburg (district of Vastra Gotaland and Varmland) and in accordance with the animal welfare policy of Astra Zeneca.

4.3 Results

4.3.1 Transfection efficiency, pharmacokinetic characterization, and hybridization of AZD8601

As shown in Fig. 4.1a, AZD8601 could be effectively transfected into human smooth muscle cells

and led to the production of VEGF-A protein that was secreted into the supernatant. In contrast, transfection with NT-VEGF-A mRNA did not give rise to VEGF-A production.

Intradermal injection of AZD8601 formulated in citrate/saline to db/db mice (n = 6/dose group) showed that increased dosing of AZD8601 in the range of 10–100 μg led to increased maximum concentration (Cmax) of VEGF-A protein (Fig. 4.1b, left). However, increasing the dose of AZD8601 to 300 μg did not result in further increase in Cmax, suggesting saturation of VEGF-A production. Besides the dose dependence in protein production, we also evaluated the pharmacokinetics in the same *in vivo* setting. Our result showed that the concentration of VEGF-A protein in the db/db mouse skin (3–8 animals/time point assessed) reached a maximum of 36 pg/mg tissue at 6 hours after intradermal injection of AZD8601 (Fig. 4.1b, right). The total exposure (i.e., the area under the curve) of human VEGF-A protein over the entire 144-hour period was 1065 pg/mg tissue.

In situ hybridization and immunohistochemistry analysis of skin biopsies from db/db mice receiving 100 μg AZD8601 suggested that the mRNA and the produced VEGF-A protein could be found up to 144 hours post injection (Fig. 4.1c). The *in situ* hybridization analysis also showed that the cell types transfected in the mouse skin were mainly adipocytes and endothelial cells, with inflammatory, muscle and nerve cells transfected to a lesser extent (Fig. 4.1c). According to the immunohistochemistry analysis results, the most pronounced VEGF-A protein production was found in adipocytes followed by endothelial cells.

Fig. 4.1. Transfection efficiency, pharmacokinetic characterization, and hybridization of AZD8601. (a) subsequent measurement of human VEGF-A protein. Levels of VEGF-A protein produced are normalized to levels produced by AZD8601 (n = 3/group). (b) Maximum concentration of VEGF-A protein (Cmax) after intradermal injection in db/db mice of 10, 100 and 300 μg of AZD8601 in citrate/saline (n = 6/dose group, left panel). Human VEGF-A protein content in skin biopsies up to 144 hours after intradermal injection of 100 μg citrate/saline-formulated AZD8601 in db/db mice (n = 3–8/time point, right panel). (c) In situ hybridization staining for AZD8601 (brown color in the upper panel) and immunohistochemistry staining for human VEGF-A protein (magenta color and black arrows in the lower panel) after intradermal injection of 100 μg AZD8601 in citrate/saline formulation as a function of time up to 144 hours. Magnification is 400x.

4.3.2 Multifaceted microvascular response to AZD8601 *in vivo*

Following the biochemical characterization of AZD8601, we applied serial multi-parametric PAM to study the acute and chronic microvascular responses to AZD8601 in the mouse ear *in vivo*. Fig. 4.2a and Fig. 4.3 show representative time-lapse images of the microvascular structure, blood oxygenation (sO_2), and blood flow in the ear intradermally injected with AZD8601, VEGF-A protein, NT-VEGF-A mRNA or citrate/saline vehicle.

With the aid of vessel segmentation[17], we extracted these measurements on a single-vessel basis, from which we were able to quantitatively compare the microvascular responses to the four different compounds. As shown in Fig. 4.2b, significant increases in the vessel diameter and blood flow were observed shortly (30 minutes to 6 hours) after intradermal injection of AZD8601 or VEGF-A protein. In contrast, much weaker vasodilation and flow increase were observed in mice injected with NT-VEGF-A mRNA or citrate/saline, which was likely due to the needle invasion rather than the compound effect per se. The acute hemodynamic responses gradually regressed back to the baseline levels in the protein-injected group, but remained elevated throughout the entire 28-day monitoring period in the AZD8601 group. Interestingly, the dynamic changes in blood flow were tightly coupled with those in the OEF in the three groups injected with VEGF-A protein, NT-VEGF-A mRNA or citrate/saline, resulting in a roughly constant metabolic rate of oxygen (estimated as $Blood\ flow\ \times\ OEF$). In contrast, the oxygen metabolism of the AZD8601 group gradually increased over the 28-day time course, suggesting possible tissue proliferation due to the improved vascularization.
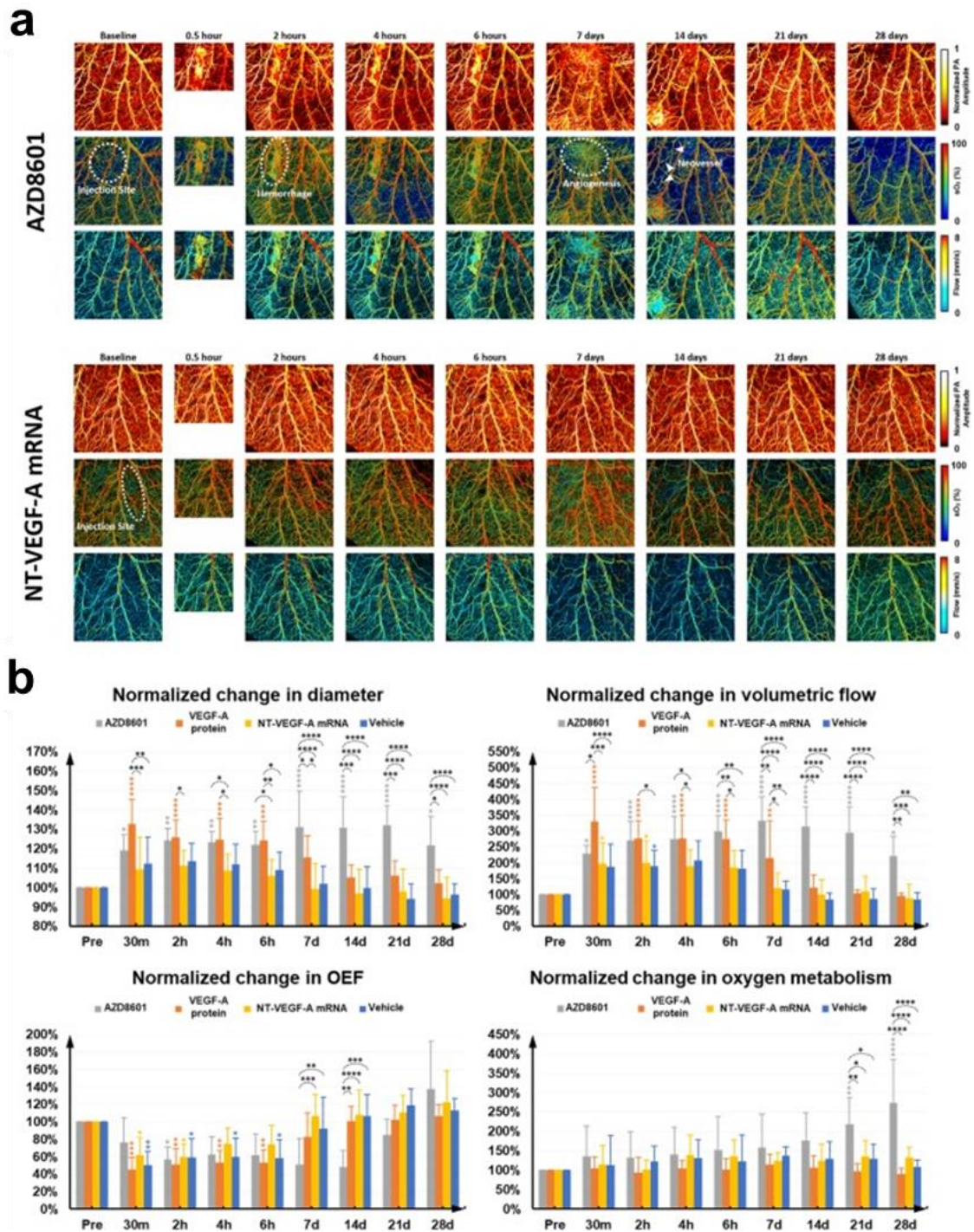
Fig. 4.2. (a) Time-lapse multi-parametric PAM of microvascular responses to 100 μg of AZD8601 or NT-VEGF-A mRNA intradermally injected to the mouse ear. (b) Statistical comparison of the multifaceted microvascular responses to AZD8601, VEGF-A protein, NT-VEGF-A mRNA, and citrate/saline vehicle (n = 8/group). *p < 0.05, **p < 0.01, ***p < 0.001, and ****p < 0.0001.
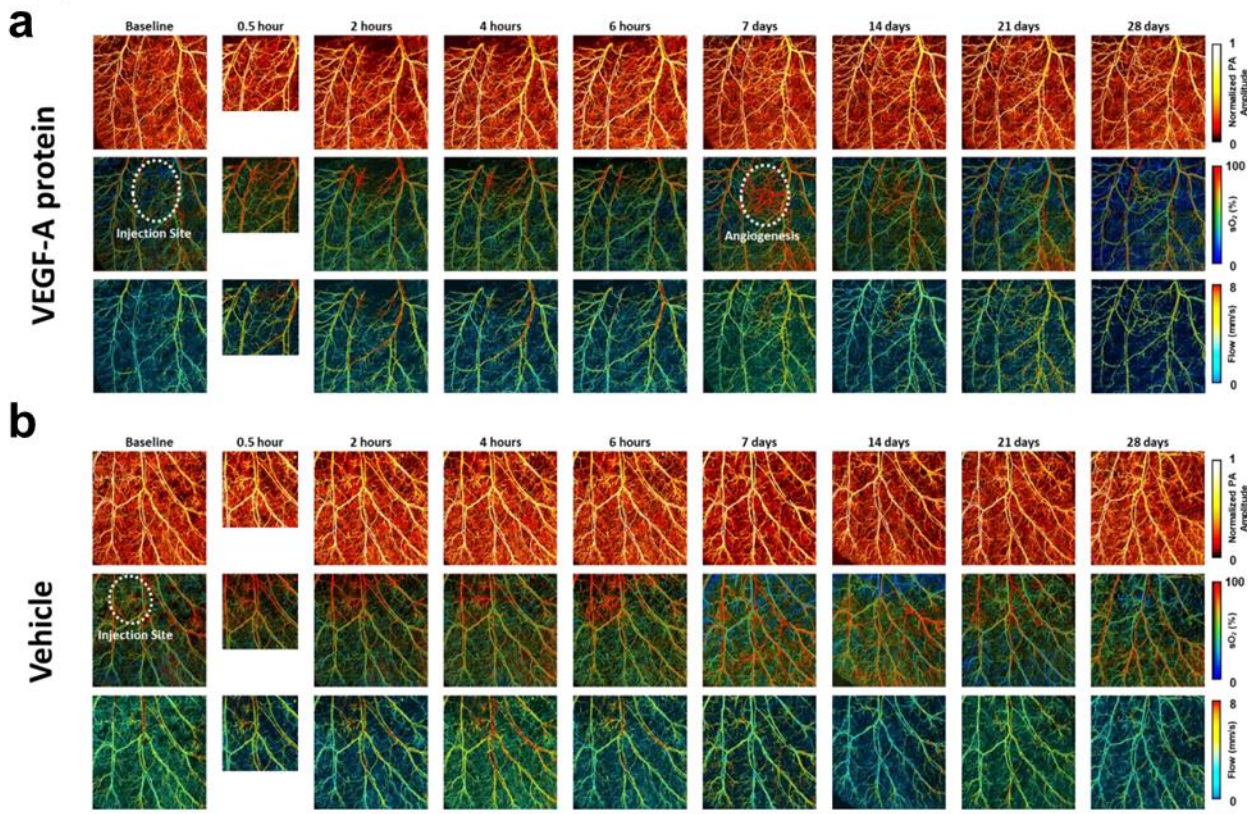
Fig. 4.3. Time-lapse multi-parametric photoacoustic microscopy of microvascular responses to (a) recombinant human VEGF-A protein or (b) citrate/saline vehicle intradermally injected to the mouse ear.

Besides the pronounced hemodynamic responses, striking angiogenesis and neovessel formation were also observed in some of the mouse ears injected with 100 µg AZD8601. As shown in the blowups of the blue boxed region (Fig. 4.4, bottom row), densely packed new capillaries and two branches of neovessels (indicated by green arrows) appeared 7 and 14 days after the injection of AZD8601, respectively. The high brightness of these neovessels in the PAM images implies that they were highly perfused with red blood cells. Interestingly, the neovessels 'regressed' on day 21 and disappeared on day

28. The 'regression' and disappearance of these vessels was likely due to the loss of blood perfusion (the PAM signal comes from blood hemoglobin). In contrast, only moderate capillary angiogenesis but no neovascularization was observed in the VEGF-A protein group (Fig. 4.3). Also, no angiogenesis or neovascularization was observed in the NT-VEGF-A mRNA and citrate/saline groups (Fig. 4.3).
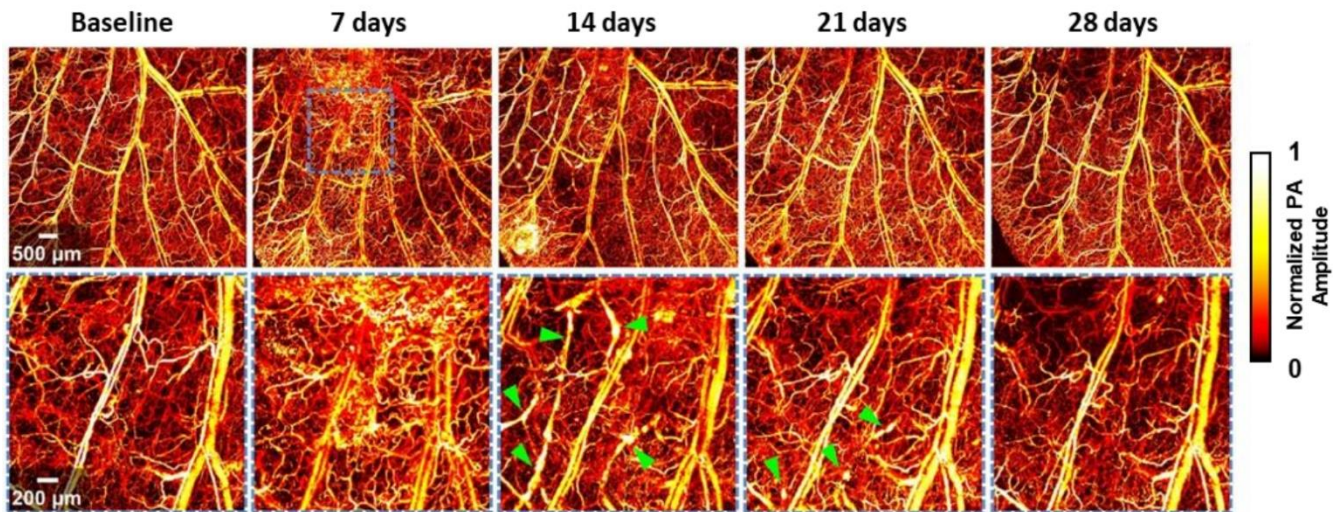
Fig. 4.4. Intradermal injection of 100 μg AZD8601 induces angiogenesis and neovascularization. Top row, microvascular structure of the whole field of view. Bottom row, zoom-in of the blue boxed region showing detailed view of the capillary angiogenesis on day 7 and neovessel formation on day 14 (green arrows).

4.3.3 Effects of sequential dosing of AZD8601 on the microvascular response

To examine whether and how sequential dosing of AZD8601 could affect the microvascular response compared with single dosing, we repeated the time-lapse multi-parametric PAM monitoring experiment in mouse ears sequentially injected with 100 μg AZD8601 at the same location on day 0, 2 and 4 (Fig. 4.5a). Given the similar microvascular responses to NT-VEGF-A mRNA and citrate/saline (Fig. 4.2b), citrate/saline was used as the control in this study (Fig. 4.5b).
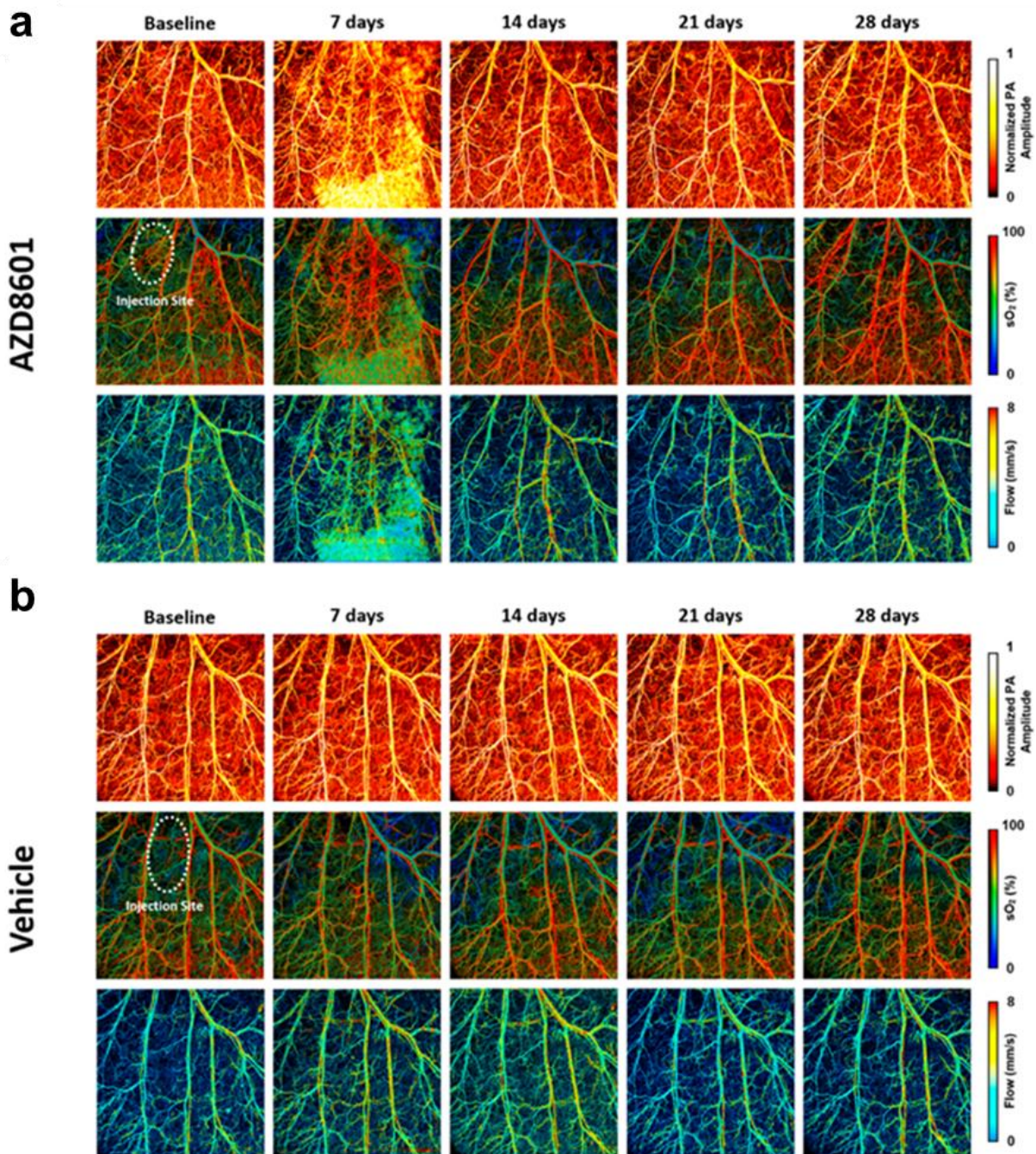
Fig. 4.5. Time-lapse multi-parametric PAM of microvascular responses to sequential dosing of (A) 100 µg AZD8601 or (B) saline vehicle intradermally injected to the mouse ear on day 0, 2 and 4.

As shown in Fig. 4.6, sequential dosing of AZD8601 resulted in larger increases in the vessel diameter (p = 0.0034 on day 7), OEF (p = 0.0003 on day 14), and oxygen metabolism (p = 0.0038 on day 14), compared with the single-dosing group. The differential responses, however, leveled out after 21 days.
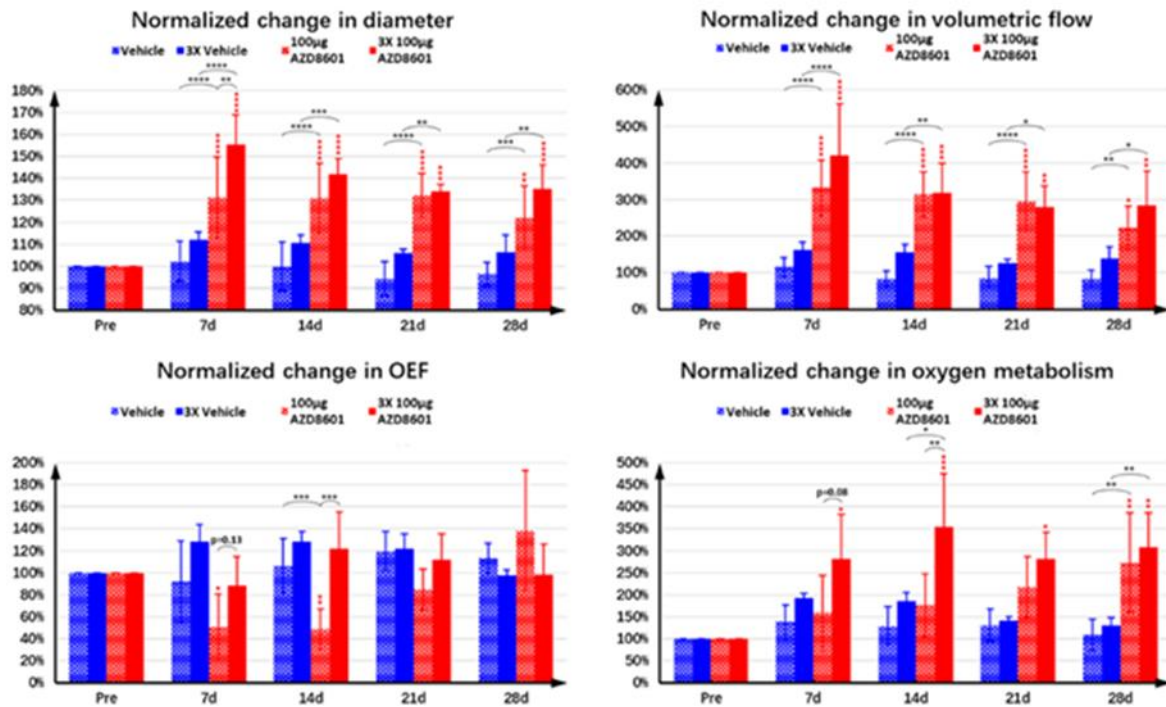
Fig. 4.6. Statistical comparison of the multifaceted microvascular responses in diameter, volumetric flow, oxygen extraction fraction (OEF), and oxygen metabolism to single and multiple injections of AZD8601 and citrate/saline vehicle (n = 4/group). *p < 0.05, **p < 0.01, ***p < 0.001, and ****p < 0.0001.

4.3.4 Dose-dependent effects of AZD8601 on the microvascular response

In light of the dose-dependent protein production (Fig. 4.1b, left), we also investigated the dose dependence of the multifaceted microvascular response on AZD8601. Given the saturation effect beyond

100 µg, two lower doses of AZD8601 (30 and 10 µg) were studied. In mice injected with 30 µg AZD8601, a less sustained increase in sO_2 and blood flow was observed, which regressed back to the baseline on day 14. Although capable of producing capillary angiogenesis around the injection site, neovessel formation was not observed (Fig. 4.7). Reducing the AZD8601 dosage to 10 µg led to further compromised microvascular responses. Specifically, the increase in sO_2 and blood flow was less significant and enduring (regressed to the baseline on day 7) and no angiogenesis or neovascularization was observed (Fig. 4.8).
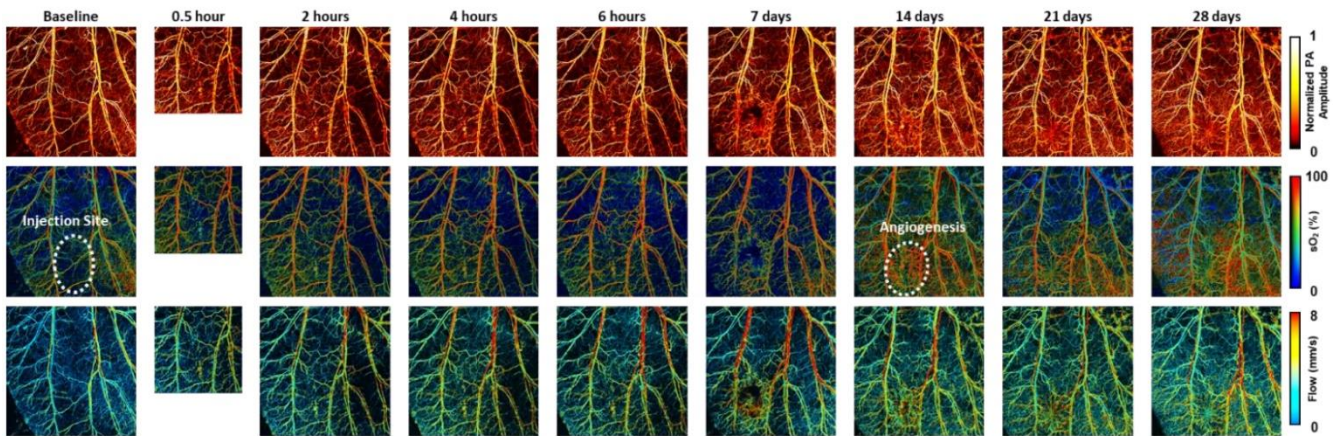
Fig. 4.7. Time-lapse multi-parametric PAM of microvascular responses to 30 µg of AZD8601 intradermally injected to the mouse ear.
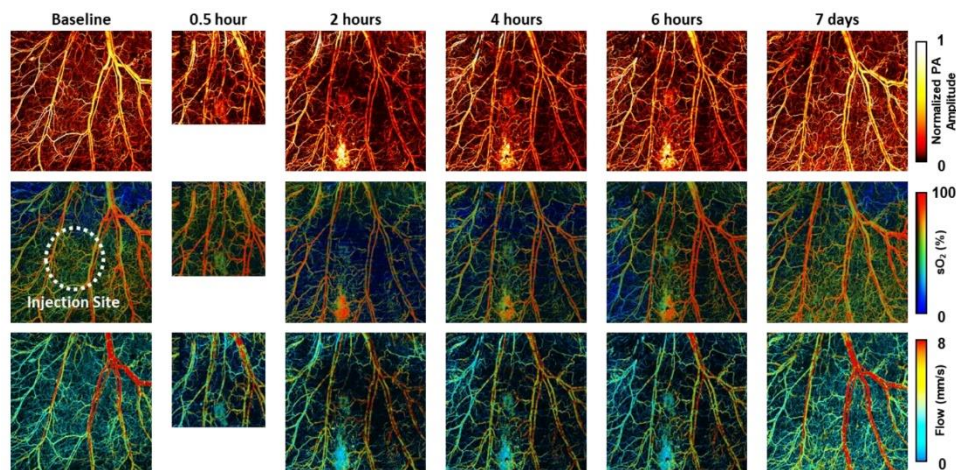
Fig. 4.8. Time-lapse multi-parametric PAM of microvascular responses to 10 µg of AZD8601 intradermally injected to the mouse ear.

4.3.5 Effects of sequential dosing of AZD8601 on the wound healing rate

Following the comprehensive characterization of the microvascular response to AZD8601, we studied the bioactivity and sequential dosing effect of AZD8601 in a mouse model of diabetic wound healing. As shown in Fig. 4.9a, a second dose of AZD8601 delivered on day 3 post-surgery (i.e., wounding) significantly increased early healing versus a single dose on day 0. Increased wound closure was observed in the double-injected AZD8601 group on days 6 and 10 post-surgery. On day 6, the double-injected AZD8601 group exhibited significantly smaller sizes of open wound ($54 \pm 3.9\%$ of original area), compared with single-injected vehicle control ($77 \pm 5.4\%$) and double-injected vehicle control ($71 \pm 7.6\%$). On day 10, the double-injected AZD8601 group exhibited significantly smaller open-wound sizes ($26 \pm 3.3\%$) versus double-injected vehicle control ($48 \pm 7.3\%$).
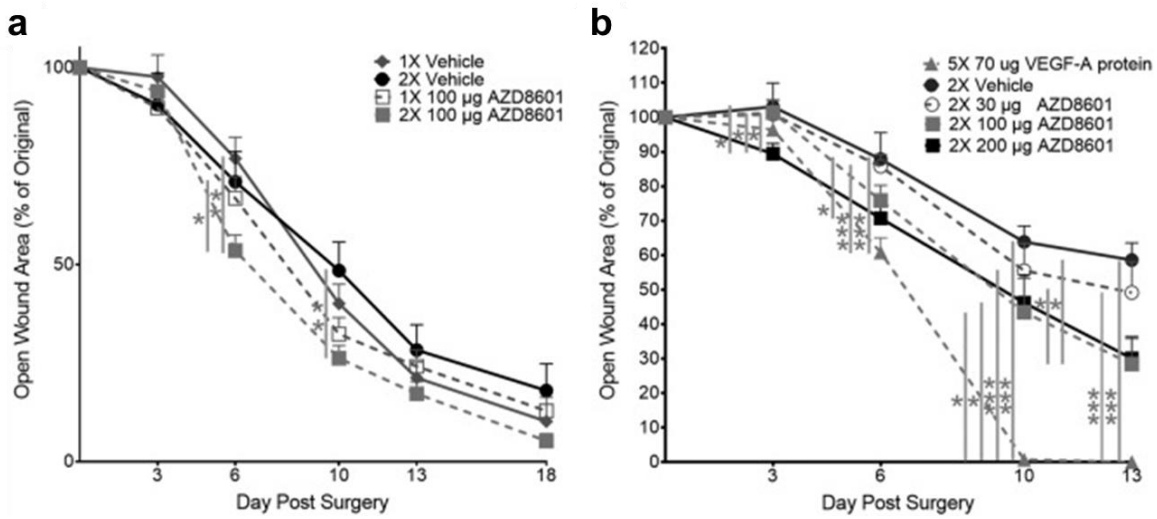
Fig. 4.9. Repeated and higher doses of AZD8601 had greater effects on diabetic wound healing. (a) Dosing on days 0 and 3 increased early healing compared to dosing on day 0 only (n = 7–8/group). (b) The greatest effect on wound closure was achieved by the 200 µg dose of AZD8601 (n = 6/group). *p < 0.05, **p < 0.01, ***p < 0.001.

4.3.6 Dose-dependent effects of AZD8601 on the wound healing rate

Consistent with the dose-dependent microvascular response to AZD8601, higher doses of AZD8601 accelerated early wound healing (Fig. 4.9b). On day 3 post-surgery, the group treated with 200 µg AZD8601 exhibited significantly smaller open-wound sizes (89 ± 3.0%) versus the vehicle control (103 ± 6.9%). On day 6, both the 200 µg AZD8601 group (71 ± 3.6%) and the VEGF-A group (61 ± 4.2%) exhibited significantly smaller open-wound sizes versus the vehicle control (88 ± 7.7%). Likewise, on day 10, the 100 µg AZD8601 group (43 ± 9.8%), the 200 µg AZD8601 group (46 ± 8.2%), and the VEGF-A group (0.7 ± 0.3%) exhibited significantly smaller open wounds versus the vehicle control (64 ± 4.6%). On day 13, the 100 µg AZD8601 group (28 ± 7.4%), the 200 µg AZD8601 group (30 ± 6.3%), and the

VEGF-A group (0 ± 0.0%) all exhibited significantly increased wound closure versus the vehicle control (59 ± 5.0%).

4.3.7 Wound oxygenation monitoring with boron nanoparticle-based tissue oxygen sensor

Besides the wound healing rate, we also evaluated the tissue oxygenation of the wound bed using the boron nanoparticle-based tissue oxygen sensor[16] (Fig. 4.10a). As shown in Fig. 4.10b, the tissue oxygenation level of the wound bed, estimated by the mean gray value of the black and white
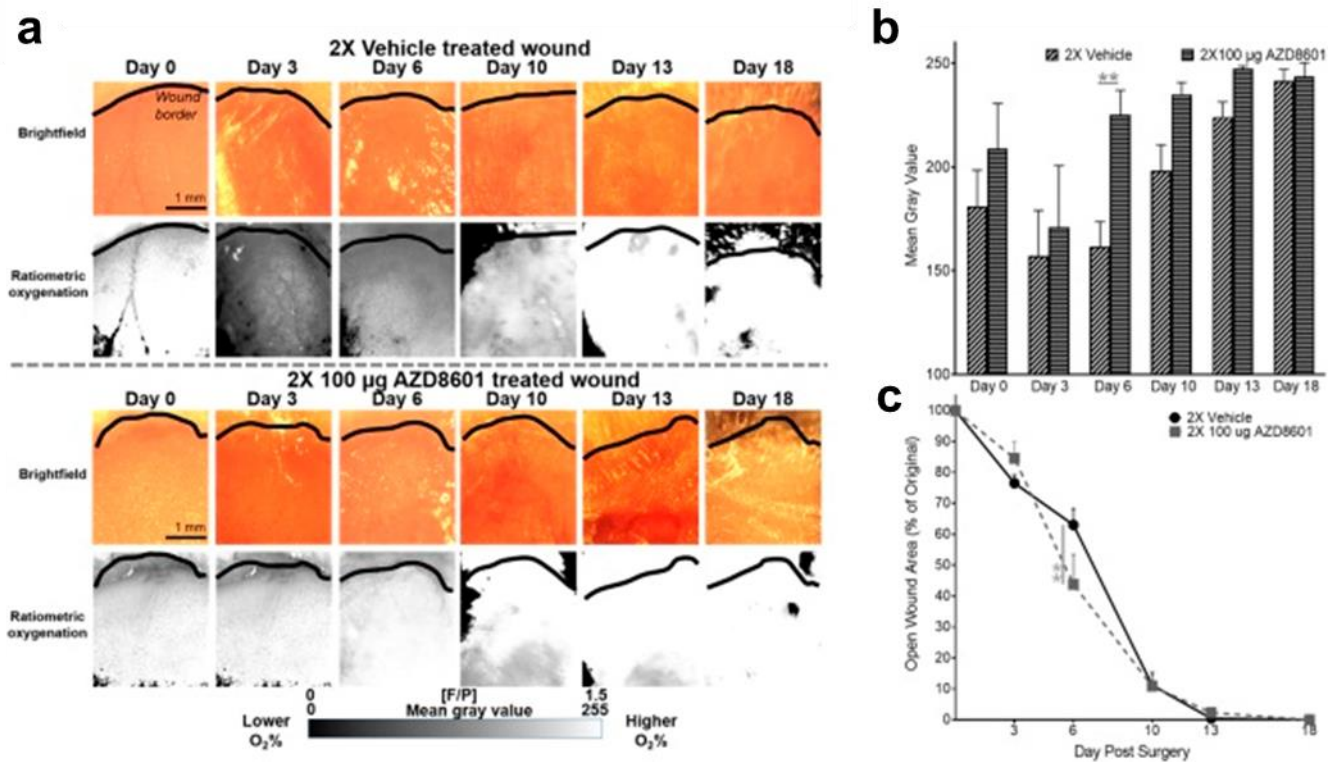
Fig. 4.10. AZD8601 treatment resulted in increased oxygenation of diabetic wound beds during healing. (a) Black and white ratiometric images of fluorescence/phosphorescence signal from BF2nbm(I)PLA (Difluoroboron β-diketonate poly(lactic acid)) nanoparticles revealed increased oxygenation in AZD8601-treated wounds. (b) Wound oxygenation as calculated by mean gray value of ratiometric images was significantly increased at day 6 post-surgery in the AZD8601-treated group. (c) Addition of BF2nbm(I)PLA nanoparticles to wounds did not impair healing. **$p < 0.01$, $n = 3$–4/group.

fluorescence/phosphorescence ratiometric outputs, was significantly increased on day 6 post-surgery in the double-injected AZD8601 group ($225 \pm 11.9\%$) as compared to the double-injected vehicle control ($161 \pm 12.2\%$). The improved tissue oxygenation was accompanied by the smaller open-wound size in the double-injected AZD8601 group ($44 \pm 9.6\%$) versus the double-injected vehicle control group ($63 \pm 5.2\%$) on day 6 (Fig. 4.10c).

4.4 Discussion

Capable of mediating efficient and localized expression of VEGF-A without eliciting innate immune responses, AZD8601 is ideally suited for VEGF-A therapies in a spatiotemporally confined manner and with low toxicity[10,11]. By promoting vascular remodeling and neovessel formation, this emerging therapeutic holds great potential in treating diabetic wound and cardiovascular diseases[18]. However, the *in vivo* efficacy and dosing pharmacokinetics of AZD8601 still remain incompletely understood.

Here, we dynamically, quantitatively and comprehensively examined the effects of AZD8601 on the vascular structure, function and associated oxygen supply/metabolism at the microscopic level *in vivo*, using multi-parametric PAM. Side-by-side comparison of the multifaceted microvascular response to AZD8601, VEGF-A protein, NT-VEGF-A mRNA, and citrate/saline vehicle showed pronounced, sustained, dose-dependent and AZD8601-specific vasodilation, blood flow increase, oxygen-metabolic upregulation, angiogenesis and neovessel formation (Fig. 4.2). Sequential dosing of AZD8601 at the same tissue location on day 0, 2 and 4 further boosted the early responses (i.e., day 7 or 14) in vasodilation and oxygen extraction/metabolism compared with single dosing, which, however, leveled out after 21 days (Fig. 4.5). Reducing the AZD8601 dose from 100 μg to 30 or 10 μg resulted in much compromised

and less enduring microvascular remodeling, along with abolished neovascularization (Fig. 4.7 and Fig. 4.8).

Promoting sustained vascularization and blood oxygen supply *in vivo*, AZD8601 demonstrated beneficial therapeutic effects on diabetic wound healing. In the established mouse model of diabetic wound, we showed that intradermal injection of AZD8601 after wounding significantly accelerated re-epithelization relative to administering citrate/saline vehicle. Sequential dosing of AZD8601 on days 0 and 3 increased early healing compared to single dosing on day 0. Further, the efficacy of AZD8601 was benchmarked to that of VEGF-A protein (Fig. 4.9), which has previously been shown to accelerate vascularization and wound healing in diabetic wounds[19]. In addition to the standard open-wound analysis, time-lapse monitoring of the tissue oxygenation within the wound area using the boron nanoparticle-based tissue oxygen sensor[16] revealed a strong correlation between the oxygenation level and the open-wound size, suggesting that the accelerated wound healing can be attributed, at least partially, to the AZD8601-facilitated re-oxygenation of the wound (Fig. 4.10).

It is worth pointing out that there is a high degree of coherence between the observations on the AZD8601-induced microvascular responses in the intact ear and the AZD8601-facilitated healing process in the diabetic wound. First, the significantly improved re-oxygenation of the wound in the AZD8601-treated mice nicely echoes the neovascularization and oxygen-metabolic upregulation induced by AZD8601 in the mouse ear. Second, increased dosage of AZD8601 resulted in both more pronounced microvascular responses in the ear (Fig. 4.4, Fig. 4.7 and Fig. 4.8) and more rapid healing of the wound (Fig. 4.9b). Last but not the least, sequential dosing of AZD8601 led to more significant early

microvascular responses versus single dosing in the ear, which, however, leveled out after 21 days (Fig. 4.6); this observation again nicely echoes that on the wound healing process, where sequential dosing of AZD8601 sped up the healing but did not lead to better end results compared with single dosing (Fig. 4.9a). Together, these observations support a bioactive effect for AZD8601, whereby the microvascular remodeling and oxygen-metabolic upregulation contributes to accelerated/improved tissue regeneration.

Relative to other pharmacological and cell-based treatments that have been shown to favorably impact re-epithelialization in murine models of delayed diabetic wound healing, AZD8601 induced comparable levels of wound healing acceleration[20]. However, treatment with AZD8601 is less expensive than stem cell therapy, and immunological rejection is not a complicating factor. Moreover, unlike treatment with VEGF-A protein, AZD8601 did not induce edema or the formation of micro-hemangiomas, as evidenced by a red blushing of the wound in our study. Since sequential topical dosing of recombinant human VEGF-A165 protein to chronic diabetic neuropathic foot ulcers has been clinically shown to reduce the time to complete ulcer healing[21], we expect that the clinical evaluation of AZD8601 in diabetic wounds could reveal a superior benefit to diabetic wound healing by promoting functional angiogenesis in the absence of edema and micro-hemangioma formation[22].

We caution against comparing the effects of recombinant VEGF-A protein on healing rates in the diabetic wound model (Fig. 4.9b) to its effects on volumetric blood flow, diameter, and tissue oxygenation in the healthy ear model (Fig. 4.2) because the dose of VEGF-A protein delivered to the diabetic wound was 72-fold higher than that delivered to the ear. Furthermore, the ear received injections of VEGF-A protein at three time points (day 0, 2 and 4; Fig. 3), while the wound received topical

applications of VEGF-A protein at five time points (day 0, 2, 4, 6 and 8 post wounding; Fig. 4.9). Because the VEGF-A protein-treated group served as the positive control in the wound healing study, the dose and dosing time course of VEGF-A protein were based on previously published data[19,21]. Based on the observed changes in the diabetic wounds treated with VEGF-A protein, we believe that this dose of VEGF-A protein is essentially an over-treatment that would not have been useful or plausible to repeat in the ear of healthy mice.

4.5 Conclusion

In summary, we demonstrate the pronounced, sustained and dose-dependent effects of AZD8601 on the microvasculature *in vivo* and its benefits to diabetic wound healing, including improved tissue oxygenation and accelerated healing rate without edema and micro-hemangioma. Out data provide strong preclinical evidence to support the potential clinical translation of this promising therapeutic[22]. Also, it is worth noting that it is the two innovative technologies that enable us to comprehensively evaluate the effects of AZD8601 on both blood oxygenation (PAM) and tissue oxygenation (boron nanoparticle-based oxygen sensor) in a noninvasive and longitudinal manner *in vivo*. Future integration of the two enabling technologies into a dual-modal system will open up new opportunities in cardiovascular research.

Reference

[1]   Nabel, E. G. & Braunwald, E. A Tale of Coronary Artery Disease and Myocardial Infarction. *New England Journal of Medicine* **366**, 54-63 (2012).

[2]   Landmesser, U. & Drexler, H. Chronic heart failure: an overview of conventional treatment versus novel approaches. *Nature clinical practice. Cardiovascular medicine* **2**, 628-638 (2005).

[3]   Varu, V. N., Hogg, M. E. & Kibbe, M. R. Critical limb ischemia. *Journal of vascular surgery* **51**, 230-241 (2010).

[4]   Brem, H. & Tomic-Canic, M. Cellular and molecular basis of wound healing in diabetes. *J Clin Invest* **117**, 1219-1222 (2007).

[5]   Ylä-Herttuala, S., Rissanen, T. T., Vajanto, I. & Hartikainen, J. Vascular endothelial growth factors: biology and current status of clinical applications in cardiovascular medicine. *J Am Coll Cardiol* **49**, 1015-1026 (2007).

[6]   Taimeh, Z., Loughran, J., Birks, E. J. & Bolli, R. Vascular endothelial growth factor in heart failure. *Nature reviews. Cardiology* **10**, 519-530 (2013).

[7]   Ferrara, N., Gerber, H. P. & LeCouter, J. The biology of VEGF and its receptors. *Nature medicine* **9**, 669-676 (2003).

[8]   Giacca, M. & Zacchigna, S. VEGF gene therapy: therapeutic angiogenesis in the clinic and beyond. *Gene therapy* **19**, 622-629 (2012).

[9]   Gaffney, M. M., Hynes, S. O., Barry, F. & O'Brien, T. Cardiovascular gene therapy: current status and therapeutic potential. *British journal of pharmacology* **152**, 175-188 (2007).

[10]   Zangi, L. *et al.* Modified mRNA directs the fate of heart progenitor cells and induces vascular regeneration after myocardial infarction. *Nature biotechnology* **31**, 898-907 (2013).

[11]   Lui, K. O., Zangi, L. & Chien, K. R. Cardiovascular regenerative therapeutics via synthetic paracrine factor modified mRNA. *Stem cell research* **13**, 693-704 (2014).

[12]   Carlsson, L. *et al.* Abstract 15533: A Biocompatible Chemically Modified mRNA Drives Sustained VEGF-A Protein Production, Human Endothelial Angiogenesis and Epicardial Progenitor Expansion, and Reduces Infarct Size and Partially Reverses Global Cardiac Dysfunction When Intracardially Injected One Week Post-Myocardial Infarction in the Pig. *Circulation* **134**, A15533-A15533 (2016).

[13]   Carlsson, L. *et al.* Biocompatible, Purified VEGF-A mRNA Improves Cardiac Function after Intracardiac Injection 1 Week Post-myocardial Infarction in Swine. *Molecular therapy. Methods & clinical development* **9**, 330-346 (2018).

[14]   Wang, L. V. & Hu, S. Photoacoustic Tomography: In Vivo Imaging from Organelles to Organs. *Science* **335**, 1458-1462 (2012).

[15]   Ning, B. *et al.* Simultaneous photoacoustic microscopy of microvascular anatomy, oxygen saturation, and blood flow. *Opt. Lett.* **40**, 910-913 (2015).

[16]   DeRosa, C. A. *et al.* Oxygen Sensing Difluoroboron β-Diketonate Polylactide Materials with Tunable Dynamic Ranges for Wound Imaging. *ACS sensors* **1**, 1366-1373 (2016).

[17]   Brian, S. *et al.* in *Proc.SPIE*.

[18]   Chien, K. R., Zangi, L. & Lui, K. O. Synthetic chemically modified mRNA (modRNA): toward a new technology platform for cardiovascular biology and medicine. *Cold Spring Harbor perspectives in medicine* **5**, a014035 (2014).

[19]   Galiano, R. D. *et al.* Topical vascular endothelial growth factor accelerates diabetic wound healing through increased angiogenesis and by mobilizing and recruiting bone marrow-derived cells. *The American journal of pathology* **164**, 1935-1947 (2004).

[20]   Amos, P. J. *et al.* Human adipose-derived stromal cells accelerate diabetic wound healing: impact of cell formulation and delivery. *Tissue engineering. Part A* **16**, 1595-1606 (2010).

[21]   Hanft, J. R. *et al.* Phase I trial on the safety of topical rhVEGF on chronic neuropathic diabetic foot ulcers. *Journal of wound care* **17**, 30-32, 34-37 (2008).

[22]   Mullard, A. mRNA-based drug approaches Phase I milestone. *Nature reviews. Drug discovery* **15**, 595 (2016).

Chapter 5 Photoacoustic microscopy of oxygen metabolism in mouse kidney after acute injury

5.1 Introduction

Sepsis associated acute kidney injury (SA-AKI) is a common cause of AKI accounting for nearly 50% of cases of AKI in the intensive Care unit[1,2]. It is a complex disorder associated with high morbidity and mortality, which could affect the downstream products of nitrogen metabolism, and/or the drop of urine output[3]. For the current translational and clinic research of AKI, tremendous efforts were made for diagnosing and classifying AKI such as urine volume (<0.5 ml/kg/hour for 6 hours)[4], blood serum creatinine levels (increase by 0.3 mg/dl within 48 hours, or 1.5 times of baseline within the prior 7 days)[5,6], and urinary biomarkers including matrix metalloproteinase-9 (MMP-9), N-acetyl-β-D-glucosaminidase (NAG), and kidney injury molecule-1 (KIM-1)[7]. Additionally, as a paired vascular organ for excretory, regulatory and secretory, kidneys have highly vascularized anatomy and receive approximately one fifth of the cardiac output[8], thus renal vascular structure has been also widely studied for AKI under hypertension or diabetes[9,10].

In recent years, besides the vasculature research of kidney, the functional quantification based on the anatomic characterization has been the focus of a number of studies, especially for the oxidative stress and renal blood flow, which have been tightly linked to sepsis–induced AKI. MRI[11], ultrasound[12], high-resolution microcomputed tomography (micro-CT)[13], and TPM[14,15] all hold great potential to study renal structure and function in rat and mice. However, there are technical bottlenecks in simultaneous quantification of three key hemodynamic parameters—C_{Hb}, sO_2 and peritubular capillary (PC) blood

flow—at the microscopic level, which prevents investigation of the underlying dynamic changes of renal MRO_2 in AKI. Other techniques have limitations that make them unsuitable for studies of kidney hemodynamics, as follows: 1) exogenous contrast agents, which can be used to visualize the kidney's microvascular structure and function, may cause perturbations in renal physiology, 2) high X-ray doses in micro-CT imaging may damage kidney hemodynamics and then limit the number of repeat measurements, and 3) the long lifetime of the phosphorescence agent required for TPM of blood oxygenation may significantly limit its speed[16].

To fill this technology gap, we have developed a new technique—intravital multi-parametric PAM. With the aid of a 3-D printed kidney cup, kidneys from anesthetized mice were exteriorized and then imaged by the label-free and noninvasive PAM, and hemodynamic parameters, including C_{Hb}, sO_2 and blood flow, were obtained simultaneously. Besides the functional quantification, a series of images for different tissue depths was also generated using the depth-resolved method. With this PAM-based intravital kidney imaging platform to simultaneously monitor the response in blood perfusion, oxygenation, and flow of the kidney microvasculature, we compared hemodynamics and oxygen metabolism in the kidney under normoxic and hypoxic conditions. Furthermore, multifaceted hemodynamic changes were comprehensively studied in the LPS-induced kidney sepsis AKI model.

5.2 Material and methods

5.2.1 Animals

8-week-old male C57/BL6 mice (weight 22±2g) from Jackson Laboratory (Bar Harbor, ME, USA) were used in this study. Mice had free access to food and water and were maintained under controlled

light-dark cycle (12:12-hour) during the entire experimental period. Experiments were performed in accordance with the NIH guide for Care and Use of Laboratory Animals, and all procedures were approved by the University of Virginia Institutional Animal Care and Use Committee.

5.2.2 LPS-induced kidney sepsis-AKI model

Sepsis was induced by a single intraperitoneal injection of LPS (Escherichia coli 0111:B4 strain, Sigma Aldrich, St. Louis, MO, USA; 5 mg/kg), and control mice received an equal volume of saline (i.p.). Animals were randomly divided into saline- (control) and LPS-treated groups. Briefly, mice were anesthetized with a mixture of ketamine hydrochloride (120 mg/kg) (MADA 043-304) and 12 mg/kg xylazine hydrochloride (Akorn Inc.), to keeping mice from waking up during the imaging process.

5.2.3 Normoxia *vs* hypoxia

By adjusting the oxygen concentration of the inhaled gas, hypoxic and normoxic state of the mice could be switched. For normoxia, the inhalation gas was the medical-grade air (AI M-T, Praxair); for hypoxia, the inhalation gas was mixed by medical-quality air (AI M-T, Praxair) and medical-quality nitrogen (NI-H, Praxair). For the normoxic condition, the oxygen concentration is 21%, while for the hypoxic condition, the oxygen concentration was set to 14% by adjusting the gas ratio of the two components, confirmed by a clinical anesthesia monitor (Capnomac Ultima, Datex-Ohmeda). Besides, 2% isoflurane was vaporized by the inhalation gas at a flow rate of 1.5 L/min, to keep the mice under anesthesia during the imaging process.

5.2.4 PAM system

As shown in Fig. 5.1a, two nanosecond-pulsed lasers (BX40-2-G, Edgewave; wavelength: 532 nm)

were used in the multi-parametric PAM system for mouse kidney imaging. For both lasers, the output beam was attenuated by a neutral-density filter (NDF; NDC-50C-2M, Thorlabs Inc.), and one of the beams was coupled into a polarization-maintenance single-mode fiber (PM-SMF; F-SPA, Newport) by a fiber collimator (FC; CFC-11X-A, Thorlabs Inc.) for Raman scattering-based wavelength conversion. The output of the PM-SMF was collimated by the same fiber collimator (FC; CFC-11X-A, Thorlabs Inc.) and purified by a bandpass filter (BPF; CT560/10bp, Chroma) to isolate the 558-nm beam. The 532-nm and 558-nm beams were combined via a dichroic beam splitter (DBS; FF552-Di02-25x36, Semrock), then coupled into a single-mode fiber (SMF; P1-460B-FC-1, Thorlabs Inc) through an objective lens (Newport, M-10X). To compensate the fluctuation of the laser intensity, ~5% of the laser energy was picked by a beam sampler (BSA; BSF10-A, Thorlabs) and monitored by a high-speed photodiode (PD; FDS100, Thorlabs). Fig. 5.1b is a diagram of the scanning head, which is mounted on a 2-axis transverse motorized linear stage (PLS-85, PI) for the raster scan and a vertical stage (KR15, THK) for the adjustment of focal plan. The output beam from the single-mode fiber was first collimated by an achromatic doublet (DL; Thorlabs, AC127-025-A), then focused by the same doublet with a correction lens (CL; LA1207-A, Thorlabs). The customized ultrasonic transducer (UT; inner diameter: 2.2 mm; outer diameter: 4.0 mm; focal length: 6.0 mm; center frequency: 35 MHz; 6-dB bandwidth: 70%) is ring-shaped, which allows the beam to pass through the central opening, and merged into a customized water tank for acoustic coupling. Fig. 5.1c is a diagram of the imaging area, where the anesthetized mouse was placed on a platform with a heating plate (Omega, SRFG-303/10) to maintain body temperature at 37 °C. The kidney was exteriorized and placed in a customized 3-D printed kidney cup; the agar, which is

transparent to the beam and ultrasonic wave, was applied around the kidney to stabilize it and prevent

dehydration and to insulate it from the motion caused by respiration and heartbeat. The two lasers, 3-axis

linear stages, photodiode and data acquisition card (ATS9350, AlazarTech) were controlled by a field-

programmable gate array (PCIe-7841R, National Instruments) via a self-developed LabVIEW program.
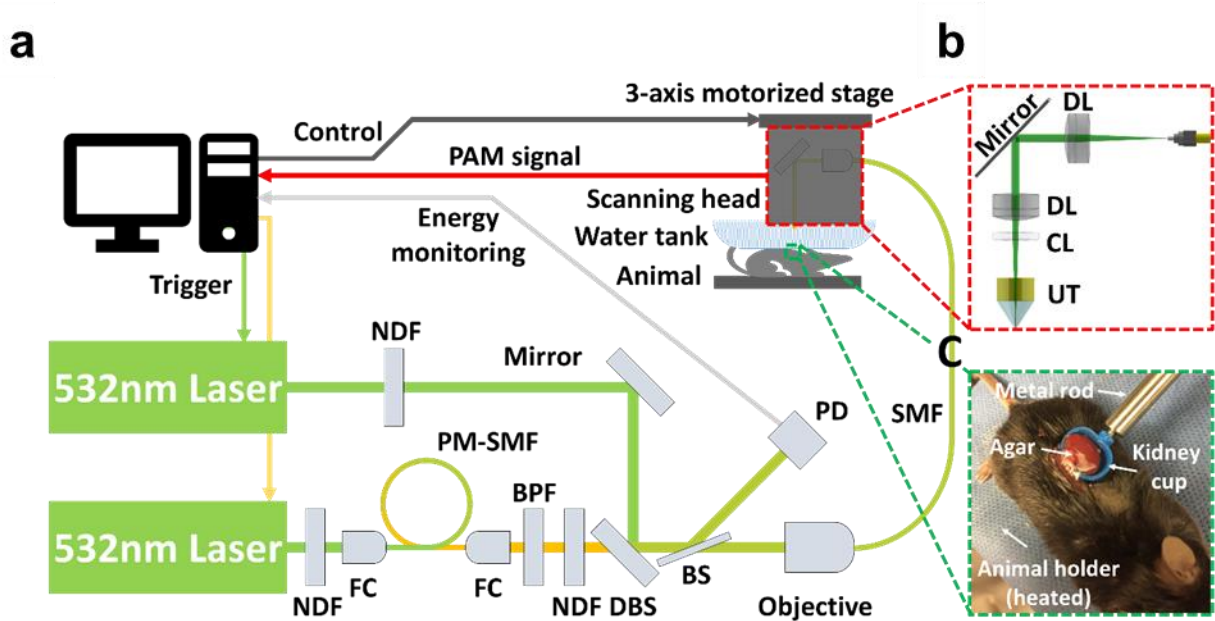
Fig. 5.1. Multi-parametric PAM platform for kidney imaging. (a) System schematic. (b) Blow-up of the scanning head boxed in (a). (c) Blow-up of the kidney cup boxed in (a).

5.2.5 Procedures for PAM imaging

Throughout the PAM experiment, the mice were maintained under general anesthesia kept body

temperature at 37°C using a rectal probe. The left kidney was exposed by opening the left flank, and after

gently teasing away tissue around the renal pedicle, the left kidney was gently exteriorized and secured

in the customized 3-D printed kidney cup designed to prevent stretching of the renal vessels. After the

agar solution (2% wt/vol; cooled to 40°C and 45°C) applied and solidified, a thin layer (~1 mm) of

ultrasound gel was applied on the surface of agar for acoustic coupling, then gel was in gentle touch against the bottom of the water, which was filled with temperature-maintained (37°C) deionized water, by slightly raising the animal holder. For the normoxia versus hypoxia experiment, PAM imaging was first performed under normoxic conditions (21% oxygen), then the mice were challenged with 14% oxygen (hypoxic condition) induced by nitrogen gas inhalation. For experiments monitoring the kidney microvascular network during LPS-induced sepsis-AKI, LPS (5 mg/kg, i.p.) was administered after the baseline imaging, then a series of PAM imaging was performed at 10, 20, 30, 40, 50, 60 and 80 min after LPS. At the end of experiments, all mice were euthanized by pentobarbital overdose (50 mg/kg), and tissue was collected. For an area of 1×1 mm^2 (e.g., Fig. 5.3 and Fig. 5.4), the acquisition time was ~10 min. Additional animals were treated with LPS and euthanized at various time intervals for measurement of kidney ATP levels and plasma creatinine.

5.2.6 Plasma creatinine assay

Blood was collected under anesthesia from the retro-orbital sinus, and plasma was prepared by centrifuging heparinized blood at 4,800 g for 5 min. Plasma creatinine was measured by enzymatic assay according to the manufacturer's protocol (Diazyme Laboratories, Poway, CA) but using twice the recommended sample volume; the accuracy of this method has been verified by LC-MS[17,18].

5.2.7 Kidney ATP assay.

ATP levels in mouse kidney were determined by CellTiter-Glo Luminescent Cell Viability Assay kit (Promega, no. G7571). Briefly, kidney tissue was placed in 5 ml of ice-cold 5% TCA (containing 10 mM dithiothreitol and 2 mM EDTA); kidney was cut into small pieces, homogenized, and incubated for

10 min on ice. Tissue homogenate was centrifuged for 10 min at 2000 × g, and the supernatant was stored at -20°C. Protein concentration was measured by optical density with a spectrophotometer according to the absorbance at 260 nm and the 260 nm/280 nm absorbance ratio (Nanodrop®, Thermo Scientific, Wilmington, DE, USA). The luminescence signal is proportional to the amount of ATP as an index of cell number.

5.2.8 Hematoxylin-eosin (H&E) and periodic acid-Schiff (PAS) staining.

Renal tissue was washed with PBS, fixed in 4% neutral formaldehyde solution, embedded in paraffin and sectioned. Sections were stained with H&E or PASand examined, under light microscopy. PAS, which strongly stains carbohydrates on the surface of proximal tubule epithelial cells and its useful to assess tubular injury and Trichrome which enable quantitative analysis of collagen deposition.

5.2.9 Real-time quantitative reverse transcription PCR (RT-qPCR).

Total RNA was isolated from renal tissue using the TRIzol Reagent (Life Technologies, Carlsbad, CA, USA) according to the manufacturer's protocol. RNA purity was evaluated by the A260/A280 ratio. Reverse transcription was performed with 800 ng of RNA in a total volume of 20 μl using the iScript cDNA Synthesis Kit (Cat.# 170-8891, USA) according to manufacturer's recommendations, the thermal cycler using the following protocol: 25°C for 5 min, 46°C for 20 min, 95°C for 1 min and hold at 4°C. For PGC1, the sense primer was 5'-GCT CTT CCT TTA ACT CTC CGT GTC-3', antisense 5' CTT GAC CTG GAA TAT GGT GAT CGG-3'; For   -actin, the sense primer was 5'-AAG ATC AAG ATC ATT GCT CCT CCT G-3'; antisense 5' AAA CGC AGC TCA GTA ACA GTC C-3'. RT-PCR was performed using an iCycler iQ Real-Time PCR Detection System (Bio-Rad) according to the manufacturer's manual.

A total of 100 ng of cDNA was subjected to pre-amplification using the SYBR Green qPCR SuperMix (Invitrogen, USA) in a total volume of 20 μl. The cycling conditions were 50°C for 2 min, 95°C for 10 min followed by 40 cycles, each one consisting of 15 s at 95°C and 1 min at 60°C. Samples were run in triplicate. The cycle threshold (Ct) values were exported into a Microsoft Excel worksheet for calculation of gene expression in accordance with the Ct method (Livak and Schmittgen 2001). All Realtime-PCR quantifications were carried out in triplicate for each sample, and the average was determined.

5.2.10 Statistical analysis

All statistical analyses were performed using the SigmaStat program (Systat Software) or GraphPad Software version Prism 11. Two-way repeated measures ANOVA was used to compare hemodynamic changes from PAM in the LPS-induced AKI group and saline-treated control group (Fig. 5.7a-c). An unpaired Student's t-test was used to compare ATP and ATP-related parameter changes from biological analysis, and when two unmatched group were compared, and a one-way ANOVA with Bonferroni's post-hoc test was used for group comparisons (Fig. 5.7d-f). All data were presented in the form of mean $\pm$ standard error of the mean (SEM). In all statistical analyses, *P value<0.05, **P value<0.01, ***P value<0.001, and ****P value<0.0001 was considered statistically significant.

5.3 Results and discussions

5.3.1 Multi-parametric PAM of mouse kidney

Using this new intravital PAM platform, we have acquired simultaneous imaging of C_{Hb}, sO_2 and blood flow speed in the mouse kidney at the microvascular level, as shown in Fig. 5.2. The clearly resolved microvascular networks of the mouse kidney showed a relative uniform distribution of the C_{Hb}

and flow speed in capillaries, but clear differences in sO$_2$. The dense vasculature anatomy resolved the peritubular capillaries, which is consistent with previous TPM results and PAM results[15,16,19]. Additionally, as the first-of-a-kind *in vivo* multi-parametric imaging platform, the quantified C$_{Hb}$, sO$_2$ and blood flow speed were also consistent with the established biological analysis[20]. These results demonstrate the feasibility of multi-parametric PAM for dynamic monitoring of renal oxygen metabolism in acute kidney injury, as well as chronic kidney disease *in vivo*.
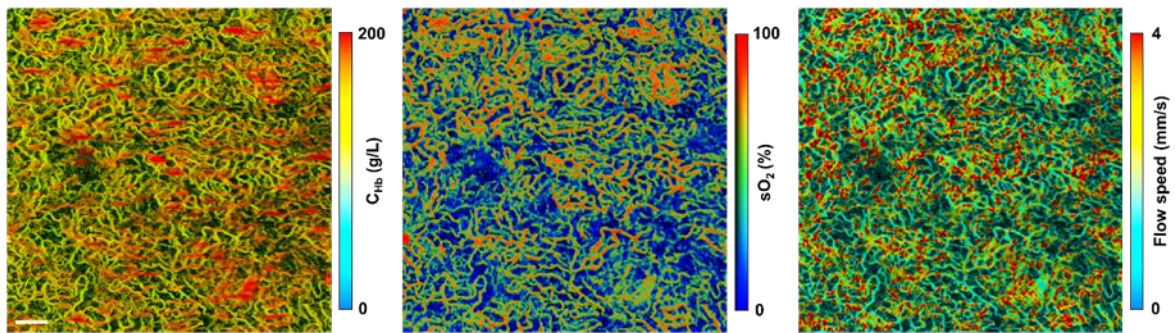
Fig. 5.2. Multi-parametric PAM images of the mouse kidney.

5.3.2 Depth-resolved image analysis of kidney

In addition to the quantitative images, a series of depth-resolved images were obtained by analyzing the raw A-lines for each B-scan, as shown in Fig. 5.3a. The upper and bottom boundaries of the A-line signals (yellow dash lines) was defined as the surface of the kidney and the maximum penetration depth (~200 μm), and the vascular structure (Fig. 5.3b) was obtained by applying the Hilbert transformation on the entire depth of the A-line signals.
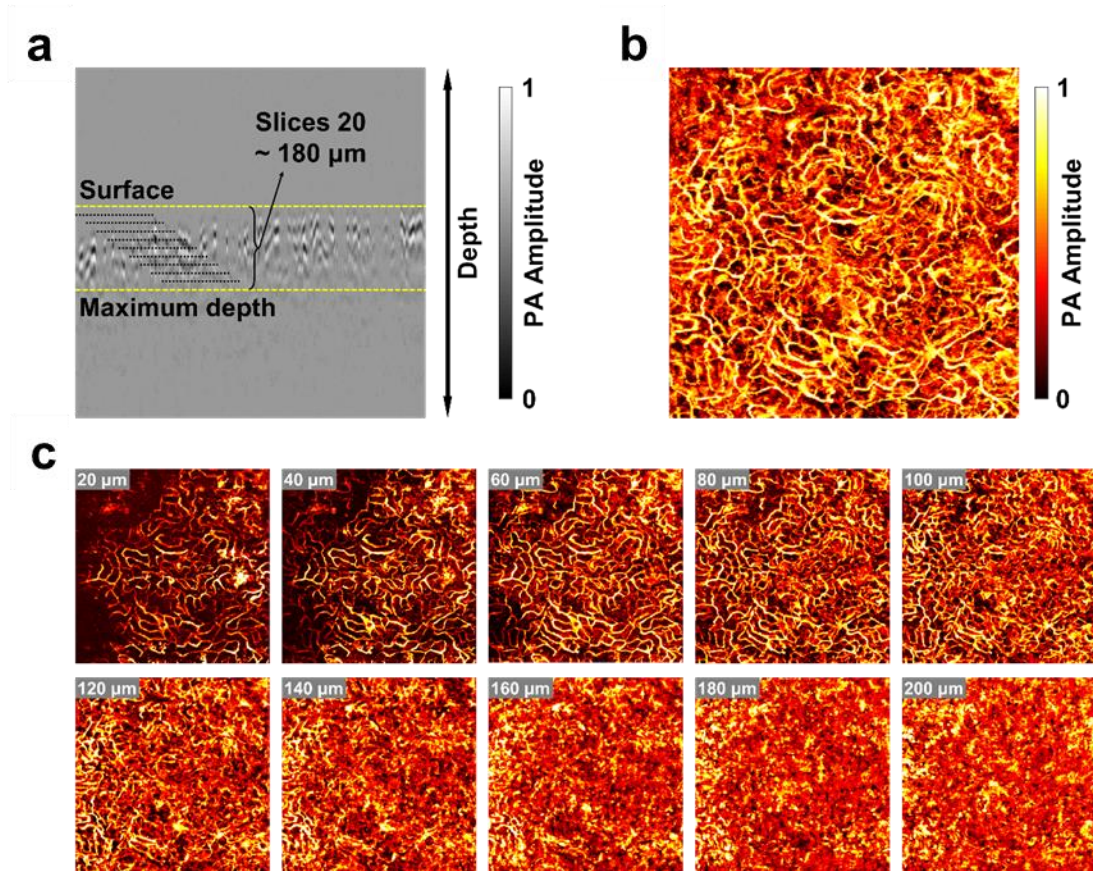
Fig. 5.3. Depth-resolved vascular structure by PAM kidney imaging platform. (a) x-z cross-sectional images of kidney acquired by multi-parametric PAM. (b) x–y maximum amplitude projection image of kidney vascular structure. (c) Vascular structure images reconstructed of different penetration depth in (a), starting from the surface to the maximum depth with the distance interval 20 μm.

By dividing the depth for a certain value (i.e., 20 μm), depth-resolved images were generated by applying the Hilbert transformation on the different depth interval (i.e., between the surface and 20 μm depth, between 20 μm and 40 μm depth, etc.), as shown in Fig. 5.3c. With increasing of depth, imaging of vascular anatomy moved from the superficial capillaries to somewhat deeper blood vessels.

5.3.3 Comparison of hemodynamic response in kidney under normoxia *vs* hypoxia

To explore the hemodynamic response under hypoxic conditions, we imaged the identical mouse kidney before and after the inhalation gas wasset to 14% oxygen concentration, as shown in Fig. 5.4.
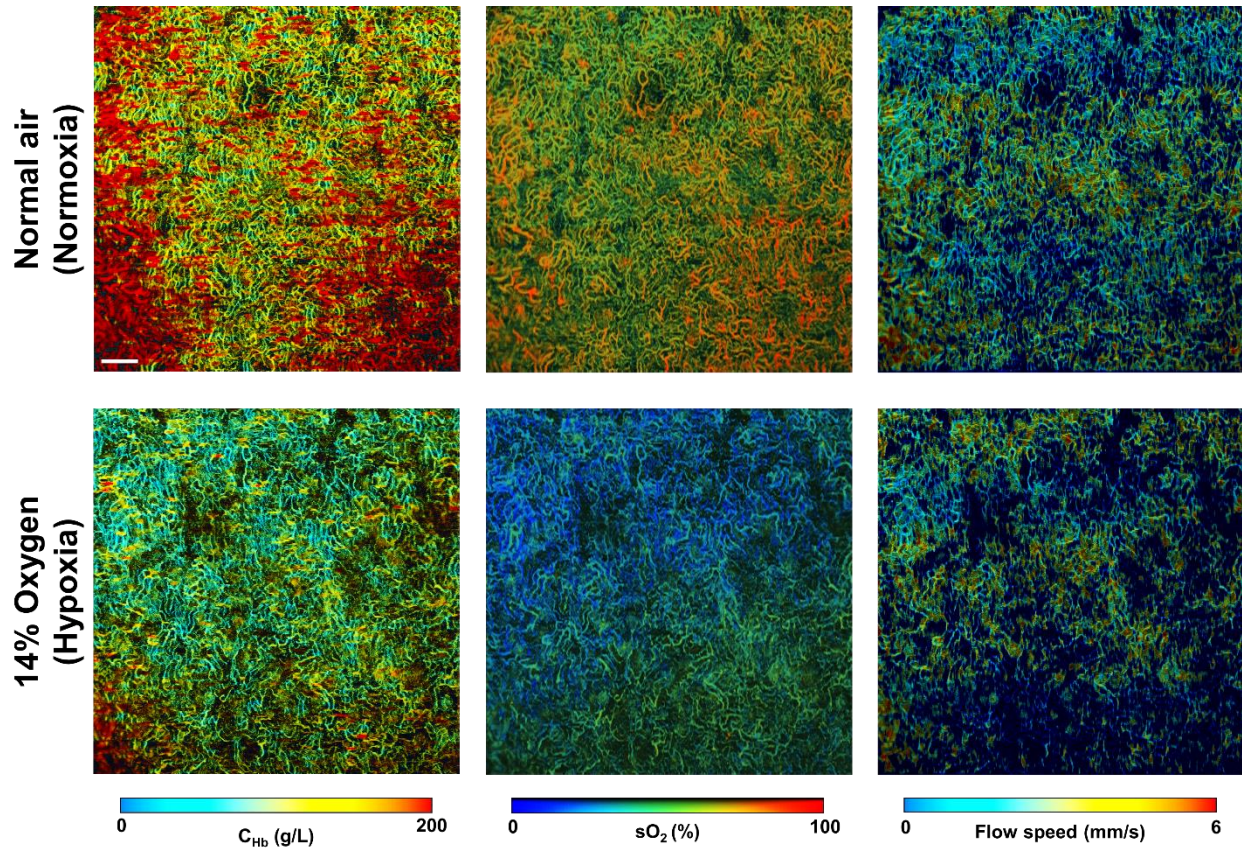
Fig. 5.4. Multi-parametric PAM of C_{Hb}, sO_2 and blood flow speed in the mouse kidney, in the absence and presence of systemic hypoxia. Scale bar: 200 μm.

The left column shows the PAM images using normal air, which are consistent with the multi-parametric PAM images of kidney in Fig. 5.2. Not surprisingly, with 14% oxygen, there was a dramatic drop of blood oxygenation (sO_2) accompanied by a reduced blood perfusion (C_{Hb}), showing a strong correlation with inhaled oxygen concentration. On the other hand, there was no significant change in

blood flow. Interestingly, in both conditions, but especially under hypoxia, there was a significant heterogeneous distribution of hemodynamics, implying a complex hemodynamic redistribution of kidney in response of hypoxia.

5.3.4 PAM of kidney in LPS-induced sepsis-AKI model

Using this new intravital PAM platform, , we collected a series PAM images of hemodynamic responses in kidney over an 80-min period after administration of LPS (Fig. 5.5), compared with a saline-treated control group (Fig. 5.6) with a 20-min time interval (10 min for the first two time points).
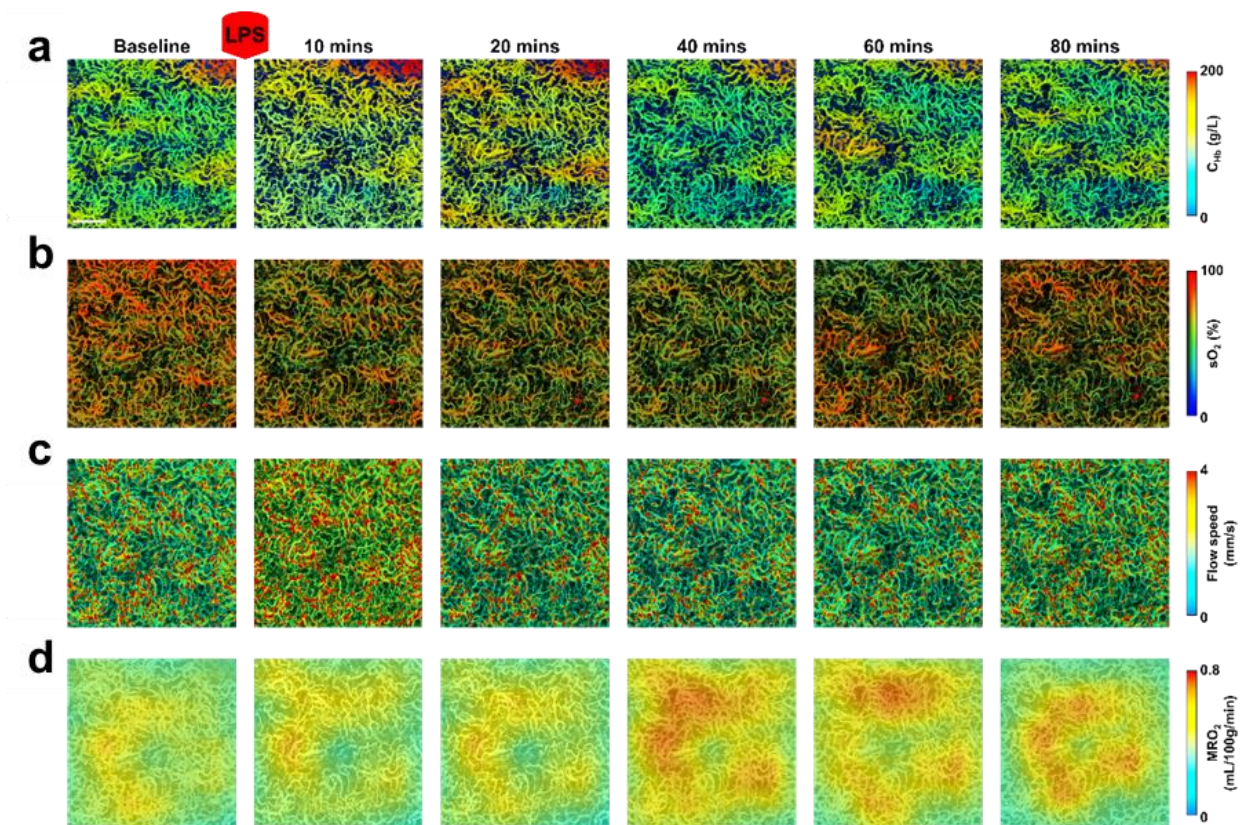
Fig. 5.5. Hemodynamic response of LPS-induced acute kidney injury. Scale bar: 200 μm.
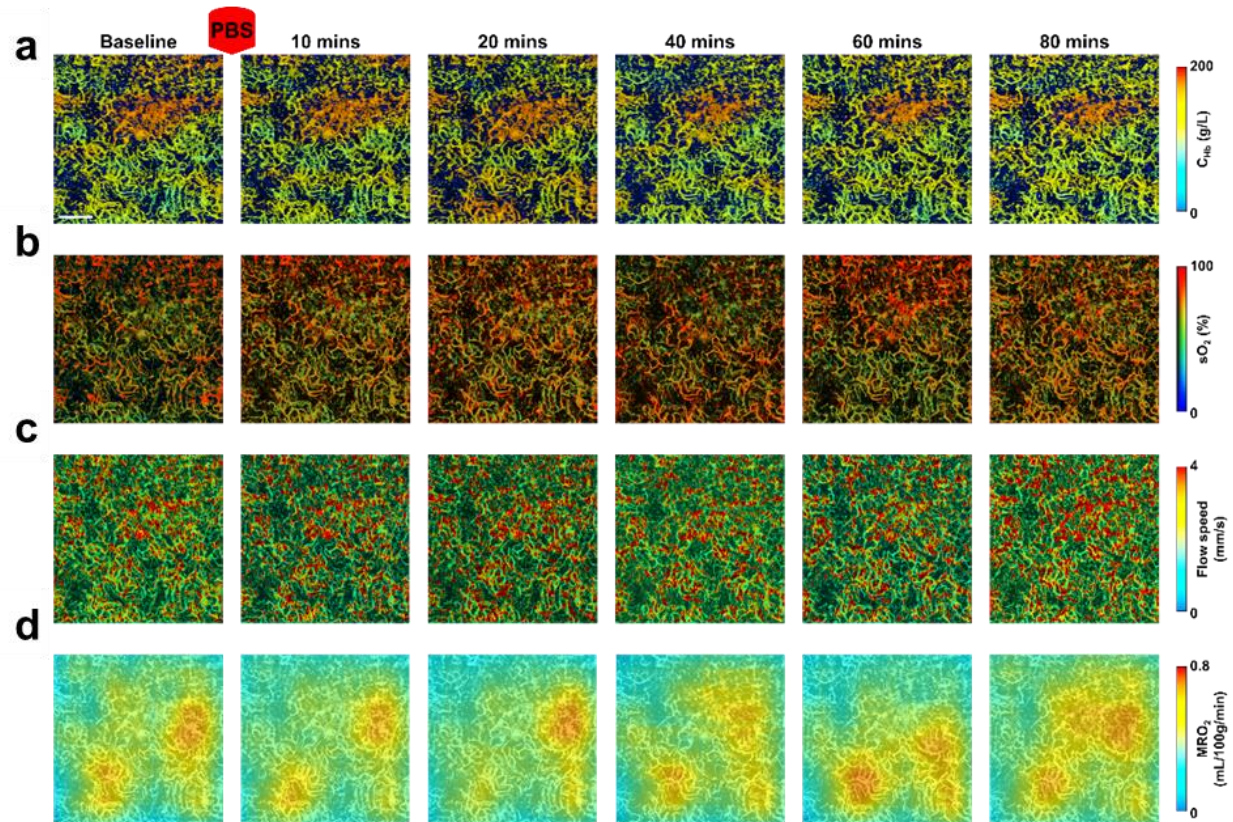
Fig. 5.6. Hemodynamic response of saline-induced control group. Scale bar: 200 μm.

A quantitative multi-parametric analysis was performed for the comparison of hemodynamic changes between the LPS- and saline-treated group (Fig. 5.7a-c). After LPS treatment, time dependent changes in hemodynamic parameters and kidney injury markers were observed (Fig. 5.7). Renal sO_2 began to decline immediately after 10 min and a ~30% decrease persisted from 20-80 min after LPS treatment compared with time matched control mice (Fig. 5.7b), while renal blood flow abruptly increased by ~10% within 10 min of LPS treatment but returned to and remained normal from 20-80 min (Fig. 5.7a). As a result, the calculated MRO_2 also gradually increased and had the maximum value (130% of pre-injection) 60 min after LPS injection and then dropped. These hemodynamic and metabolic

responses contrasted with the lack of changes in the saline treatment group. Again, the heterogeneous distribution of hemodynamics and metabolism implied a complex hemodynamic and metabolic redistribution of kidney in response of LPS injection.
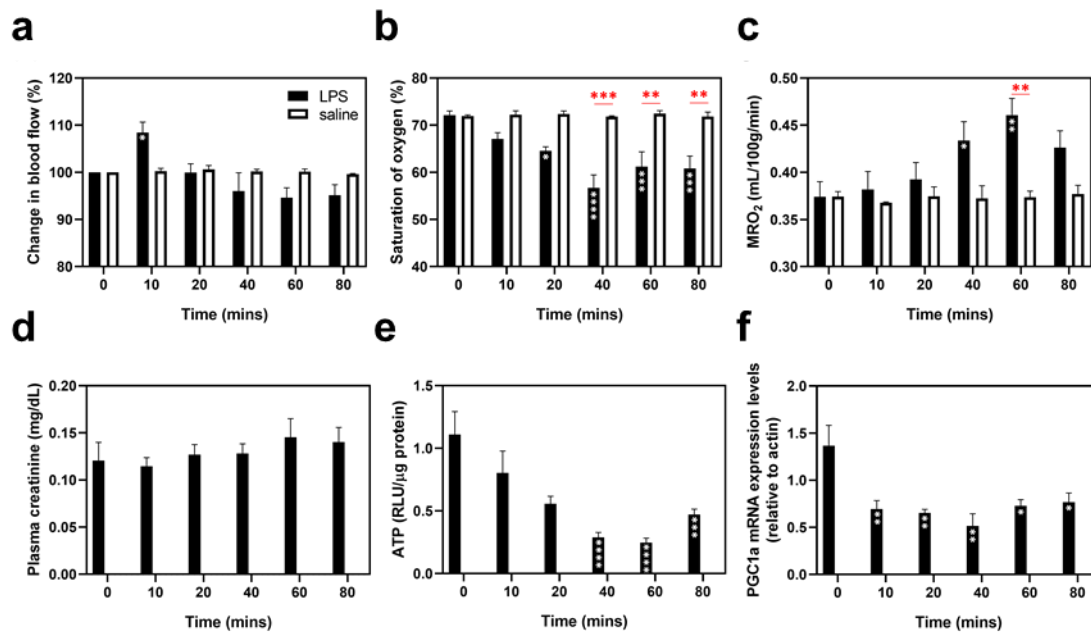
Fig. 5.7. Multi-parametric analysis of the hemodynamic response to LPS-induced acute kidney injury. (a-c) Relative changes (%) in blood flow speed, absolute change in sO_2 and after LPS or saline injection up to 80 minutes, respectively (n = 3-6/group). (d-f) Change in plasma creatinine, ATP levels, and mRNA expression after LPS injection up to 80 minutes, respectively (n = 3-6/time point). *$p < 0.05$, **$p < 0.01$, ***$p < 0.001$, and ****$p < 0.0001$. Data are presented as mean ± SEM.

5.3.5 ATP and kidney injury marker analyses of LPS-induced kidney sepsis-AKI model

To further explore the mechanism of the LPS-induced kidney sepsis-AKI model, and to better evaluate the quantification of hemodynamics by PAM, we measured kidney ATP levels, ATP-related mRNA expression level, as well as plasma creatinine level, an important indicator of kidney function

(Fig. 5.7d-f). The results showed that the change of oxygen stress was associated with ATP degeneration (Fig. 5.7e) as well as mitochondrial dysfunction (Fig. 5.7f) in the early stages of LPS-induced sepsis-AKI. Plasma creatinine (Fig. 5.7d) did not change significantly within the first 80 min after LPS injection, despite there already being an abnormal change in MRO_2, implying possible energy redistribution in the early stage of sepsis AKI.

5.4 Conclusion

Combining the intravital PAM system and the 3-D printed kidney cup, we have demonstrated simultaneous, high-resolution, label-free imaging of C_{Hb}, sO_2, and PC blood flow in the mouse kidney *in vivo* with a penetration depth of 200 μm. Challenging the animals with 14% oxygen, we observed strong correlation between sO_2 and the inhaled oxygen concentration. For the LPS-induced AKI model, we observed a rapid decrease in sO_2 within 40 min, then a slightly recovery after 80 min, which has a striking correlation with the renal ATP analysis. Overall, this PAM-based intravital kidney imaging platform allows simultaneous monitoring the response in blood perfusion, oxygenation, and flow of the kidney microvasculature following hypoxia. This technical innovation provides a new tool for AKI and chronic kidney disease studies.

Reference

[1]   Uchino, S. *et al.* Acute renal failure in critically ill patients: a multinational, multicenter study. *Jama* **294**, 813-818 (2005).

[2]   Angus, D. C. & van der Poll, T. Severe Sepsis and Septic Shock. *New England Journal of Medicine* **369**, 840-851 (2013).

[3]   Bellomo, R., Kellum, J. A. & Ronco, C. Acute kidney injury. *Lancet (London, England)* **380**, 756-766 (2012).

[4]   Kellum, J. A. & Lameire, N. Diagnosis, evaluation, and management of acute kidney injury: a KDIGO summary (Part 1). *Critical care (London, England)* **17**, 204 (2013).

[5]   Mehta, R. L. *et al.* Acute Kidney Injury Network: report of an initiative to improve outcomes in acute kidney injury. *Critical Care* **11**, R31 (2007).

[6]   Akcan-Arikan, A. *et al.* Modified RIFLE criteria in critically ill children with acute kidney injury. *Kidney International* **71**, 1028-1035 (2007).

[7]   Sierra, H., Cordova, M., Chen, C.-S. J. & Rajadhyaksha, M. Confocal imaging-guided laser ablation of basal cell carcinomas: an ex vivo study. *J Invest Dermatol* **135**, 612-615 (2015).

[8]   Chmielewski, C. Renal anatomy and overview of nephron function. *Nephrology nursing journal : journal of the American Nephrology Nurses' Association* **30**, 185-190; quiz 191-182 (2003).

[9]   Gattone, V. H., Evan, A. P., Willis, L. R. & Luft, F. C. Renal afferent arteriole in the spontaneously hypertensive rat. *Hypertension* **5**, 8-16 (1983).

[10]   Kimura, K., Tojo, A., Matsuoka, H. & Sugimoto, T. Renal arteriolar diameters in spontaneously hypertensive rats. Vascular cast study. *Hypertension* **18**, 101-110 (1991).

[11]   Kobayashi, H. *et al.* Renal tubular damage detected by dynamic micro-MRI with a dendrimer-based magnetic resonance contrast agent. *Kidney International* **61**, 1980-1985 (2002).

[12]   Lindner Jonathan, R. *et al.* Ultrasound Assessment of Inflammation and Renal Tissue Injury With Microbubbles Targeted to P-Selectin. *Circulation* **104**, 2107-2112 (2001).

[13]   Ehling, J. *et al.* Quantitative Micro-Computed Tomography Imaging of Vascular Dysfunction in Progressive Kidney Diseases. *Journal of the American Society of Nephrology : JASN* **27**, 520-532 (2016).

[14]   Ashworth, S. L., Sandoval, R. M., Tanner, G. A. & Molitoris, B. A. Two-photon microscopy: Visualization of kidney dynamics. *Kidney International* **72**, 416-421 (2007).

[15]   Dunn, K. W. *et al.* Functional studies of the kidney of living animals using multicolor two-photon microscopy. *American Journal of Physiology-Cell Physiology* **283**, C905-C916 (2002).

[16]   Sakadzić, S. *et al.* Two-photon high-resolution measurement of partial pressure of oxygen in cerebral vasculature and tissue. *Nat Methods* **7**, 755-759 (2010).

[17]   Inoue, T. *et al.* Vagus nerve stimulation mediates protection from kidney ischemia-reperfusion injury through α7nAChR+ splenocytes. *The Journal of Clinical Investigation* **126**, 1939-1952 (2016).

[18]   Keppler, A. *et al.* Plasma creatinine determination in mice and rats: An enzymatic method compares favorably with a high-performance liquid chromatography assay. *Kidney International*

71, 74-78 (2007).

[19]   Ogunlade, O. *et al.* In vivo three-dimensional photoacoustic imaging of the renal vasculature in preclinical rodent models. *American journal of physiology. Renal physiology* **314**, F1145-f1153 (2018).

[20]   Biology of the laboratory mouse. Edited by George D. Snell. Dover Publications, Inc., New York, 1956 (Reprint of first edition, 1941). viii + 497 pp. 16 × 24.5 cm. Price $6. *Journal of the American Pharmaceutical Association* **45**, 819-819 (1956).

Chapter 6 Long-term cortex-wide functional imaging of the awake mouse brain using multi-parametric photoacoustic microscopy

6.1 Introduction

Multi-parametric PAM has become a promising, useful tool in biomedical research for small-animal neuroimaging[1-10]. Taking advantage of the photoacoustic effect, PAM offers many advantages in biomedical imaging, including high spatial resolution, high image contrast, and deep tissue penetration past the optical diffusion limit. Moreover, by using endogenous absorbers and exogenous contrasts, multi-parametric PAM is able to achieve functional and molecular imaging, making it a very versatile and attractive imaging modality[11]. Researchers, capitalizing on PAM's capabilities, have been able to apply the technology in recent years to study neuroprotection against ischemic stroke[12], neurovascular coupling[13], Alzheimer's disease[14], cancer[15], and electrophysiological neural activity[9]. With the rapid advancement of its imaging capabilities and the increasing attention in the field, PAM has a bright future in expanding its research applications to pave way for its clinical adoption.

In order to conduct small-animal cortical imaging, several techniques have been widely adopted in the field, but they present significant drawbacks. Transcranial PAM imaging through the intact skull are desirable because of its noninvasive nature, but due to optical scattering of the skull, it either requires the use of very young mice (<10 weeks old)[4] or sacrifices high spatial resolution at the micron level for a deeper imaging depth[16,17]. To reduce or eliminate the signal interference from the skull, invasive procedures of either skull thinning or cranial window installation are used. Skull thinning procedures are shorter and have a smaller learning curve, but its imaging depth is still limited due to the remaining

skull[18]. Furthermore, due to bone regrowth, repeated procedures are required to conduct longitudinal studies, which increases the risk of brain injury due to mechanical stress of the drill and limits the number of available timepoints for imaging[19,20]. A craniotomy, followed by the installation of a chronic cranial window, is the best available option of eliminating the skull scattering effects to maximize tissue penetration and achieve resolution at the micron level. This procedure is very suitable for longitudinal monitoring studies, but it requires highly skilled surgeons. Furthermore, significant challenges still remain, including a short window lifetime due to either dura thickening or skull regrowth[20], small window size[20-23], and the need for repeated procedures[22], which paves way for further improvements.

To address these limitations, Kim et al. presented a curved glass cranial window protocol for TPM that demonstrated long-term monitoring of the bilateral cortex for 8 weeks without dura thickening or bone regrowth[24]. Although this is a significant improvement compared to prior window preparations, the curved glass is not suitable for PAM imaging due to its interference with the ultrasound signal. A robust cranial window tailored to PAM brain imaging still remains unavailable.

In the present study, we have developed the first-of-a-kind long-lifetime (>5 months), cortex-wide (6×8 mm^2), and light-weight (<2 g) cranial window with dual transparency to both light and ultrasound, which is tailored to perform multi-parametric PAM of the awake mouse brain. Capitalizing on the long window lifetime, we have tested the restoration of the BBB and have further applied it to study the cerebrovascular responses to ischemic stroke for up to 28 days, which demonstrates some of its new and exciting potential applications.

6.2 Methods

6.2.1 Custom-made 3-D printed head frame

To allow for long-term awake monitoring, the in-house head-mounted frame (Shapeways, New York City, New York) is designed and optimized to be light-weight (2g) while retaining its stiffness and durability. The 3-D printed material we used is the PA12 multi jet fusion plastic, which offers the mechanical properties that we desired. The center of the head frame is hollow to allow for an 8 mm by 6 mm window (with transparent acetate film underneath sealing the exposed tissue) for PAM access to the bilateral cerebral cortex. The bottom of the frame is curved and fitted to the average skull curvature of CD-1 mice at 6-10 weeks, so that the frame can be securely installed onto the exposed mouse skull without the risk of loosening and shortening the lifetime of the window. The extended lateral wings of the head frame have a bore large enough to thread a #4-40 screw down to secure onto another custom machined metal arm-piece. The head frame is thick enough to maintain rigidity during imaging, allowing awake mouse imaging for a stable image acquisition.

6.2.2 Animal preparation

1. The mouse is anesthetized by isoflurane in an induction chamber and vaporizer unit (EZ-SA800, E-Z Systems Inc, Palmer, Pennsylvania). Induction occurs at 4% for 30 seconds, followed by 2% isoflurane until the animal is fully anesthetized (slow and rhythmic breathing is observed). Toe pinch is performed to ensure that the animal is fully anesthetized.

2. The mouse is secured on a homemade stereotaxic surgical station with a homeothermic monitoring system with heating pad (No. 69020, RWD life science, Dover, Delaware) set at 37°C. 2%

isoflurane will be continuously administered through the homemade nose cone throughout the procedure and decreased to ~1% as needed.

3. Administer subcutaneously carprofen (5 mg/kg) to prevent an inflammatory response and dexamethasone (0.2 mg/kg) to prevent swelling of the brain.

4. Lubricate both eyes with ointment (Stye™, Lynchburg, Virginia) to prevent them from drying out. Remove hairs on the scalp using an electric trimmer, and then remove residual hairs using commercial hair trimmer (9990-1301, Wahl Clipper Corp., Sterling, Illinois).

5. Disinfect scalp using a povidone-iodine solution and wipe with 70% ethanol prep pads.

6. Using sterilized surgical scissors (MDS10030, Medline Industries, Mundelein, Illinois) to remove the skin over the top of the skull (scalp), starting with a horizontal incision along the base of the head, followed by two cuts in the rostral direction, almost reaching the eyelids, then two oblique cuts that converge at the midline (Fig. 6.1a-1). Apply lidocaine HCl 1% + epinephrine 1:100,000 solution onto the periosteum to avoid excessive bleeding or pain during craniotomy. Retract and remove the periosteum to the edges of the skull with a scalpel (6008T-10, Medline Industries, Mundelein, Illinois). Also, lightly retract the musculature of the back of the neck until the interparietal bone is completely exposed. Gently scrape the entire exposed area of the skull with the scalpel to create a dry surface, which will allow the glue to adhere better when applied later (Fig. 6.1a-1).

7. Demarcate the area to be removed using a fine point marker. This area is roughly a 7 mm by 5 mm trapezoid located with the longer base at 1 mm rostral to the lambda and the shorter base at 2-3 mm rostral to the bregma. Under a microscope (SM-3B, AmScope, Irvine, California), etch out a shallow

groove along the demarcated area with the dental drill (K.8350-H.30, Foredom, Bethel, Connecticut) with a 0.7 mm diameter drill bit (FG, Shofu Dental, San Marcos, California). After a slight drilling, apply lidocaine + epinephrine solution again onto the skull surface. Stop drilling every 20-30 seconds to remove bone dust using sterile saline and cotton swabs and to avoid overheating the skull. Once a shallow groove is created and blood vessels are visible underneath the groove, switch to a 0.5 mm diameter drill bit (CN1, Shofu Dental, San Marcos, California) and continue creating a deeper groove. Completely stop drilling when a very thin layer of bone is left. With forceps, gently push on the inner edge along the perimeter of the bone flap to determine if the entire bone flap is loose. The bone flap is ready for removal when it is entirely loose (Fig. 6.1a-2).

8. Prepare the 0.6% agarose and store in a 37°C water bath for later use.

9. Cut out the surgical sponge (ETH1972, Medline Industries, Mundelein, Illinois) into rectangular pieces large enough to cover the entire window area. Soak the sponges in sterile saline until completely soft.

10. Cut out a piece of transparent acetate film with 0.003-inch thickness (Dura-Lar Film, Grafix, Maple Heights, Ohio) that is slightly larger than the central bone flap. Sterilize with alcohol swabs and soak in sterile saline.

11. Immerse the entire skull with sterile saline. Then, gently lift up the central bone flap with very fine-tip forceps by taking advantage of the bone trabeculae. The saline will help prevent bleeding of the dura. Tip: apply the forceps horizontally nearly parallel to the bone flap to avoid accidentally puncturing the underlying tissue (Fig. 6.1a-3).

12. Apply the soaked surgical sponges onto the exposed cortex to stop any bleeding, flush with sterile saline as needed. This step can take up to 30-40 mins (Fig. 6.1a-4).

13. After drying the dura mater surface and ensuring that there is no further bleeding, mix a drop of epoxy resin and hardener (8 oz, ArtResin, Carrollton, Texas) together. Apply the resin along the edge of the window with a fine-tipped applicator. Ensure that all bone edges are covered to prevent future bone regrowth. After the epoxy resin solidifies (~5 min), flush the window area with sterile saline again to void drying out the cortex and dura (Fig. 6.1a-5).

14. Carefully dry the surrounding skull with Kimwipes, and then apply a few drops of the agarose onto the exposed cortex with a 0.3 cc syringe (Fig. 6.1a-6).

15. We recommend that steps 15-16 are completed with the help of an assistant. Gently lay the pre-cut clear acetate film onto the window area on top of the agarose. With a pair of thumb forceps, the assistant uses each prong to press down on the 2 non-parallel sides near the edge of the film until flush against the skull following its natural curvature. Carefully dry off the surrounding agarose with Kimwipes, while ensuring that a sufficient amount remains under the film so that no air bubble accumulates. Reposition the film as needed so that it rests directly at the center of the window area, with ~1 mm of film overlapping the skull on all 4 sides (Fig. 6.1a-7).

16. Once the correct position is reached, it is crucial for the assistant to remain steady and ensure that the film does not shift away from its position. In the meantime, the main surgeon carefully applies gel-based cyanoacrylate glue (234790, Loctite, Hartford, Connecticut) to the edge of the window on all 4 sides with the help of a needle point. Tip: Be careful not to accidentally apply glue onto the center of

the window, in which case the film will need to be replaced and reapplied. Once all 4 sides are secured with cyanoacrylate glue, allow for 1 additional minute to cure, then the assistant can carefully lift up the forceps. Make sure that there is no excessive glue on the 4 edges to allow for a flush attachment of the head frame in a subsequent step (Fig. 6.1a-8).

17. Using the 0.7 mm diameter dental drill, create 3 deep indents on the intact skull: 2 on each side of the interparietal bone near the caudal end, and 1 on either side of the nasal bone near the coronal suture. Allow sufficient room for placement of the 3-D printed head frame. Install 3 bone screws (90065A013, McMaster-Carr, Elmhurst, Illinois), 1 in each indent with a screwdriver. Only about 1 full rotation is needed to secure the screws. Ensure that the screw is not inserted too deep to avoid damaging the underlying tissue (Fig. 6.1a-9).

18. Apply a layer of cyanoacrylate along the bottom of the curved surfaces of the head frame. Then center and place the head frame onto the window area. Apply gentle downward pressure for about 30 seconds to allow for the glue to cure.

19. Once the frame is secured onto the skull and film, apply more glue along the outer edges of the frame, where it meets the skull, to create a tighter connection. Allow time for the glue to cure. Then mix dental cement (S396, S398, and S371, Parkell, Edgewood, New York) and apply it throughout the exposed skull surface. Apply more cement near the gaps between the frame and skull to create a stronger seal. Ensure that there is no excessive cement applied onto the exposed skull under the 2 lateral wings of the frame so that the head will fit in between the 2 prongs on the metal arm piece. Also ensure that all

exposed edges of the skin are covered by cement. Allow for 10-15 minutes until the dental cement is solidified (Fig. 6.1a-10).

20. Subcutaneously inject 5 mg/kg Ketoprofen post-surgery and stop administering anesthesia. Allow time for the mouse to recover from anesthesia before returning to the cage. The entire procedure takes roughly 3-3.5 hours on average to complete.

21. Administer 5 mg/kg Ketoprofen subcutaneously every day for 3 days post-surgery to minimize inflammation and pain. Watch for any signs of distress and ensure that the mouse has easy access to food and water.

22. The mouse will be subject to 5 training sessions on 5 consecutive days to help the mouse relieve the head restraint-induced stress. Each training session lasts for 45 minutes. During the training session, the mouse will be provided with a palatable drink as a positive reward. If the mouse struggles continuously against the head restraint for more than 30 seconds, it will be released and put back in the cage for a 10-minute rest. The mouse body temperature will be kept at 37 degrees using a heating lamp or pad. If the mouse fails to acclimate to the restraint after all 5 training sessions, it will be euthanized.

All experimental methods were carried out in conformity with the animal protocol approved by the Animal Care and Use Committee (IACUC) at the University of Virginia.
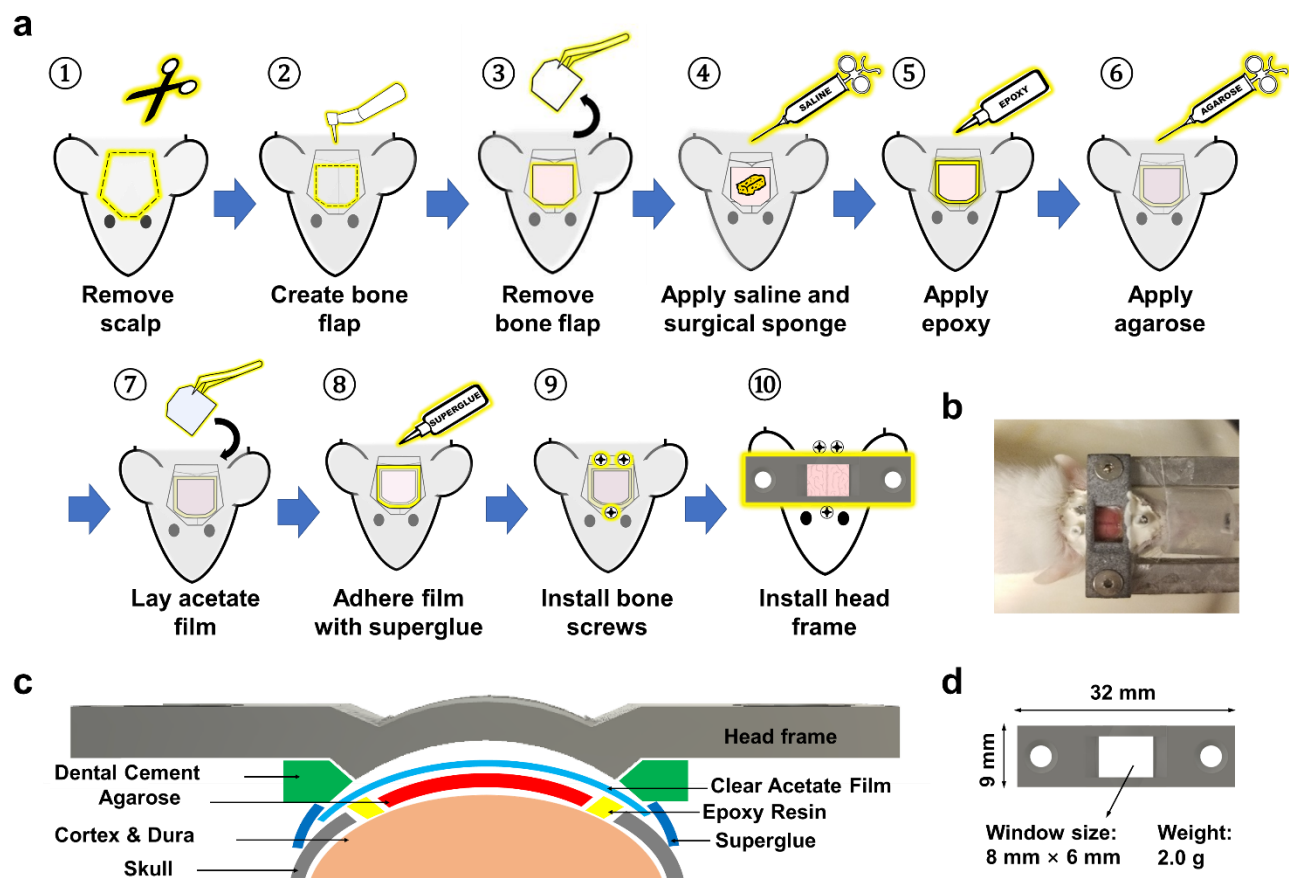
Fig. 6.1. Schematic of the cranial window protocol. (a) Major steps of the cortex-wide cranial window installation procedure. (b) Overhead view of the mounted animal post-cranial window installation. (c) Schematic of the coronal cross section of the cranial window. (d) Dimensions and weight of the custom-made 3-D printed head frame.

6.2.3 Longitudinal monitoring procedure

1. Following steps 1-22 of the protocol detailed in the "Animal Preparation" section, a cranial window was prepared. After the cranial window installation, 2 weeks was allowed for recovery, for any signs of inflammation and hemorrhages in the brain to subside.

2. To acquire the first set of PAM images (2 weeks post-surgery), the animal was transferred to the air-floated spherical treadmill, and the head was stabilized by mounting the plastic cranial window frame onto the metal arm-piece with screws.

3. To ensure the mouse's voluntary movement under its own weight, the height of the treadmill was adjusted. The translational and rotational alignment of the ROI on the mouse head was adjusted, so the plane of the ROI was positioned directly underneath and perpendicular to the scanning head. During the awake condition, room air was administered to the mouse through the nose cone. A 36.5 °C water bath held by an optically, acoustically transparent membrane separated the scanning head from the ROI. And for acoustic coupling, ultrasound gel was applied within the area of the cranial window against the transparent plastic membrane. The PAM image was then acquired.

4. Once the structural PAM imaging was complete, the animal was transferred back to the cage. Subsequent PAM images were taken of the mouse weekly for 4 weeks, then monthly for 24 weeks.

5. The mouse was monitored for signs of pain throughout the timeline of the longitudinal study.

6. Once the series of longitudinal structural PAM imaging was complete, the mouse was euthanized.

6.2.4 Awake *vs* anesthesia procedure

1. Following steps 1-3 of the protocol detailed in the "Longitudinal Monitoring Procedure" section, the animal was transferred to the air-floated treadmill.

2. Once the animal head was stabilized and the cranial window was secured to the metal-arm piece, the delivery of isoflurane ceased. The animal was then allowed to regain wakefulness.

4. Functional and structural PAM images were acquired in this awake condition.

5. For the anesthesia condition, the animal remained on the treadmill. 2% isoflurane was subsequently delivered to the mouse for 15 minutes through the nose cone. Once the animal was completely anesthetized, an additional set of PAM images was acquired.

6. After the completion of the experiment, the animal was euthanized immediately.

6.2.5 Photothrombosis procedure

1. Following steps 1-22 of the protocol detailed in the "Animal Preparation" section, a cranial window was prepared. After the cranial window installation, 2 weeks was allowed for recovery, for any signs of inflammation and hemorrhages in the brain to subside.

2. A 20mg/mL solution of Rose Bengal was prepared. 1mL Rose Bengal was then administered to the animal via intravitreal injection. Utilizing an optical laser mask to isolate a 2mmx1.5mm area of vessels in the lower left quadrant of the cortical region, a 532nm laser was focally shined upon the vessels of interest through the cranial window to induce a local ischemic stroke for 15 minutes.

3. Once 3 hours had elapsed, following steps 2-3 of the protocol detailed in the "Longitudinal Monitoring Procedure" section, the animal was transferred to the air-floated treadmill, where structural and functional PAM images were acquired.

4. Once the structural PAM imaging was complete, the animal was transferred back to the cage. Subsequent PAM images were acquired on day 1, 4, 7, 14, 21, and 28, relative to the time of Rose Bengal injection and laser illumination.

5. The mice were monitored for signs of pain throughout the timeline of the study.

6. Once the series of PAM imaging was complete, the mouse was euthanized.

6.2.6 BBB procedure

1. Following steps 1-22 of the protocol detailed in the "Animal Preparation" section, a cranial window was prepared. After the glue and dental cement was allowed to cure for an hour, a baseline PAM image was acquired. Then, 2% (w/v) Evans blue dye at the dose of 4 ml/kg animal's body weight was administered to the animal via tail vein injection.

2. Once 2 hours had elapsed for Evans blue to be fully extravasated, following steps 2-3 of the protocol detailed in the "Longitudinal Monitoring Procedure" section, the animal was transferred to the air-floated treadmill. Structural and functional PAM images were acquired to measure the BBB leakage at the time of the cranial window installation procedure.

3. For each subsequent time point, a separate cranial window was prepared and the Evans blue injection was again administered in the animal after the selected number of days following the initial cranial window procedure. Again, 2 hours elapsed to allow for full Evans blue extravasation post-injection before acquiring the PAM image.

4. PAM images were acquired on day 0, 7, 14, and 18 relative to the time of the animal's initial surgery.

5. After the completion of each experiment, the animal was euthanized immediately.

6.2.7 Cranial window *vs* intact skull

1. Following the steps 1-6 of the protocol detailed in the "Animal Preparation" section, the skull of the animal was exposed and cleaned.

2. While anesthetized under 2% isoflurane, the animal was transferred to a heating pad set to 36.5 °C. Translational and rotational alignment of the ROI on the mouse head was adjusted so the most superior point of curvature of the skull was positioned directly underneath and perpendicular to the scanning head. A 36.5 °C water bath held by an optically, acoustically transparent membrane separated the scanning head from the ROI. And for acoustic coupling, ultrasound gel was applied to the skull against the transparent plastic membrane. The structural and functional PAM image was then acquired of the in-tact skull.

3. The animal was then transferred back to the stereotaxic surgical station to complete the remaining procedure, in accordance with steps 7-22 of the protocol detailed in the "Animal Preparation" section.

4. After the glue and dental cement cured following completion of the cranial window installation procedure, in accordance with steps 2-3 of the protocol detailed in the "Longitudinal Monitoring Procedure" section, the animal was transferred again to the air-floated treadmill. PAM image was then acquired of the visible cortex through the cranial window.

5. After the completion of the experiment, the animal was euthanized immediately.

6.2.8 Statistical analysis

The two-way repeated measures ANOVA was used to compare the hemodynamic change for the longitudinally monitoring after the frame installation up to 24 weeks post installation in Fig. 6.3, for the ipsilateral hemisphere and contralateral hemisphere during the photothrombosis experiments in Fig. 6.5, as well as in the awake mouse and anesthesia mice in Fig. 6.4. The paired t-test was used to compare the initial hemodynamic parameters for the photothrombosis experiment before Rose Bengal injection. In all

statistical analysis, p<0.05 was considered significant. All data were presented in the form of mean ± standard deviation.

6.3 Results

6.3.1 Intact Skull *vs* cranial window

Only structural images alone were obtained for this experiment. Using the same mouse under similar imaging conditions, the image acquired with the skull intact exhibits poor imaging quality. As can be observed in Fig. 6.2a (left), the superior sagittal sinus is not visible, its daughter vessels show a weak contrast relative to the background, and the microvessels cannot be resolved due to the scattering effects of the skull. As demonstrated in the expanded view, very few microvessels can be observed from the image, and they show a weak signal strength, resulting in the poor image contrast. Additionally, the sparsely distributed vasculature within the skull, which appears as thin, bright, and tortuous structures, obstruct the underlying vessels of interest. Contrarily, once the skull is removed and the cranial window is installed, the imaging contrast and resolution visibly improve as the microvasculature exhibits greater clarity (Fig. 6.2a, right). The superior sagittal sinus and its daughter vessels are clearly visible with great imaging contrast and well-defined boundaries. In the blowup view, more microvessels can be observed in the image, which collectively exhibit a much-improved contrast and resolution compared to its intact skull counterpart. This side-by-side comparison demonstrates the competitive advantage of using cranial windows for cortex-wide PAM imaging over intact skull preparations.

Fig. 6.2. PAM imaging with and without the in-tact skull and restoration of BBB over time. (a) Structural PAM images of the cortical vasculature through the in-tact skull before (left), and after (right) the cranial window installation, once the skull has been removed. Scale bar: 1mm, blowup: 250μm. (b) Structural PAM image of the cortical vasculature on day 4 after the cranial window installation. Dashed circle: major hemorrhages in the brain. Scale bar: 1mm. (c) Visualization of Evans blue leakage 2 hours after dye injection (bottom) compared to baseline image before injection (top) at different timepoints after cranial window installation Scale bar: 1mm. (d) Evans blue coverage after date of initial cranial window installation.

6.3.2 Initial brain responses post window installation

After the installation of our cranial window, local hemorrhaging and inflammation usually occurs acutely during the first four days. On PAM images (day 4), the two circular regions demarcate the areas where hemorrhaging occur, which often completely occlude the vessels of interest (Fig. 6.2b). Despite the post-surgical care provided, the window quality typically worsens within the first week, and starts to recover at the start of week 2.

113

6.3.3 blood-brain barrier

To test for the integrity of the BBB, Evans blue was injected into the mouse, and structural PAM images were acquired and overlaid with the map of Evans blue leakage (Fig. 6.2c). Its coverage is plotted over time since the date of the cranial window installation (Fig. 6.2d). As shown in Fig. 6.2d, 23.2% Evans blue coverage was observed 2 hours after the injection, immediately after the baseline image was acquired after implantation. This is confirmed by the significant Evans blue extravasation visible in the structural PAM image on Day 0 (Fig. 6.2c). This leakage decreased to 15.2% on day 7, and diminished almost entirely to 2.6% on day 18 (Fig. 6.2d). Moreover, evident in the PAM images, the presence of the dye is almost entirely undetectable by Day 18 (Fig. 6.2c).

6.3.4 Longitudinal monitoring

The present cranial window protocol demonstrates high-quality, cortex-wide, functional PAM imaging for at least 24 weeks. As can be observed in Fig. 6.3a, PAM and microscopic images all exhibit consistent qualitative results throughout the monitoring period. Furthermore, signs of dura thickening or bone regrowth were not observed to interfere with our longitudinal monitoring, contrary to prior window preparations[20,22]. After performing vessel segmentation analysis as outlined in a prior publication of our group[25,26], we report that the functional parameters of vessel diameter, C_{Hb}, sO_2, and flow speed show no significant changes at any time point throughout the 24 week-span relative to the baseline at week 2 (Fig. 6.3b-e). This hemodynamic stability in our monitoring period demonstrates the robustness of our cranial window preparation and its reliability in other potential longitudinal applications.
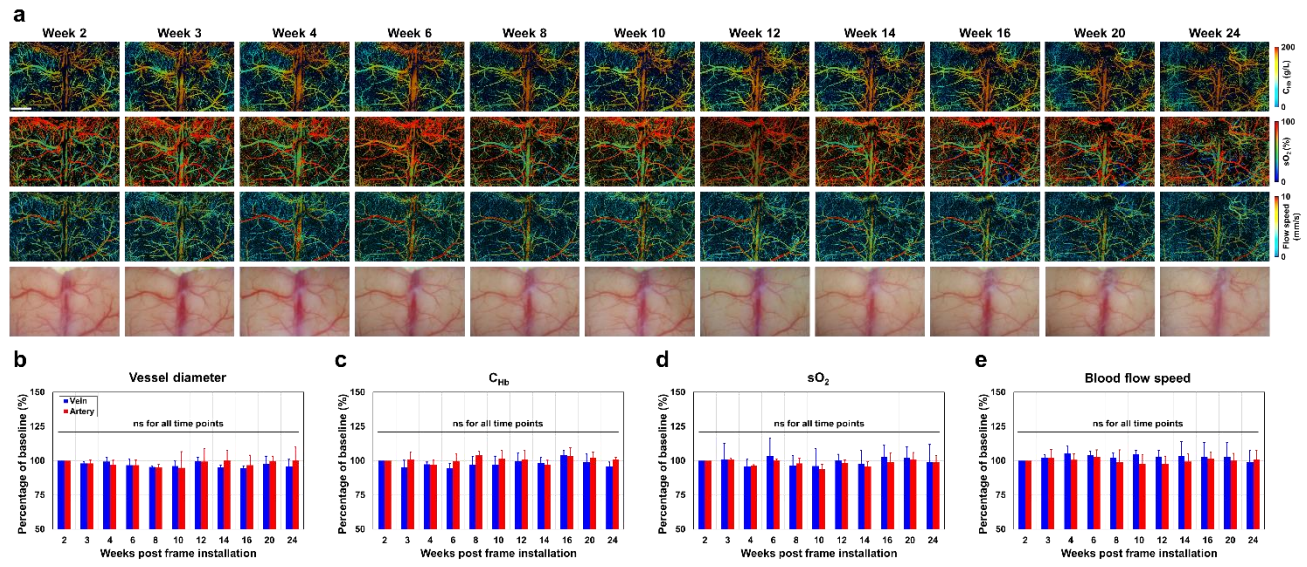
Fig. 6.3. (a) Longitudinal imaging of the awake mouse brain through a cranial window by multi-parametric PAM (Row 1–3) and a dissecting microscope (Row 4). Scale bar: 1 mm. (b-e) Segmentation-based quantitative analysis shows unchanged vascular structure and function over the prolonged monitoring period.

6.3.5 Awake *vs* anesthesia

The development of the present protocol also allowed us to further verify the reliability of our cranial window by repeating the work by Cao et al. on the effect of anesthesia on cerebral hemodynamics of the mouse brain. Following the protocol described by Cao et al.[25], we obtained PAM images in both the awake and anesthetized conditions for a comparative study. As can be observed in Fig. 6.4a, the anesthetized condition showed a marked increase in red color in both the sO_2 and flow speed maps, which implies an increase in both parameters. Results show that the administration of isoflurane increases arterial diameter by 25.7% and flow speed by 78.7%, and it also increases venous diameter, sO_2, and

flow speed by 8.4%, 17.6%, and 16.5% respectively (Fig. 6.4b-d). Overall, the application of isoflurane leads to a 47.1% decrease in the $CMRO_2$ (Fig. 6.4e). The trends that we observed in the present study are completely identical to the work by Cao et al., which further demonstrates the useful applications of our cranial window preparation.
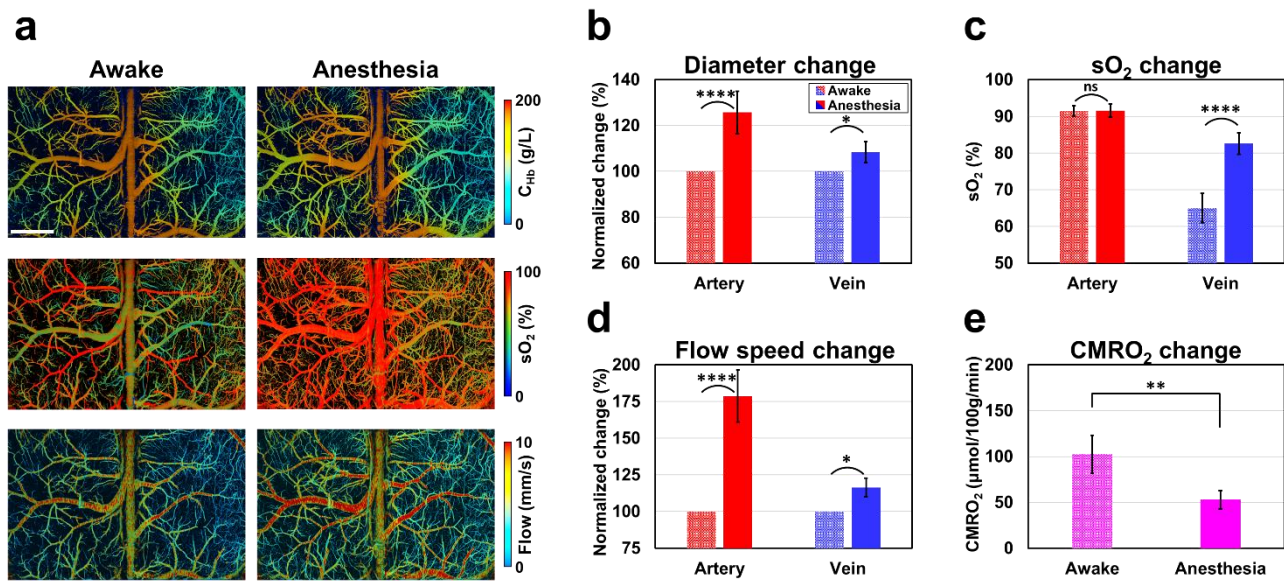
Fig. 6.4. Qualitative and quantitative comparisons between mouse cortex imaged at awake and anesthetized conditions. (a) PAM images of awake (left) and anesthetized (right) mouse cortical vasculature. Scale bar: 1 mm. (b-e) Statistical comparisons of key functional parameters in arteries and veins between awake and anesthetized mice (N = 5).

6.3.6 Photothrombosis

As shown in Fig. 6.5a, a focal ischemic region is visible 3 hours after the Rose Bengal injection and subsequent laser illumination in the ipsilateral cerebral hemisphere of the animal brain. TTC results and analysis confirm that ischemia is successfully induced in the right cerebral hemisphere (Fig. 6.5f).

Through PAM imaging, microvessel density, OEF, CBF, and $CMRO_2$ change are all quantified in all timepoints, from 3 hours to 28 days post-stroke, in both the contralateral and ipsilateral regions of the brain. The absolute values in these parameters at baseline do not show any significant differences between the stroke and the contralateral region. In the contralateral hemisphere, all four parameters remained unchanged throughout the study (Fig. 6.5b-e). However, by the end of the subacute phase (3 hours to 4 days post stroke), the ischemic hemisphere exhibited a significant 16.7% decrease in microvessel density change, 92.6% increase in OEF, 34.4% decrease in CBF, and 22.8% increase in $CMRO_2$ compared to the measurements.

By the end of the chronic phase (7-28 days), microvessel density change in the ipsilateral hemisphere gradually increased to 115.4%, which was found to be significantly larger than both its own ipsilateral baseline value and the day 28 value in the unaffected contralateral hemisphere (Fig. 6.5b). Meanwhile, ipsilateral CBF returned to its baseline level (Fig. 6.5d). However, by day 28, OEF levels in the stroke hemisphere declined to 59.2%, which is significantly lower than its normalized baseline value (Fig. 6.5c). Similarly, ipsilateral $CMRO_2$ declined significantly to 63.5% of its baseline by the end of the chronic phase (Fig. 6.5e). Furthermore, on day 28, significant $CMRO_2$ measurement in the ipsilateral region is 35.5% lower than in the contralateral region. Similarly, significant OEF measurement in the ipsilateral region is 44.5% lower than in the contralateral region. (Fig. 6.5c and e).
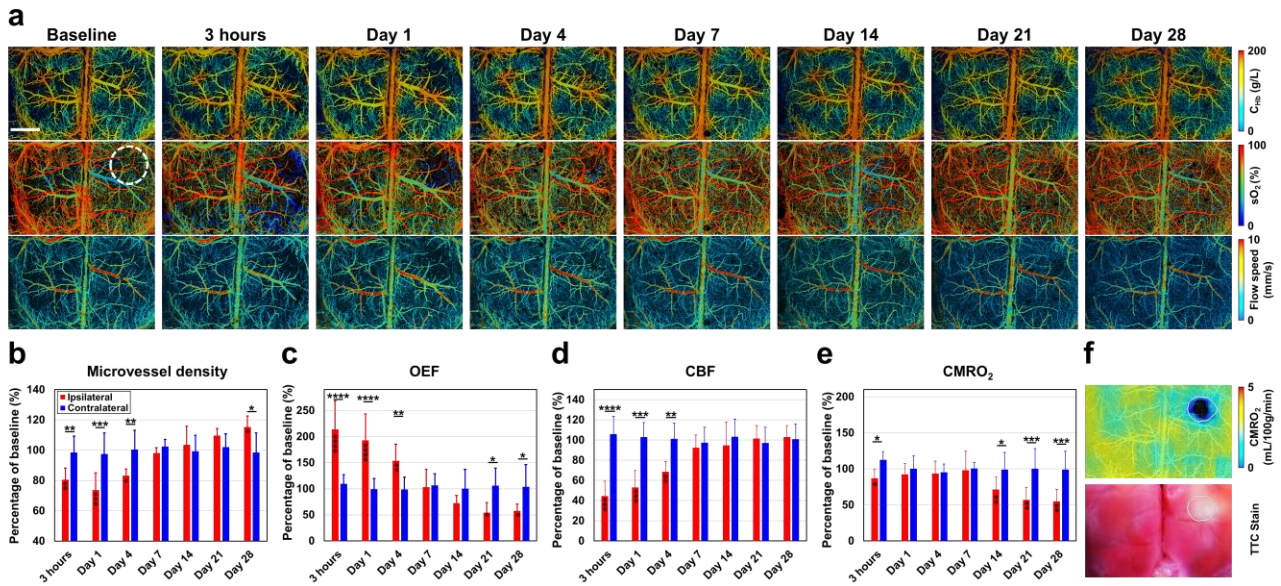
Fig. 6.5. (a) Longitudinal PAM of cerebrovascular responses to photothrombotic stroke. Dashed circle: focal ischemic region. Scale bar: 1 mm. (b-e) Quantitative analysis of structural and functional vascular remodeling and associated metabolic changes in response to stroke injury and recovery. (f) Co-registered PAM and TTC images show a correlation between reduced CMRO2 and tissue infarction.

6.4 Discussion

In the intact skull *vs* cranial window study, the vasculature at the superior sagittal sinus was not visible when imaged under the intact skull (Fig. 6.2a). This can be attributed to the shape of the cerebral cortex. The superior sagittal sinus is naturally depressed relative to the surrounding cortical tissue, which brings out-of-focus issues for cortex-wide PAM imaging. Although our system allows the contour scan of the entire cortex, the increased thickness of the skull at the superior sagittal sinus brings further scattering complications that resulted in the ultimate loss of signal in the region. Therefore, leaving the

skull intact is not suitable for cortex-wide PAM imaging. Not only is the usage limited by the age and size of the animal model[4], but there is also the tradeoff that has to be made between penetration depth and spatial resolution[16,17].

In our studies, we decided to exclude images taken in the first 2 weeks post window installation due to several reasons. First, we observed that there is acute local hemorrhaging that occurs in the cortex in the first 2 weeks. The bleeding often obstructed the vessels of interest and prevented us from PAM imaging. The amount of bleeding can be variant based on the quality of the surgery, and better preparations are observed to have the least amount of hemorrhaging and a more expedited recovery period. This variability across mice in bleeding and recovery time in the first 2 weeks reduce the repeatability for statistical analysis. Additionally, in the first 2 weeks post open-skull cranial windows, other adverse effects have been observed as well, including inflammation and BBB compromise[20,27,28], astrocyte and microglia activation[29], and loss of dendritic spines in neurons[30]. Moreover, in awake mouse imaging, it is necessary to conduct several mouse training sessions on the imaging treadmill to minimize stress levels during imaging sessions. The combination of these factors makes it a logical choice to exclude the first 2 weeks in our analysis.

In our longitudinal monitoring study, we have demonstrated to-date the longest monitoring period with stable hemodynamic parameters and without degradation in the imaging quality or need for window replacement. We attribute the longevity of the window to several key components used during surgical preparation to address both dura thickening and bone regrowth. Dura thickening is caused by a lack of pressure from the cranial window[22]. Accordingly, by taking advantage of the gelatin texture of agarose,

we were able to apply more pressure on the dura underneath the window to prevent thickening. To address

bone regrowth, we applied epoxy resin along the edge of the remaining skull, which proved to be effective.

In a previous cranial window study utilizing a skull-clearing window technique, which measured

BBB integrity, similarly, the mouse BBB experienced Evans blue extravasation[31]. However, few studies

have reported longitudinal experiments measuring BBB permeability over time following a cranial

window installation. In our study, by day 18, Evans blue coverage decreased to just 2.6%, which

demonstrates the gradual restoration of the BBB integrity[32]. This addresses the concern of a compromised

BBB following the installation of the cortex-wide cranial window and further validates the procedure as

a viable method for functional imaging of the mouse brain without causing major BBB leakage. Since

our data shows that BBB integrity is 95.2% restored by day 14, it suggests the necessity to allow, at least

two weeks post-surgery for the animal to adequately recover, before further experimentation.

Furthermore, in contrast with our current simultaneous bilateral photothrombotic comparison,

previous studies have only been able to demonstrate these results in separate control and stroke groups

of mice[33,34]. The multi-parametric PAM results from our photothrombosis experiment confirm that

through this cranial window procedure, it is possible to successfully conduct a bilateral cerebrovascular

stroke study, within one test subject, where the contralateral hemisphere is retained at baseline, while

focal ischemic stroke can be induced in the ipsilateral hemisphere, and monitored for significant changes

in microvessel density, $CMRO_2$, OEF, and CBF over the span of 28 days. In our study, a significant

difference in all measured cerebral hemodynamics is indeed observed between the ipsilateral and

contralateral hemispheres in the subacute phase after the induced ischemia. In a previous study, declining

trends in flow cross-sectional area (FCA) and vessel area density (VAD) were similarly reported in the subacute phase[34]. $CMRO_2$ is also known to decrease within an ischemic region, while OEF increases[35]. Moreover, in the chronic phase, CBF levels in the ipsilateral region are restored to baseline, indicated by the non-significant difference between CBF between to two hemispheres. These results are consistent with previous studies that show FCA is able to successfully recover from ischemic stroke, in part due to neuroprotective mechanisms and the central nervous system's recruitment of the leukocytes and astrocytes to the infarct region[12,33,34]. Furthermore, previous studies suggest that the plasticity of the brain during stroke recovery is due to cortical remapping of the stroke region with the surrounding ischemic tissue[36]. In the structural PAM images of the longitudinal monitoring following photothrombotic stroke, new vessel formations appear in the stroke region, which may indicate vascular remodeling during stroke recovery[37]. This is confirmed by our results which demonstrate significantly increased microvessel density by the end of the chronic stage from baseline. Previous studies have also found a similar upward trend by week 2[34,38,39]. Additionally, these results may be attributed to angiogenesis, which may largely contribute to stroke recovery, and suggested to be triggered by several influences, such as neuroblast migration to the infarct endothelial cells or by other neurotrophic factors[38-40].

Interestingly, in the chronic phase following the ischemic event, a full recovery to baseline is clearly exhibited in CBF, however, microvessel density, OEF and $CMRO_2$ do not show such a recovery, which echoes the results in the Lin and Powers study[41]. Lack of recovery in OEF and $CMRO_2$ is also consistent with the TTC results taken after day 28, which show that the ipsilateral infarct region of the cortex indeed remains distinctively paler than the rest of the brain.

This cranial window procedure which enables cortex-wide imaging of the awake mouse brain using PAM microscopy has many potential future applications to explore other chronic neurological disease models such as the longitudinal progression of Aβ plaque development in Alzheimer's Disease or perhaps the neurological basis for hemoglobinopathies[42,43]. In conjunction with this cranial window technique, by considering TPM with the PAM system, one can capitalize on both optical absorbance and fluorescence to conduct studies at the cellular level[44]. TPM can also be valuable in improving the imaging depth resolution[44]. And because of the large bilateral area and extensive 24-week longevity of the window frame, there are potential applications for neurovascular monitoring in mouse models at a new higher capacity.

Regarding the cortex-wide cranial window technique itself, modification of the window post-surgery as needed, in the form of additional dental dement reinforcement or total replacement of the frame, may enhance its lifetime even further[23]. Moreover, removal of the dura during surgery could be practiced to prevent dura and tissue regrowth, which may help prolong the clarity of the cortex over time.

Although high-resolution characterization of the cerebral hemodynamics in the awake mice brain was utilized to measure numerous parameters such as sO_2, $CMRO_2$, OEF, CBF, vessel diameter, microvessel density, and flow speed, there should be further optimization of the focused contour scanning system. Abnormally low sO_2 levels in the functional PAM images are due to the out-of-focus detection of the surface contours in the major cortical blood vessels, such as the superior sagittal sinus[45]. Correction of the PAM contour scanning can lead to more accurate sO_2 mapping of these major vessels, especially in relation to its more distal daughter vessels.

6.5 Conclusion

In the present study, we have developed a long-lifetime, cortex-wide, and light-weight cranial window suitable for functional and metabolic PAM imaging in the awake mouse brain. Longitudinal monitoring showed good window quality with unaffected cerebral hemodynamics (including C_{Hb}, sO_2, and blood flow speed) over 24 weeks without noticeable bone regrowth or dura thickening. The utility of the cranial window has been tested in three different experimental settings. Side-by-side comparison of the cerebral hemodynamics under awake and anesthetic conditions shows its utility for awake-brain imaging. Monitoring the hemodynamic and metabolic responses of the mouse brain to photothrombotic stroke throughout the recovery process shows its utility for longitudinal studies. Characterizing the Evans blue extravasation following the window implantation shows the restoration of BBB integrity after 14 days. Together, these results demonstrate that the cranial window technique we have developed enables high-resolution functional and metabolic PAM of the awake mouse brain over a prolonged period (>24 weeks), thereby opening new opportunities to study small-vessel pathology in a broad range of brain disorders.

Reference

[1]   Bi, R., Ma, Q., Mo, H., Olivo, M. & Pu, Y. in *Neurophotonics and Biomedical Spectroscopy* (eds Robert R. Alfano & Lingyan Shi)   159-187 (Elsevier, 2019).

[2]   Upputuri, P. K., Periyasamy, V., Kalva, S. K. & Pramanik, M. A High-performance Compact Photoacoustic Tomography System for In Vivo Small-animal Brain Imaging. *Journal of visualized experiments : JoVE* (2017).

[3]   Gamelin, J. *et al.* A real-time photoacoustic tomography system for small animals. *Optics express* **17**, 10489-10498 (2009).

[4]   Yao, J. *et al.* High-speed label-free functional photoacoustic microscopy of mouse brain in action. *Nature Methods* **12**, 407-410 (2015).

[5]   Yang, X. & Wang, L. V. Monkey brain cortex imaging by photoacoustic tomography. *Journal of biomedical optics* **13**, 044009 (2008).

[6]   Yao, J. & Wang, L. V. Photoacoustic Brain Imaging: from Microscopic to Macroscopic Scales. *Neurophotonics* **1** (2014).

[7]   Wang, L. V. & Hu, S. Photoacoustic Tomography: In Vivo Imaging from Organelles to Organs. *Science* **335**, 1458-1462 (2012).

[8]   Li, C. *et al.* Real-time photoacoustic tomography of cortical hemodynamics in small animals. *Journal of biomedical optics* **15**, 010509 (2010).

[9]   Kang, J. *et al.* Transcranial Recording of Electrophysiological Neural Activity in the Rodent Brain in vivo Using Functional Photoacoustic Imaging of Near-Infrared Voltage-Sensitive Dye. *Frontiers in Neuroscience* **13** (2019).

[10]   Xia, J. *et al.* Whole-body ring-shaped confocal photoacoustic computed tomography of small animals in vivo. *Journal of biomedical optics* **17**, 050506 (2012).

[11]   Hu, S. Listening to the Brain With Photoacoustics. *IEEE Journal of Selected Topics in Quantum Electronics* **22**, 117-126 (2016).

[12]   Cao, R. *et al.* Photoacoustic microscopy reveals the hemodynamic basis of sphingosine 1-phosphate-induced neuroprotection against ischemic stroke. *Theranostics* **8**, 6111-6120 (2018).

[13]   Liao, L. D., Li, M. L., Lai, H. Y., Chen, Y. Y. & Thakor, N. V. Study of neurovascular coupling functions for transient focal cerebral ischemia in rats using electrocorticography functional photoacoustic microscopy (ECoG-fPAM). *Conference proceedings : ... Annual International Conference of the IEEE Engineering in Medicine and Biology Society. IEEE Engineering in Medicine and Biology Society. Annual Conference* **2013**, 1799-1802 (2013).

[14]   Park, S.-J. *et al.* Visualizing Alzheimer's Disease Mouse Brain with Multispectral Optoacoustic Tomography using a Fluorescent probe, CDnir7. *Scientific Reports* **9**, 12052 (2019).

[15]   Mehrmohammadi, M., Yoon, S. J., Yeager, D. & Emelianov, S. Y. Photoacoustic Imaging for Cancer Detection and Staging. *Curr Mol Imaging* **2**, 89-105 (2013).

[16]   Silasi, G., Xiao, D., Vanni, M. P., Chen, A. C. & Murphy, T. H. Intact skull chronic windows for mesoscopic wide-field imaging in awake mice. *Journal of neuroscience methods* **267**, 141-149 (2016).

[17] Stein, E. W., Maslov, K. & Wang, L. V. Noninvasive, in vivo imaging of blood-oxygenation dynamics within the mouse brain using photoacoustic microscopy. *Journal of biomedical optics* **14**, 020502-020502 (2009).

[18] Zhao, Y.-J. *et al.* Skull optical clearing window for in vivo imaging of the mouse cortex at synaptic resolution. *Light: Science & Applications* **7**, 17153-17153 (2018).

[19] Yang, G., Pan, F., Parkhurst, C. N., Grutzendler, J. & Gan, W. B. Thinned-skull cranial window technique for long-term imaging of the cortex in live mice. *Nature protocols* **5**, 201-208 (2010).

[20] Holtmaat, A. *et al.* Long-term, high-resolution imaging in the mouse neocortex through a chronic cranial window. *Nature protocols* **4**, 1128-1144 (2009).

[21] Li, H. *et al.* Disposable ultrasound-sensing chronic cranial window by soft nanoimprinting lithography. *Nature Communications* **10**, 4277 (2019).

[22] Goldey, G. J. *et al.* Removable cranial windows for long-term imaging in awake mice. *Nature protocols* **9**, 2515-2538 (2014).

[23] Heo, C. *et al.* A soft, transparent, freely accessible cranial window for chronic imaging and electrophysiology. *Sci Rep* **6**, 27818 (2016).

[24] Kim, T. H. *et al.* Long-Term Optical Access to an Estimated One Million Neurons in the Live Mouse Cortex. *Cell reports* **17**, 3385-3394 (2016).

[25] Cao, R. *et al.* Functional and oxygen-metabolic photoacoustic microscopy of the awake mouse brain. *NeuroImage* **150**, 77-87 (2017).

[26] Sun, N. *et al.* In vivo imaging of hemodynamic redistribution and arteriogenesis across microvascular network. *Microcirculation* **27**, e12598 (2020).

[27] Shih, A. Y. *et al.* Two-photon microscopy as a tool to study blood flow and neurovascular coupling in the rodent brain. *Journal of cerebral blood flow and metabolism : official journal of the International Society of Cerebral Blood Flow and Metabolism* **32**, 1277-1309 (2012).

[28] Cole, J. T. *et al.* Craniotomy: true sham for traumatic brain injury, or a sham of a sham? *Journal of neurotrauma* **28**, 359-369 (2011).

[29] Dorand, R. D., Barkauskas, D. S., Evans, T. A., Petrosiute, A. & Huang, A. Y. Comparison of intravital thinned skull and cranial window approaches to study CNS immunobiology in the mouse cortex. *Intravital* **3**, e29728 (2014).

[30] Xu, H.-T., Pan, F., Yang, G. & Gan, W.-B. Choice of cranial window type for in vivo imaging affects dendritic spine turnover in the cortex. *Nature Neuroscience* **10**, 549-551 (2007).

[31] Feng, W., Zhang, C., Yu, T., Semyachkina-Glushkovskaya, O. & Zhu, D. In vivo monitoring blood-brain barrier permeability using spectral imaging through optical clearing skull window. *Journal of biophotonics* **12**, e201800330 (2019).

[32] Zhang, C. *et al.* Photodynamic opening of the blood-brain barrier to high weight molecules and liposomes through an optical clearing skull window. *Biomedical optics express* **9**, 4850-4862 (2018).

[33] Schoknecht, K. *et al.* Monitoring stroke progression: in vivo imaging of cortical perfusion, blood-brain barrier permeability and cellular damage in the rat photothrombosis model. *Journal of cerebral blood flow and metabolism : official journal of the International Society of Cerebral Blood Flow and Metabolism* **34**, 1791-1801 (2014).

[34] Yang, S. *et al.* Longitudinal in vivo intrinsic optical imaging of cortical blood perfusion and tissue damage in focal photothrombosis stroke model. *Journal of cerebral blood flow and metabolism : official journal of the International Society of Cerebral Blood Flow and Metabolism* **39**, 1381-1393 (2019).

[35] Yamauchi, H., Fukuyama, H., Nagahama, Y., Nishizawa, S. & Konishi, J. Uncoupling of oxygen and glucose metabolism in persistent crossed cerebellar diaschisis. *Stroke* **30**, 1424-1428 (1999).

[36] Murphy, T. H. & Corbett, D. Plasticity during stroke recovery: from synapse to behaviour. *Nature reviews. Neuroscience* **10**, 861-872 (2009).

[37] Liu, J. *et al.* Vascular remodeling after ischemic stroke: mechanisms and therapeutic potentials. *Progress in neurobiology* **115**, 138-156 (2014).

[38] Chopp, M., Zhang, Z. G. & Jiang, Q. Neurogenesis, angiogenesis, and MRI indices of functional recovery from stroke. *Stroke* **38**, 827-831 (2007).

[39] Thored, P. *et al.* Long-term neuroblast migration along blood vessels in an area with transient angiogenesis and increased vascularization after stroke. *Stroke* **38**, 3032-3039 (2007).

[40] Font, M. A., Arboix, A. & Krupinski, J. Angiogenesis, neurogenesis and neuroplasticity in ischemic stroke. *Curr Cardiol Rev* **6**, 238-244 (2010).

[41] Lin, W. & Powers, W. J. Oxygen metabolism in acute ischemic stroke. *Journal of cerebral blood flow and metabolism : official journal of the International Society of Cerebral Blood Flow and Metabolism* **38**, 1481-1499 (2018).

[42] Hu, S., Yan, P., Maslov, K., Lee, J. M. & Wang, L. V. Intravital imaging of amyloid plaques in a transgenic mouse model using optical-resolution photoacoustic microscopy. *Opt Lett* **34**, 3899-3901 (2009).

[43] Golan, L., Yeheskely-Hayon, D., Minai, L., Dann, E. J. & Yelin, D. Noninvasive imaging of flowing blood cells using label-free spectrally encoded flow cytometry. *Biomedical optics express* **3**, 1455-1464 (2012).

[44] Song, W. *et al.* Fully integrated reflection-mode photoacoustic, two-photon, and second harmonic generation microscopy in vivo. *Sci Rep* **6**, 32240 (2016).

[45] Zhiqiang, X. *et al.* Cortex-wide multiparametric photoacoustic microscopy based on real-time contour scanning. *Neurophotonics* **6**, 1-8 (2019).

Chapter 7 Photoacoustic microscopy of metabolic dysfunction in neonatal hypoxic-ischemic encephalopathy

7.1 Introduction

Neonatal HIE occurs in ~3 per 1,000 live births in the USA (and a higher incidence in developing countries), with potential devastating sequelae including cerebral palsy, epilepsy, and cognitive impairment[1-3]. Preclinical research shows that acute HI insult causes an initial depression of brain energetics, which quickly recovers and maintains for a variable period (a latent phase) until it plummets again as "secondary energy failure" that signifies irreversible brain injury[4]. Developing novel imaging biomarkers of "secondary energy failure" can be used in early detection of brain injury and outcome prognostication to improve neonatal care[5,6]. However, developing non-invasive bedside procedures to monitor brain damage is still a major challenge in neonatology. Although MRI/MRS are powerful diagnostic tools for HIE, unlikely they will become a bedside procedure to closely monitor the progression of HI brain injury[7,8]. In contrast, an index for cerebral oxygen metabolism ($CMRO_{2i}$) measured by FDNIRS/DCS is a promising alternative[9-12], since $CMRO_2$ is a reliable marker of tissue viability in adult stroke[13,14]. However, due to constraints in human research, it remains uncertain whether a plunge of $CMRO_2$ after birth asphyxia signifies energy failure plus irreversible brain damage and what triggers the rapid decline of $CMRO_2$ in HIE.

With the great potential to address the current challenges of $CMRO_2$ quantification, the multi-parameter PAM will be utilized for $CMRO_2$ measurement to monitor the viability at the tissue level in experiment HIE[15-17]. By demonstration the simultaneously measurement of C_{Hb}, sO_2, and blood flow

speed—all the hemodynamic parameters required for quantification of $CMRO_2$ and the extrapolation algorithm described in Chapter 2, the multi-parameter PAM is an ideal imaging tool to study the HIE model *in vivo*. To avoid the confounding effect of anesthesia on the $CMRO_2$ responses to hypoxia and HI, reduce individual variations, and simplified repeated PAM imaging on the same animal, the awake mouse brain is necessary[17].

In this chapter, we first extended our previously developed head-restrained PAM from adult mice to P10 mice, enabling awake and cortex-wide contour imaging, and validated it with global hypoxia experiment. Then, the Vannucci HI model was used to mimic the HIE condition in neonatal mice, and the hemodynamic parameters were acquired by PAM to calculate $CMRO_2$ for the comparison of the contralateral and ipsilateral side. At last, the effectiveness of therapeutic hypothermia of HIE was examined after the hypothermia treatment, with the comparison of normothermia treatment group.

7.2 Results and Discussion

7.2.1 System development

Based on our previous work[17,18], we have demonstrated the capability of awake mouse brain imaging with the cortex-wide contour scanning, to avoid the effect of anesthesia as well as the out-of-focus issue, which could image the ipsilateral and contralateral hemisphere simultaneously. Also, we designed a 3-D printed head-mounted frame for the neonatal mouse brain, which could secure its head to the image platform in Chapter 6. By the combination of these updates, the updated imaging platform for neonatal mouse brain imaging was developed as shown in Fig. 7.1. The syringe mask and tube of normoxia or hypoxia, could help us to control the inhalation gas.
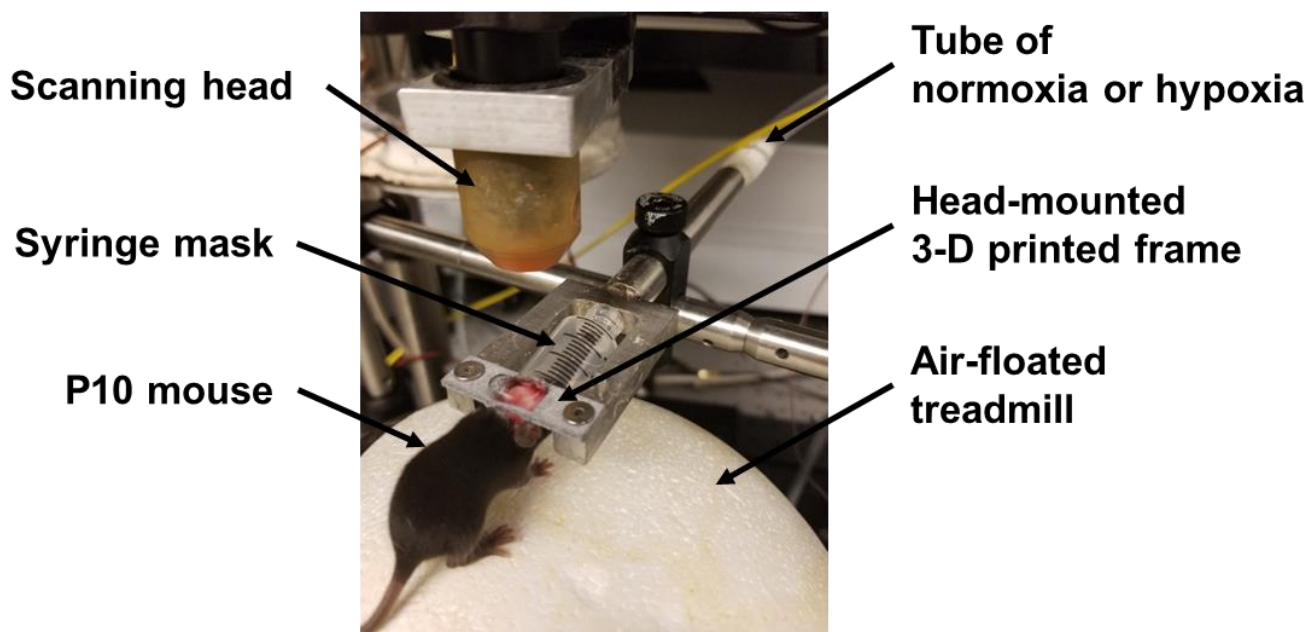
Fig. 7.1. Neonatal mouse brain imaging platform.

7.2.2 Hemodynamic response to hypoxia of P10 mice

In this section, we first used the normoxia condition, which is 21% oxygen. Then we use hypoxia condition by mixing oxygen and nitrogen to obtain the gas with 10% oxygen during the scanning. The PAM images of sO_2 and flow speed, as well as the statistical results are shown in Fig. 7.2. As expected, hypoxia caused a reduction of sO_2, but OEF had a compensatory increase. Also, with the vasodilation, the CBF also increased, leading to a $p<0.05$ increase in $CMRO_2$ (Fig. 7.2, n=5). While our observation of "hypoxia increases $CMRO_2$" is a bit counterintuitive, it is consistent with the MRI-based results of the metabolic response to 10-14% oxygen by adult human subjects[19,20].
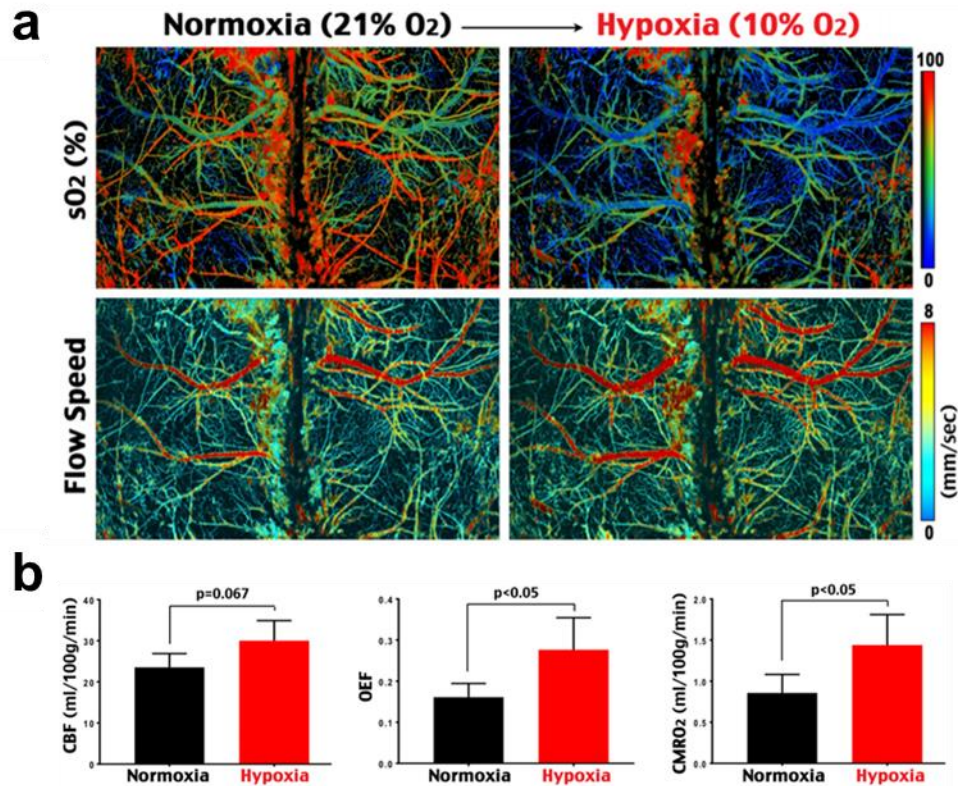
Fig. 7.2. (a) sO_2 and flow speed under 20.9%-vs-10% O_2. (b) PAM-derived CBF, OEF, and $CMRO_2$.

7.2.3 $CMRO_2$ response to the Vannucci HI

Next, we used the PAM-based awake-brain imaging to compare the responses to Vannucci HI (unilateral carotid artery occlusion plus 40-min hypoxia) in both hemispheres in P10 mice. Specifically, we used time-lapse PAM imaging to track the changes of CBF, OEF, and $CMRO_2$ in both hemispheres before, during, and after the hypoxia insult (0-40, 40-80, and 80-120 min) in the same animal (Fig. 7.3, n=4). This experiment showed increased $CMRO_2$ in the contralateral hemisphere (blue circle in Fig. 7.3c). However, the ipsilateral hemisphere showed a reduction of $CMRO_2$ during the hypoxia period, followed by a significant surge and overshoot of $CMRO_2$ in the post-HI period (red squares in Fig 7.3c). Close

examination indicated that the responses to HI on the contralateral hemisphere were similar to those in response to global hypoxia (large increase of both CBF and OEF, Fig. 7.3b). In contrast, CBF barely increased on ipsilateral hemisphere during HI (likely due to the carotid artery occlusion and hypoxia-induced peripheral vasodilation) and OEF actually decreased transiently (Fig. 7.3b). Moreover, there was a sustained increase of $CMRO_2$ values for up to 2 hours after HI in the ipsilateral hemisphere (Fig. 7.3c), which may reflect increased mitochondrial oxidative phosphorylation that could trigger reperfusion-induced oxidative outburst (Fig. 7.3c).
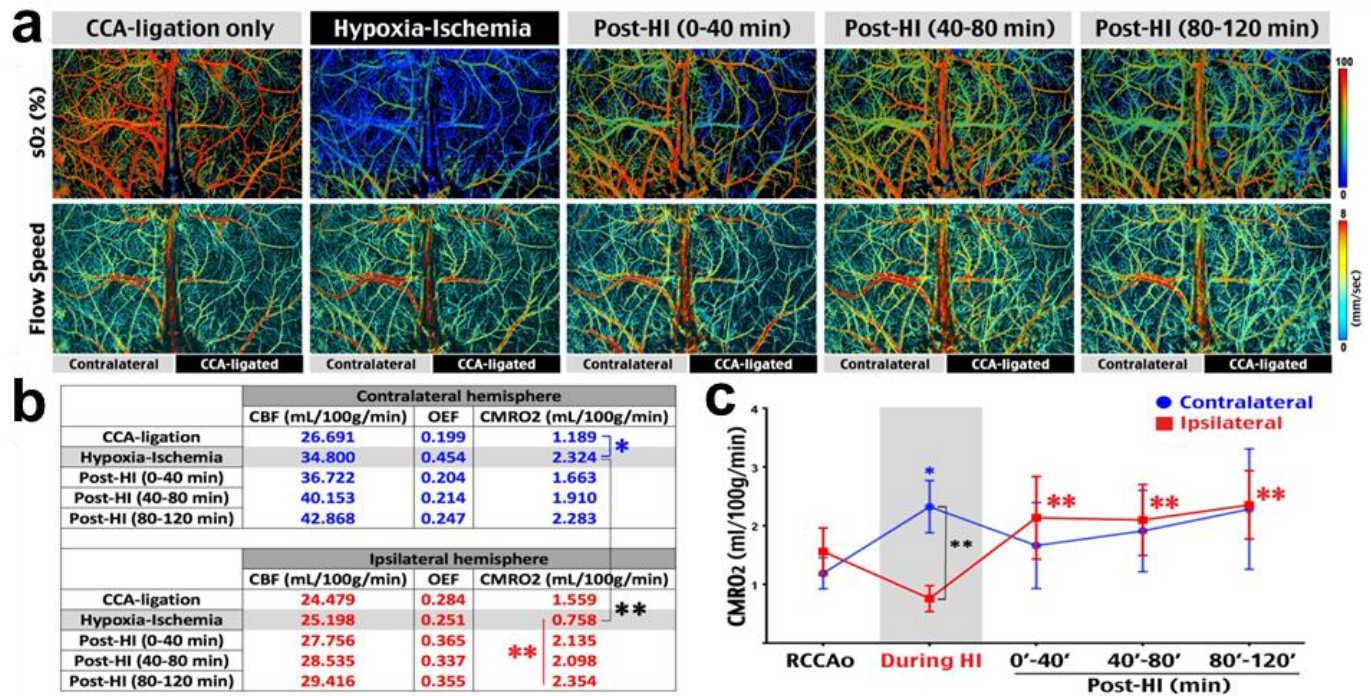
Fig. 7.3. Combined HI causes $CMRO_2$-suppression and a rapid recovery in the ipsilateral hemisphere in P10 mice. (a) Sequential sO_2 and flow speed images of the indicated phases. (b) Quantification of CBF, OEF, and $CMRO_2$ (n=4). *: $p<0.05$ and ** $p<0.01$ for the indicated comparison by t-test. (c) Tracing of the different $CMRO_2$ responses to HI in ipsilateral-versus-contralateral hemispheres.

7.2.4 Post-HI mitochondrial hyperactivity

Since mitochondria is the primary site of oxygen consumption and source for $CMRO_2$, we conjectured that there may be post-HI mitochondrial hyperactivity to account for the post-HI $CMRO_2$ overshoot (Fig. 7.3c). To test this notion, we have visited Dr. Vadim Ten's laboratory to learn biochemical and physiological analytic methods with isolated mitochondria, and used them to compare the mitonchondria activity at 2 and 5 h after Vannucci HI in P10 mice (Fig. 7.4). This analysis indicated the oxygen consumption rate (OCR) by isolated mitochondria from the ipsilateral hemisphere was significantly greater than those from contralateral hemisphere or unchallenged mice at 2 h, but reduced at 5 h post-HI (Fig. 7.4a&b, n=3-4). Moreover, the mitochondria from ipsilateral hemisphere showed increased succinate-induced H_2O_2 production but near-normal membrane potential at 2 h post-HI, suggesting that they remain viable at this timepoint (Fig.7.4 c&d). In contrast, at 5 h post-HI, the mitochondria from ipsilateral hemisphere showed reduced membrane potential and succinate-induced H_2O_2 release, plus diminished OCR, suggesting that they were no longer healthy. These results suggest
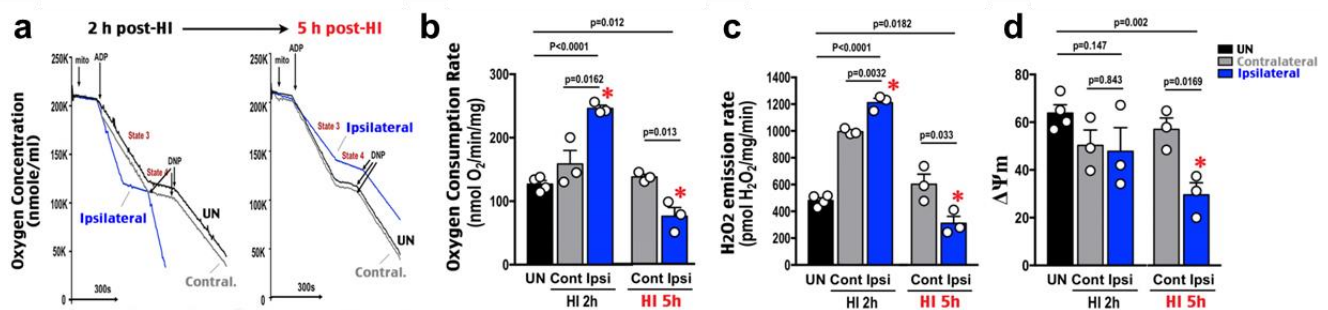
Fig. 7.4. Comparison of the mitochondria activity and integrity at 2-versus-5 h post-HI. p-value is determined by t-test. n=3-4 as indicated.

that the post-HI overshoot of $CMRO_2$ is correlated with, or caused by post-HI mitochondrial hyperactivity.

7.2.5 Effectiveness of the therapeutic hypothermia of HIE.

It has been reported that cooling/hypothermia preserves the mitochondrial functions in myocardial ischemia[21]. Hence, we will test whether hypothermia reduces post-HI mitochondrial hyperactivity and (consequently) the overshoot of $CMRO_2$, leading to better outcomes in murine neonates. In this section, we used the head-restrained PAM system to compare $CMRO_2$ and TTC stain (the gold standard to detect cerebral infarct by the lack of TTC/red-staining) in awake P11 (i.e., eleven days after birth) mice at 24 h
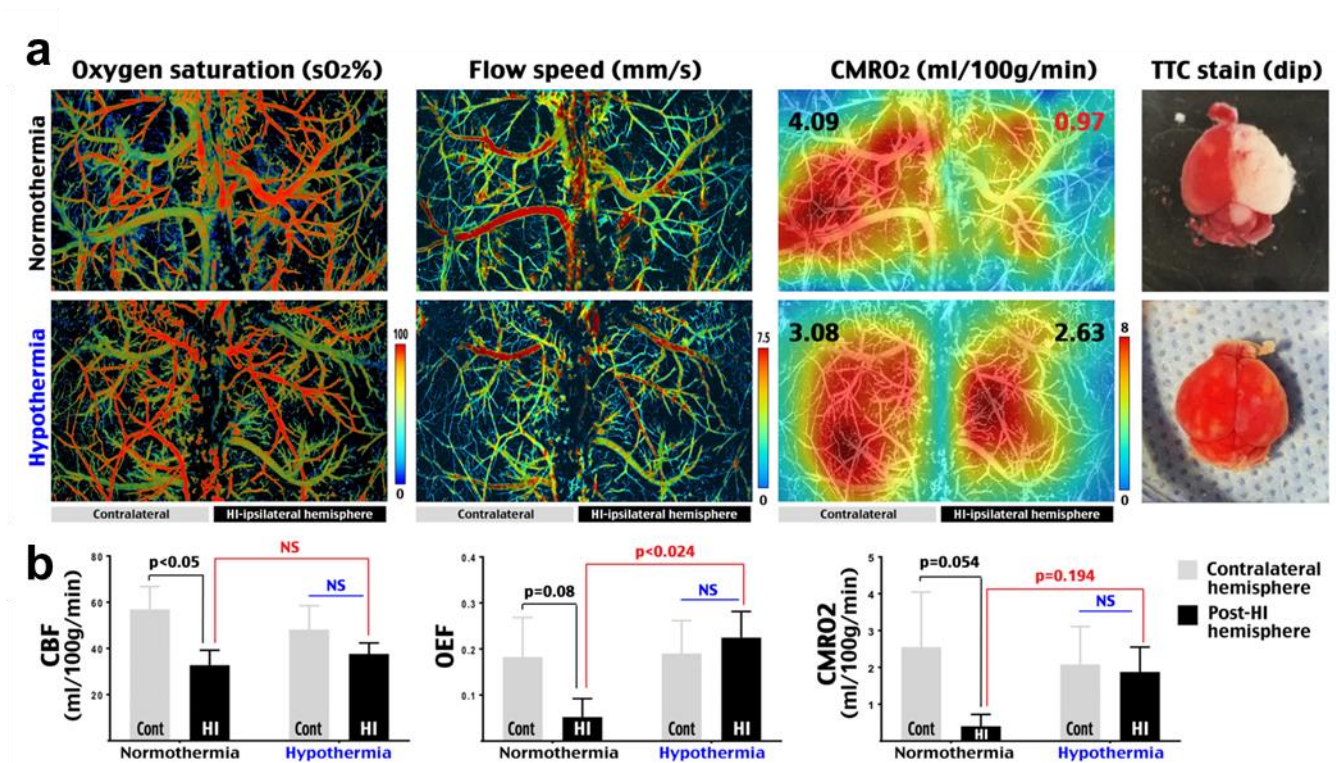
Fig. 7.5. (a) Correlation of TTC-defined infarction and severe $CMRO_2$ reduction in awake mice at 24 h post-HI. The $CMRO_2$ values in the normothermia-vs-hypothermia treated mouse hemispheres were labeled. (B) Statistical analysis (n=3 for each).

133

post-HI and normothermia *vs* hypothermia treatment (for 4 h immediately after HI). This experiment revealed severe $CMRO_2$ reduction (0.97 ml/100g/min) coupled to impaired TTC staining right after the PAM scan in the ipsilateral hemisphere of normothermia-treated mouse (Fig. 7.5a, top row). In contrast, the hypothermia-treated animals showed a smaller reduction of $CMRO_2$ (2.63-*vs*-3.08 ml/100g/min) and stronger TTC stain in ipsilateral hemisphere (Fig. 7.5a, bottom row).

we tested whether hypothermia protects the mitochondrial integrity at 5 h post-HI (Fig. 7.6). P10 mice were subjected to Vannucci HI followed by recovery in a normothermic (37 °C)-versus-hypothermic (32 °C) environment for 4 hours. At 5 h post-HI, we collected the mitochondria from both hemispheres for *in vitro* analysis. This experiment indicated that post-HI hypothermia treatment successfully rescued the mitochondrial derangements in animals recovered in a normothermic environment (Fig. 7.6). Interestingly, the mitochondria from ipsilateral hemisphere showed increased superoxide at 5 h pos-HI, despite reduction of succinate-induced H_2O_2 release (Fig. 7.6b&c). This pattern suggests reverse electron transfer-induced ROS outburst during reperfusion. It also echoes Vadim Ten's thesis that mitochondrial complex I is an important source for oxidative insults in neonatal HIE[22,23].
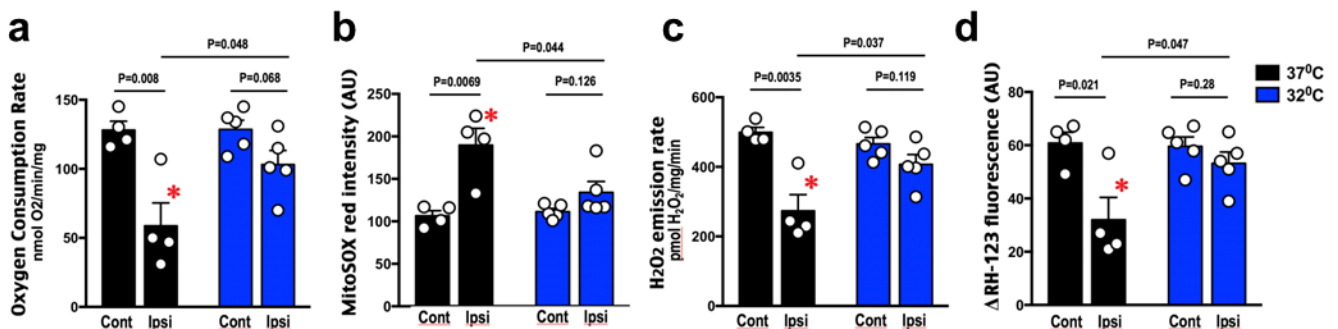
Fig. 7.6. Hypothermia protects against the rapid demise of mitochondria after experimental HIE in mice. p-value is determined by t-test.

7.3 Conclusion

In this study, we first developed a multi-parametric PAM platform for awake, cortex-wide head-restrained *in vivo* imaging of P10/P11 mice, and then evaluated with a global hypoxia experiment. The results showed that hypoxia increases $CMRO_2$, which is consistent with the MRI-based results of the metabolic response to 10-14% oxygen by adult human subjects. Then, we investigated HIE of the neonatal brain with the Vannucci HI model, which the PAM and biochemistry results showed a rapid drop of $CMRO_2$ during the HI with rapid recovery in the latent phase, and finally irreversible dropped again as the second energy failure. At last, we explored the effectiveness of therapeutic hypothermia, and the results showed that hypothermia reduced post-HI mitochondrial hyperactivity and (consequently) the overshoot of $CMRO_2$.

Reference

[1]   Hull, J. & Dodd, K. L. Falling incidence of hypoxic-ischaemic encephalopathy in term infants. *British journal of obstetrics and gynaecology* **99**, 386-391 (1992).

[2]   Thornberg, E., Thiringer, K., Odeback, A. & Milsom, I. Birth asphyxia: incidence, clinical course and outcome in a Swedish population. *Acta paediatrica (Oslo, Norway : 1992)* **84**, 927-932 (1995).

[3]   Wu, Y. W., Backstrand, K. H., Zhao, S., Fullerton, H. J. & Johnston, S. C. Declining Diagnosis of Birth Asphyxia in California: 1991–2000. *Pediatrics* **114**, 1584-1590 (2004).

[4]   Gunn, A. J. *et al.* Therapeutic hypothermia translates from ancient history in to practice. *Pediatr Res* **81**, 202-209 (2017).

[5]   Faulkner, S. *et al.* Xenon augmented hypothermia reduces early lactate/N-acetylaspartate and cell death in perinatal asphyxia. *Annals of neurology* **70**, 133-150 (2011).

[6]   Natarajan, N. & Pardo, A. C. Challenges in neurologic prognostication after neonatal brain injury. *Seminars in perinatology* **41**, 117-123 (2017).

[7]   Raichle, M. E. Behind the scenes of functional brain imaging: A historical and physiological perspective. *Proceedings of the National Academy of Sciences* **95**, 765-772 (1998).

[8]   Rodgers, Z. B., Detre, J. A. & Wehrli, F. W. MRI-based methods for quantification of the cerebral metabolic rate of oxygen. *Journal of cerebral blood flow and metabolism : official journal of the International Society of Cerebral Blood Flow and Metabolism* **36**, 1165-1185 (2016).

[9]   Rajaram, A. *et al.* Simultaneous monitoring of cerebral perfusion and cytochrome c oxidase by combining broadband near-infrared spectroscopy and diffuse correlation spectroscopy. *Biomedical optics express* **9**, 2588-2603 (2018).

[10]   Bale, G. *et al.* Oxygen dependency of mitochondrial metabolism indicates outcome of newborn brain injury. *Journal of cerebral blood flow and metabolism : official journal of the International Society of Cerebral Blood Flow and Metabolism* **39**, 2035-2047 (2019).

[11]   Jain, V. *et al.* Cerebral oxygen metabolism in neonates with congenital heart disease quantified by MRI and optics. *Journal of cerebral blood flow and metabolism : official journal of the International Society of Cerebral Blood Flow and Metabolism* **34**, 380-388 (2014).

[12]   Liu, P., Chalak, L. F. & Lu, H. Non-invasive assessment of neonatal brain oxygen metabolism: A review of newly available techniques. *Early Human Development* **90**, 695-701 (2014).

[13]   Dehaes, M. *et al.* Cerebral oxygen metabolism in neonatal hypoxic ischemic encephalopathy during and after therapeutic hypothermia. *Journal of cerebral blood flow and metabolism : official journal of the International Society of Cerebral Blood Flow and Metabolism* **34**, 87-94 (2014).

[14]   Ferradal, S. L. *et al.* Non-invasive Assessment of Cerebral Blood Flow and Oxygen Metabolism in Neonates during Hypothermic Cardiopulmonary Bypass: Feasibility and Clinical Implications. *Sci Rep* **7**, 44117 (2017).

[15]   Ning, B. *et al.* Simultaneous photoacoustic microscopy of microvascular anatomy, oxygen saturation, and blood flow. *Opt. Lett.* **40**, 910-913 (2015).

[16] Zhou, Y., Yao, J., Maslov, K. I. & Wang, L. V. Calibration-free absolute quantification of particle concentration by statistical analyses of photoacoustic signals in vivo. *Journal of biomedical optics* **19**, 37001 (2014).

[17] Cao, R. *et al.* Functional and oxygen-metabolic photoacoustic microscopy of the awake mouse brain. *NeuroImage* **150**, 77-87 (2017).

[18] Zhiqiang, X. *et al.* Cortex-wide multiparametric photoacoustic microscopy based on real-time contour scanning. *Neurophotonics* **6**, 1-8 (2019).

[19] Vestergaard, M. B. *et al.* Acute hypoxia increases the cerebral metabolic rate - a magnetic resonance imaging study. *Journal of cerebral blood flow and metabolism : official journal of the International Society of Cerebral Blood Flow and Metabolism* **36**, 1046-1058 (2016).

[20] Xu, F., Liu, P., Pascual, J. M., Xiao, G. & Lu, H. Effect of hypoxia and hyperoxia on cerebral blood flow, blood oxygenation, and oxidative metabolism. *Journal of cerebral blood flow and metabolism : official journal of the International Society of Cerebral Blood Flow and Metabolism* **32**, 1909-1918 (2012).

[21] Ning, X. H. *et al.* Hypothermia preserves function and signaling for mitochondrial biogenesis during subsequent ischemia. *The American journal of physiology* **274**, H786-793 (1998).

[22] Kim, M. *et al.* Attenuation of oxidative damage by targeting mitochondrial complex I in neonatal hypoxic-ischemic brain injury. *Free radical biology & medicine* **124**, 517-524 (2018).

[23] Ten, V. S. *et al.* Complement component c1q mediates mitochondria-driven oxidative stress in neonatal hypoxic-ischemic brain injury. *The Journal of neuroscience : the official journal of the Society for Neuroscience* **30**, 2077-2087 (2010).

Chapter 8 Conclusions and perspectives

8.1 Conclusion

In this dissertation, we developed a first-of-a-kind hardware-software multi-parametric PAM platform for conventional raster scanning (i.e., mouse ear), cortex-wide contour imaging (i.e., mouse brain), and intravital imaging (i.e., mouse kidney). Enabling the simultaneous quantification of three key hemodynamic parameters—C_{Hb}, sO_2 and blood flow speed—for quantifying oxygen metabolism, together with vessel segmentation algorithm and the extension algorithm of the current $MRO_2/CMRO_2$ measurement, this PAM platform could be finally used to study hemodynamic and oxygen-metabolic dysfunction in a wide range of disease models for multiple tissue/organ sites.

In Chapter 3, we studied the hemodynamic redistribution and arteriogenesis across microvascular network by inducing the ligation of feeding arteries in the mouse ear. A new, inverse relationship between initial vascular resistance and extent of arteriogenesis was revealed. What's more, the differential responses between obese and lean mice were also observed, that there is a stronger structural and functional remodeling in the lean mice and a more severe hypoxia right after ligation and an incomplete recovery of sO_2 21 days post ligation in the obese mice.

In Chapter 4, the longitudinal and comprehensive characterization of microvascular responses to AZD8601 was performed, *in vivo*. The result showed that intradermal injection of AZD8601 formulated in a biocompatible vehicle results in pronounced, sustained and dose-dependent vasodilation, blood flow upregulation, and neovessel formation, in striking contrast to those induced by recombinant human VEGF-A protein, a non-translatable variant of AZD8601, and citrate/saline vehicle. By using a mouse

model of diabetic wound healing *in vivo*, the results showed that sequential dosing of AZD8601 improves vascularization and tissue oxygenation of the wound bed, leading to accelerated re-epithelialization during the early phase of diabetic wound healing.

In Chapter 5, the intravital multi-parametric was used to monitor the hemodynamic changes of sO_2 and blood flow of the kidney microvasculature. The normoxia *vs* hypoxia experiment revealed a strong correlation between inhaled oxygen concentration and measured sO_2. Then, with LPS-induced AKI model, time dependent changes in hemodynamic parameters and kidney injury markers were monitored. The change of oxygen stress was associated with reduced kidney ATP levels in the early stages of LPS-induced AKI.

In Chapter 6, a first-of-a-kind long-lifetime (>5 months), cortex-wide (6×8 mm^2), and light-weight (<2 g) cranial window with dual transparency to both light and ultrasound was developed, whose lifetime is over 24 weeks without dura thickening and skull regrowth. Then, the photothrombosis model was used to study the chronic progression of brain diseases was demonstrated by monitoring the functional recovery of the mouse brain from ischemic stroke throughout the acute (<24 hours), subacute (1–5 days), and chronic (up to 4 weeks) stages of ischemic stroke. With this bilateral cerebrovascular stroke study, within one test subject, the contralateral hemisphere is retained at baseline, while focal ischemic stroke is induced in the ipsilateral hemisphere with significant changes in microvessel density, $CMRO_2$, OEF, and CBF over the span of 28 days.

In Chapter 7, the results of the global hypoxia among neonatal mice showed that hypoxia increases $CMRO_2$, which is consistent with the MRI-based results of the metabolic response to 10-14% oxygen by

adult human subjects. Besides, both of the PAM and biochemistry results of the Vannucci HI model showed a rapid drop of $CMRO_2$ during the HI with rapid recovery in the latent phase, with an irreversible dropped again as the second energy failure. Finally, the effectiveness of therapeutic hypothermia was confirmed with the reduced post-HI mitochondrial hyperactivity and the moderate $CMRO_2$ drop.

8.2 Perspectives

8.2.1 Puncture wound healing

Cutaneous wounds including puncture wounds, ulcers, and contusions, which caused by burn incidence or other incidences, affects over two million of the U.S. population each year[1]. Since skin is a rich vascularized tissue thus the anatomic characterization and the functional quantification of blood vessels have been tightly linked to wound healing[2,3]. Since multi-parametric PAM holds the great potential to map vasculatures and hemodynamics, we did several preliminary studies of the puncture wound model, with characterization of the wound healing process.

As Fig. 8.1 shown, we longitudinally monitored the puncture wound healing process from baseline to day 14 post the induction of wound, which covered the hemostasis phase, the inflammatory phase, almost entire proliferative phase, and even the very early maturation phase. Both of brightfield images (Fig. 8.1a) and PAM images (Fig. 8.1b) are presented, from which we could observe the wound healing process up to 14 days. Because of hemorrhage, the shape of the wound was irregular right after the onset of wound, but sO_2 and blood flow speed had a dramatic change due to the loss of ear tissue and blood. On day 1, the shape formed an almost round hole, reflecting the biopsy punch we used (Integra® Miltex®, Japan), and the height of wound edge also thickened because of the inflammation. For the later timepoints,

with the gradual closure of the wound, angiogenesis was observed in the surrounding area of the wound, implying the proliferative phase was ongoing. Which is more interesting are the tissue level maps of MRO_2, OEF and volumetric flow. The increased MRO_2 value implied that an increased demand of tissue recovery and vasculature reconstruction for oxygen, or, the energy.
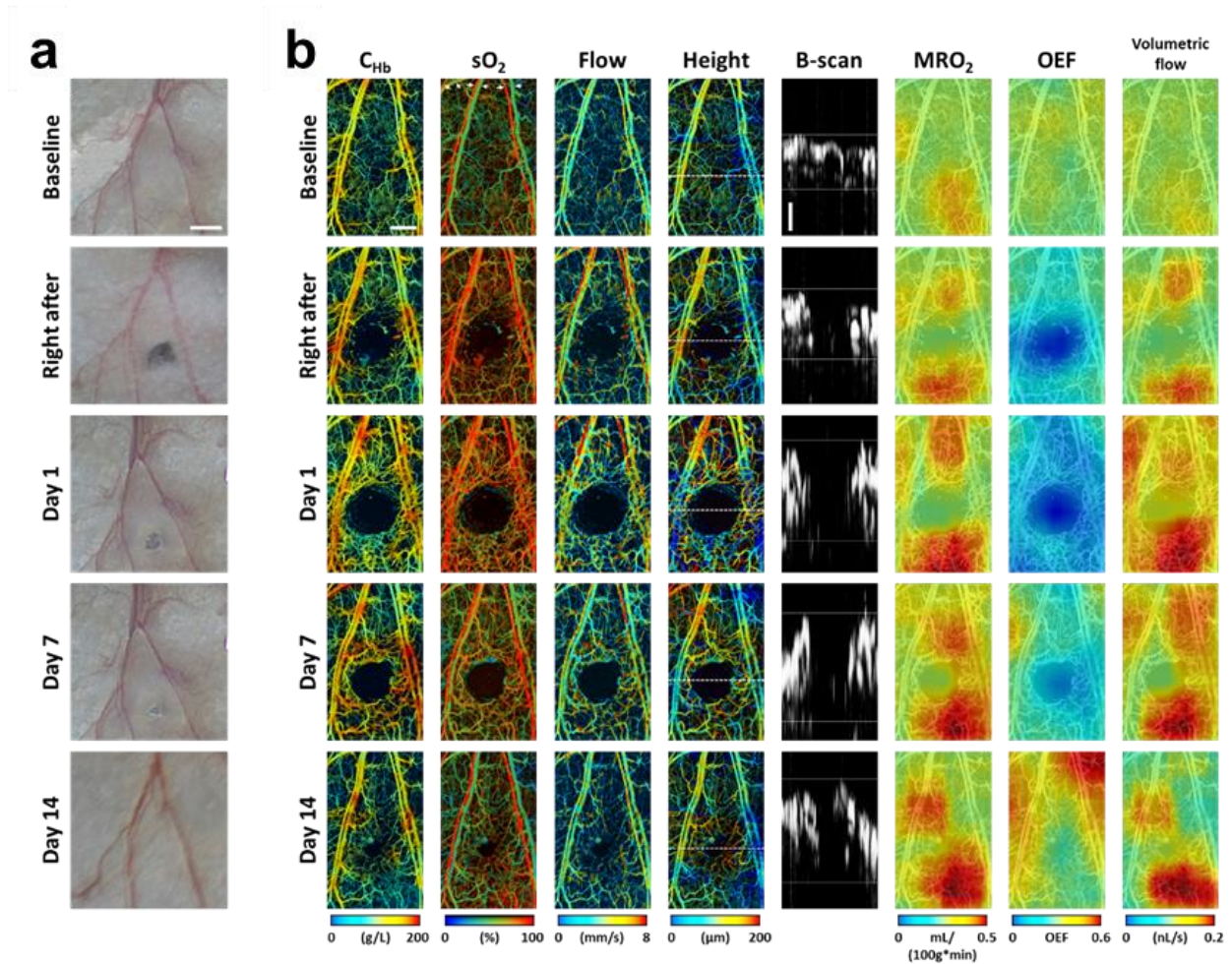
Fig. 8.1. (a) Pictures of wound healing process taken by microscopy; (b) Time-lapse PAM of the hemodynamic change during wound healing, For the height map, "0" is the position of the very bottom point for the ear microvasculature. The black-white images are the cross-section B-scans indicated in height images with the white dashed line, to show the thickness change in the wound area. Arrows on sO_2 map indicate the feeding arteries and draining veins analyzed in Fig. 8.2. Horizontal scale bar: 500 μm, vertical scale bar: 50 μm.

To better understand the hemodynamic redistribution, we repeated this experiment with three more mice and obtained the statistical result, as shown in Fig. 8.2.
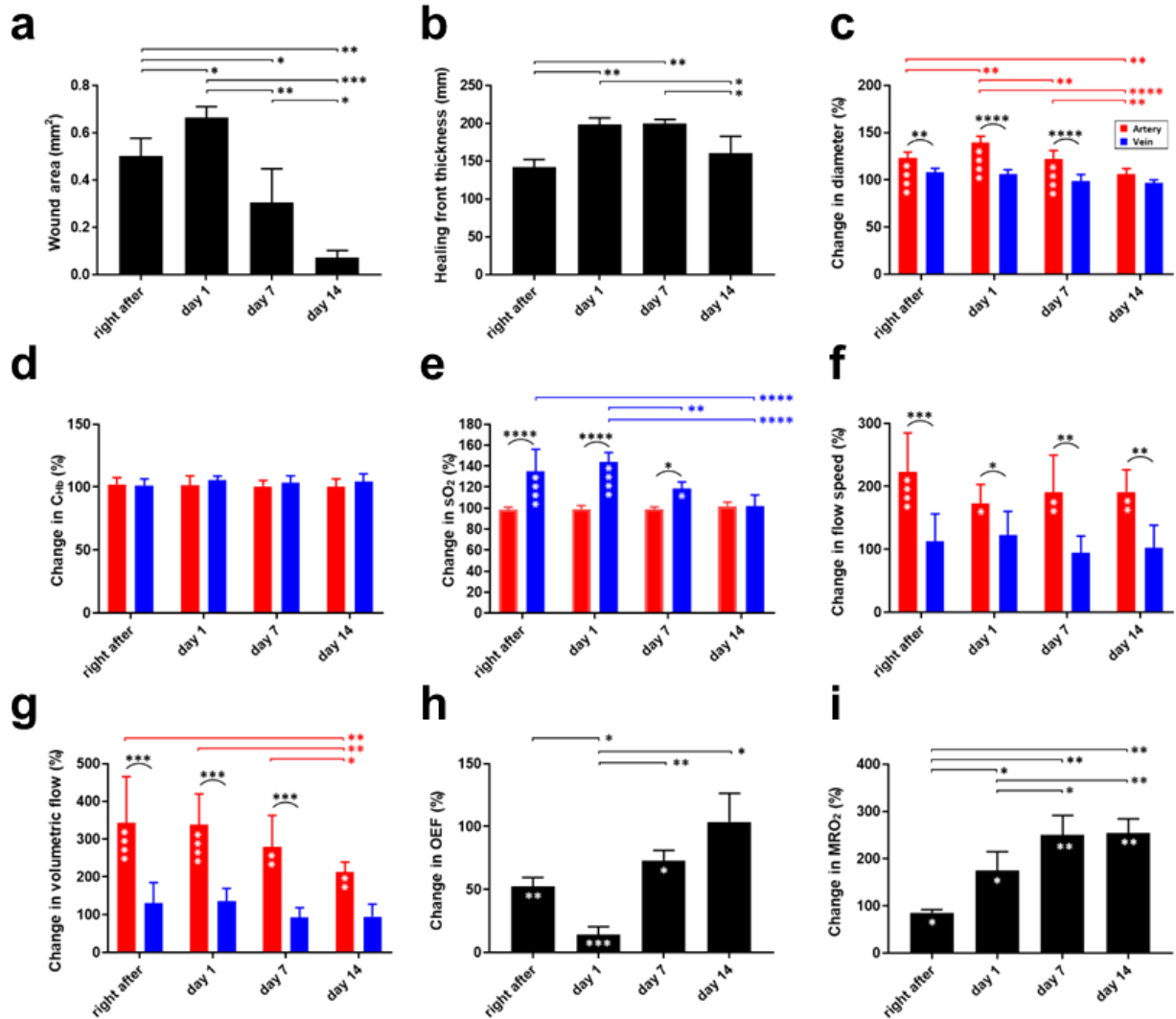
Fig. 8.2. Statistical comparison (N = 4) of (a-c) Structural change, (d-g) Hemodynamic change based on vessel segmentation, and (h-i) Hemodynamic change at the tissue level in the wound healing process. Healing front is defined as the surrounding of the wound with 10% area of the open wound area. White asterisks within the bars indicate the p value between the baseline (data not shown) and the certain timepoint. Paired t-test was used in (a), (b), (h) and (i), while two-way ANOVA tests were used in (c-g). *, **, ***, and **** respectively represent p<0.05, p<0.01, p<0.001, and p<0.0001. Data are presented as mean ± SD.

The results were consistent with what we observed in Fig. 8.1. However, to better reveal the mechanism behind the wound healing process, additional biochemical tests of the wound healing biomarker need to be performed, and a longer monitoring to the maturation phase is also essential.

8.2.2 Perfusion reserve across the different tissue/organ sites in response to the vasodilator

Involving the reduction of blood flow to the heart muscle due to build-up of plaque in the arteries of the heart[4], coronary artery disease (CAD) is the most common of the cardiovascular diseases[5]. Directly correlated to myocardial oxygen supply, the reduction of myocardial perfusion reserve (MPR)—the ratio of global myocardial blood flow at stress *vs* rest—is a sensitive indicator for evaluation of myocardial ischemia, thus has been widely investigated[6,7]. Enabling the noninvasive detection of MPR in myocardial ischemia, cardiovascular magnetic resonance has been widely used in clinical research to study CAD. However, the expensive cost of MRI system and the data acquisition is relative time consuming, which prevent the further application. Interestingly, our preliminary prefusion reserve value showed a correlation with the MRI results in healthy mice and obese mice. Thus, in this pilot experiment, we would like to explore the perfusion reserve across the different tissue/organ sites (i.e., the hindlimb, ear, and brain) of the same mouse in response to the vasodilator (i.e., Acetazolamide), to check the possibility of an alternative way to estimate MPR with superficial tissue/organs.

To achieve the awake imaging for all the tissue/organ sites, we updated our current multi-parametric PAM system with head frame restrained mouse ear plate and body container for awake mouse ear imaging and awake mouse hindlimb imaging, respectively. The PAM results are shown in Fig. 8.3, from which we could observe that the vasodilation was more severe in regular diet group than in high-fat diet

group across all the tissue/organ sites we imaged, which confirmed our hypothesis. However, to better understand the mechanism and explore the differences of perfusion reserve in different the tissue/organ sites, more effort should be made to mature this approach.
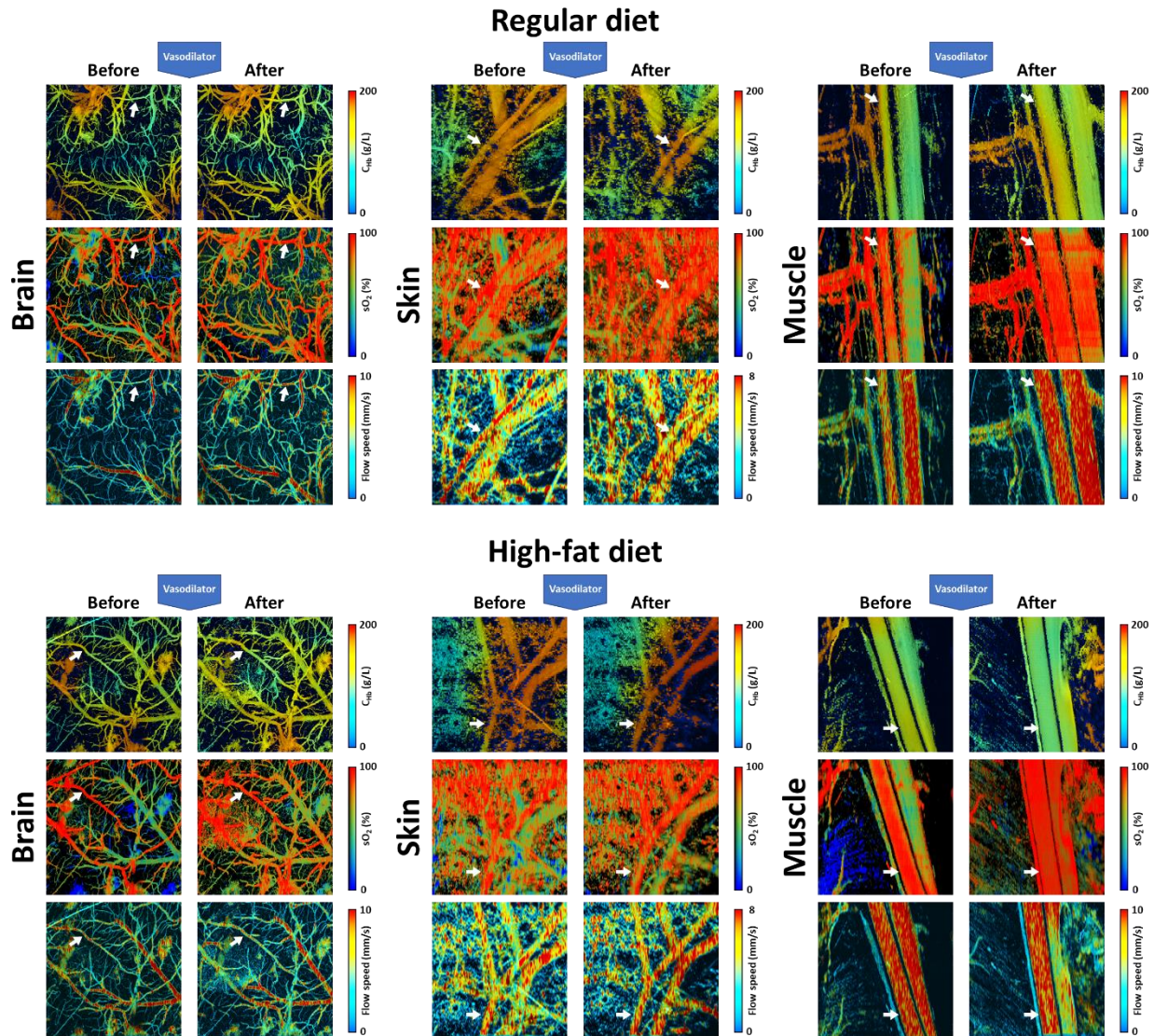
Fig. 8.3. Multi-parametric PAM images of mouse brain, skin (i.e., ear) and muscle (i.e., hindlimb) before and after the injection of vasodilator in regular diet mice and high-fat diet mice. Imaging size: 2 mm × 2mm

8.2.3 Tumor xenograft on the mouse ear

Cancer is a group of diseases that involve abnormal increases in the number of cells, with the potential to invade or spread to other parts of the body. With a numerous of types and possible causes, cancer has become one of the leading causes of death across the world[8]. Among all the approaches of studying cancer, the mouse tumor xenograft model plays an important role in the screening and evaluation on tumor growth, which always accompanies with abnormal vasculature and MRO_2. In this pilot experiment, female athymic nude mice (8-10 weeks, Envigo Co.) were used with intradermal injection on the dorsal side of mouse ear for two tumor cell lines: HEK-Ras12V (non-targeting control) and HEK-Ras12v+shDrp1 (Knockdown of Drp1). Besides the baseline imaging before the tumor cell injection, the tumor xenograft ear will be imaged up to 7 days post- tumor injection. Then the characterization of the tumor growth will be performed, to compare the two different tumor cell lines as shown in Fig. 8.4. From the results we could observe that, inhibition of mitochondrial fission-mediating GTPase Drp1 suppressed the tumor growth, angiogenesis, and blood flow, implying that knockdown of Drp1 inhibited mitochondrial fission, thereby impeding repair of damaged mitochondria and leading to reduced MRO_2 in comparison with the control. Spatiotemporally resolved metabolic reprogramming and metabolic response to Drp1 knockdown are observed in early-stage tumor xenografts in the mouse ear. These results demonstrate the feasibility of MRO_2 measurement by PAM at the tissue level in various mouse model. However, to better reveal the MRO_2-related tumor growth mechanism of the two tumor cell lines, additional tests of tumor growth biomarker, mitochondrial activity, and glucose metabolism need to be performed.
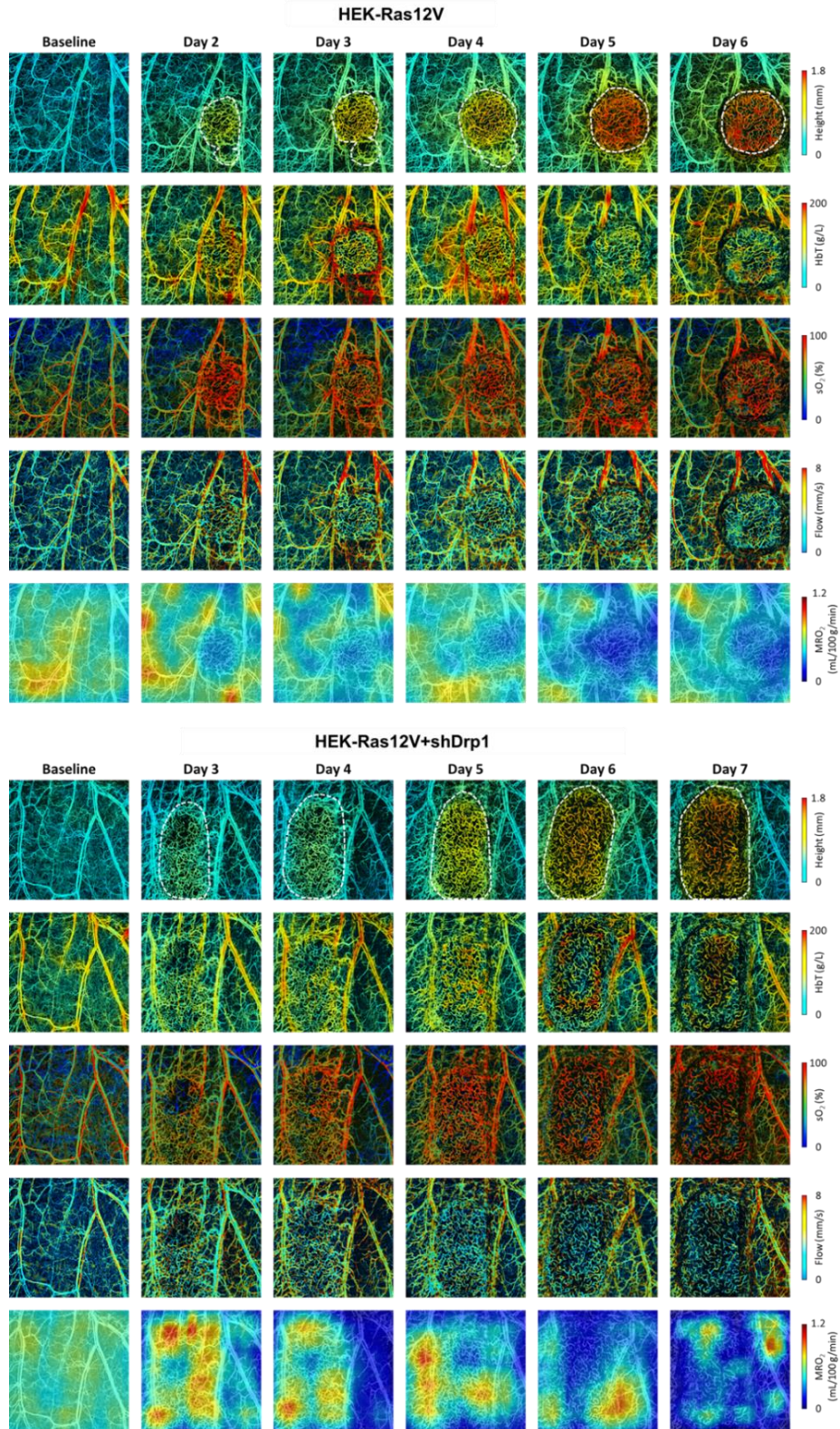
Fig. 8.4. Multi-parametric PAM of tumor xenograft on mouse ear of two cell lines: HEK-Ras12V (non-targeting control) and HEK-Ras12V+shDrp1 (Knockdown of Drp1). Imaging size: 6×6 mm^2.

Reference

[1]   Brigham, P. A. & McLoughlin, E. Burn incidence and medical care use in the United States: estimates, trends, and data sources. *The Journal of burn care & rehabilitation* **17**, 95-107 (1996).

[2]   Singer, A. J. & Clark, R. A. F. Cutaneous Wound Healing. *New England Journal of Medicine* **341**, 738-746 (1999).

[3]   Branski, L. K., Gauglitz, G. G., Herndon, D. N. & Jeschke, M. G. A review of gene and stem cell therapy in cutaneous wound healing. *Burns : journal of the International Society for Burn Injuries* **35**, 171-180 (2009).

[4]   Mendis, S. *et al. Global Atlas on Cardiovascular Disease Prevention and Control*. (World Health Organization in collaboration with the World Heart Federation and the World Stroke Organization, 2011).

[5]   Global, regional, and national age–sex specific all-cause and cause-specific mortality for 240 causes of death, 1990–2013: a systematic analysis for the Global Burden of Disease Study 2013. *The Lancet* **385**, 117-171 (2015).

[6]   Naresh, N. K. *et al.* Cardiovascular magnetic resonance detects the progression of impaired myocardial perfusion reserve and increased left-ventricular mass in mice fed a high-fat diet. *Journal of cardiovascular magnetic resonance : official journal of the Society for Cardiovascular Magnetic Resonance* **18**, 53 (2016).

[7]   Al-Saadi, N. *et al.* Noninvasive detection of myocardial ischemia from perfusion reserve based on cardiovascular magnetic resonance. *Circulation* **101**, 1379-1383 (2000).

[8]   Benjamin Emelia, J. *et al.* Heart Disease and Stroke Statistics—2019 Update: A Report From the American Heart Association. *Circulation* **139**, e56-e528 (2019).